



2

NRL/MR/6722--94-7460

Advanced Concepts Theory Annual Report 1993, Final Report

*Radiation Hydrodynamics Branch
Plasma Physics Division*

April 25, 1994

DTIC
ELECTE
MAY 16 1994
S B D

1098 94-14546

Approved for public release; distribution unlimited.

94 5 13 106

REPORT DOCUMENTATION PAGE			Form Approved OMB No. 0704-0188	
<small>Public reporting burden for this collection of information is estimated to average 1 hour per response, including the time for reviewing instructions, searching existing data sources, gathering and maintaining the data needed, and completing and reviewing the collection of information. Send comments regarding this burden estimate or any other aspect of the collection of information, including suggestions for reducing this burden, to Washington Headquarters Services, Directorate for Information Operations and Reports, 1215 Jefferson Davis Highway, Suite 1204, Arlington, VA 22202-4302, and to the Office of Management and Budget, Paperwork Reduction Project (0704-0188), Washington, DC 20503.</small>				
1. AGENCY USE ONLY (Leave Blank)		2. REPORT DATE April 25, 1994		3. REPORT TYPE AND DATES COVERED Final Report
4. TITLE AND SUBTITLE Advanced Concepts Theory Annual Report 1993, Final Report				5. FUNDING NUMBERS
6. AUTHOR(S) Radiation Hydrodynamics Branch				
7. PERFORMING ORGANIZATION NAME(S) AND ADDRESS(ES) Naval Research Laboratory Washington, DC 20375-5320				8. PERFORMING ORGANIZATION REPORT NUMBER NRL/MR/6722-94-7460
9. SPONSORING/MONITORING AGENCY NAME(S) AND ADDRESS(ES) Defense Nuclear Agency RAEV Alexandria, VA 22310				10. SPONSORING/MONITORING AGENCY REPORT NUMBER
11. SUPPLEMENTARY NOTES This research was sponsored by the Defense Nuclear Agency under Job Order Title, "Advanced Concept," MIPR No. 93,516.				
12a. DISTRIBUTION/AVAILABILITY STATEMENT Approved for public release; distribution unlimited.				12b. DISTRIBUTION CODE
13. ABSTRACT (Maximum 200 words) This report details the work of the Radiation Hydrodynamics Branch conducted in FY93 with respect to several critical problems concerning the design and analysis of DECADE z-pinch experiments. Separate sections describe progress in: (1) the evaluation of DECADE's predicted PRS performance, (2) the analysis and scaling of z-pinch experiments using phenomenological turbulence transport parameters in 1-D calculations, (3) the analysis of gas puff nozzle designs and large radius implosion stability, (4) the development of a DECADE transmission line model to study power flow, POS/PRS interactions, and energy coupling to PRS loads in DECADE, (5) the development of diagnostics with which to analyze experimental and theoretical PRS data, and (6) the development of L-shell atomic models.				
14. SUBJECT TERMS Z-pinch physics Plasma radiation sources Radiation MHD				15. NUMBER OF PAGES 110
				16. PRICE CODE
17. SECURITY CLASSIFICATION OF REPORT UNCLASSIFIED	18. SECURITY CLASSIFICATION OF THIS PAGE UNCLASSIFIED	19. SECURITY CLASSIFICATION OF ABSTRACT UNCLASSIFIED	20. LIMITATION OF ABSTRACT UL	

CONTENTS

EXECUTIVE PROGRAM SUMMARY	iv
A. PRS ON DECADE	1
B. ONE-DIMENSIONAL MODELING OF Z-PINCH IMPLOSIONS	25
C. PRS LOAD SIMULATIONS IN TWO-DIMENSIONS	41
D. DECADE POWER FLOW	49
E. ANALYSIS OF MHD DATA	76
F. L-SHELL MODEL DEVELOPMENT	92

Accession For	
NTIS GRA&I	<input checked="" type="checkbox"/>
DTIC TAB	<input type="checkbox"/>
Unannounced	<input type="checkbox"/>
Justification	
By	
Distribution/	
Availability Codes	
Dist	Avail and/or Special
A-1	

EXECUTIVE SUMMARY

This report describes theoretical work carried out in support of the Plasma Radiation Source (PRS) DECADE Program by Code 6720 in FY 1993. The six sections of the report discuss the following subjects:

- (1) In section I, DECADE's predicted PRS performance is discussed. During FY 93, a capability to evaluate the effect of different DECADE front-end designs on Marx-bank-energy-to-load-kinetic-energy conversion efficiency was developed, and a significant advancement was made in our ability to predict how load kinetic energy conversion to K-shell x rays scales with mass and implosion velocity. This advancement was made possible by a systematic comparison of theoretically predicted K-shell yields with measured yields in experiments on Double Eagle, Saturn, and Phoenix machines. The latter experiments were designed this year expressly for this task. There are two ways to approach the DECADE coupling and scaling problems. In one approach, emphasis is placed on the technical issues associated with power flow to the PRS load and on the design of multi-megajoule pulse-power generators for use as PRS x-ray simulators. In the other approach, emphasis is placed on the load-specific requirements for efficiently converting electrical energy into x rays (especially x rays that are tailored for use in NWET). The first approach to DECADE guides the design of DECADE's PRS front-end. In this case, it is assumed that if a pulse power machine can be built to meet the power flow and energy coupling PRS requirements, then x rays will be produced as predicted by the scaling laws. This assumption allows emphasis to be placed on machine design problems. In FY93, these scaling laws were put on a more solid foundation. The culmination of several recent years of experimental and theoretical efforts to improve the scaling laws is summarized in Section I. As a consequence, x-ray yield scaling in aluminum can now be predicted over three or more orders of magnitude, and machine requirements can be defined for achieving greater simulation fidelity. On scales of several orders of magnitude, a factor of two difference in yields can be ignored. However, when a DECADE- or Jupiter-class PRS machine is built, a factor of two difference in performance will be very significant in terms of dollars/photon. Thus, section I concludes with a discussion of some non-machine (load oriented) problems that were addressed as part of the FY93 technical risk reduction effort for DECADE. In both cost/photon and simulation fidelity areas, the load physics PRS issues become important.
- (2) The scaling relations being used to predict DECADE's PRS performance capabilities need theoretical and experimental validation for moderate atomic number loads, ($18 \leq Z \leq 29$). One way to validate theoretically is to carry out a set of calculations for titanium or copper that is similar to those that were done for aluminum. However, experimental implosions are much softer (i.e., much lower in density and much fatter in extent) than the aluminum implosions that were calculated in deriving the earliest version of the K-shell scaling laws. These calculations were carried out without the use of phenomenologically determined enhancements to classically calculated plasma viscosities, heat conductivities, and electrical resistivities. During FY93, a significant effort was completed to determine these enhancements from PI experimental data in order to obtain a more realistic scaling of K-shell yield with load mass and implosion velocity. In particular, the shift in breakpoint mass was determined from an analysis of argon and aluminum experimental data. This

work is discussed in Section II. Because soft implosion modeling generally produces better agreement between theory and experiment, it also creates new problems of discriminating between physical situations where conventional slug modeling and current-off procedures are valid and where they are not. These problems, which are the subject of current investigation, are also discussed in Section II. They are relevant to the problem, also under investigation, of increasing PRS emissions in the 10 to 20 keV region on DECADE or ACE IV.

- (3) Two problems arise as machine energy is scaled upwards. On the one hand, the PRS loads must be imploded from larger distances, leading to a possible degradation in implosion symmetry due to the onset of Rayleigh-Taylor instabilities. On the other hand, larger amounts of mass must be imploded, leading to questions of how nozzle designs should be scaled. The application of a 2-D MHD fluid code to address these problems is discussed in Section III. It is found, for example, that the growth of plasma instabilities can be mitigated by distributing a gas PRS load over a large volume and imploding it more as a snowplow than a plasma shell. However, this option leads to less kinetic energy generation than a shell implosion. The tradeoff between instability reduction and maximizing kinetic energy is an important 2-D issue under investigation. The 2-D code is also being used to investigate the influence of different gas puff nozzle designs on PRS performance. This gas puff work is being done in support of PI Double Eagle experiments, which provides a benchmark before they are applied to DECADE.
- (4) The POS is an important circuit element in DECADE when it is operated in bremsstrahlung mode. Its role in PRS mode is less certain. Over the last couple of years, an NRL transmission line model of an inductive energy store (IES) generator was constructed. Its POS model was benchmarked in FY92 to NRL Hawk POS data and applied in FY93 to the study of power flow in DECADE. In Section IV, the DECADE transmission line model is presented, and results of its benchmarking against PI's DECADE model are discussed. When coupled to a gas bag model PRS load, the NRL model supports the idea that the DECADE generator should be able to meet DECADE's radiation specs in PRS mode with or without a POS. With a POS, however, higher yields should be achievable with copper or krypton loads than without provided the POS operates at a sustainable high quality level. This prediction was tested theoretically, in part, by a sensitivity study of energy transfer to a PRS load to variations in the POS performance parameters.
- (5) Predictions of DECADE's performance and of load designs to improve its performance rely on the ability of theoretical models to accurately describe PRS load dynamics and on the ability of PRS experiments to meet performance objectives by design. To increase the reliability of theory and experiment, procedures to benchmark z-pinch calculations against experimental data must be developed. Some efforts in this direction are described in Section V. A set of experiments was recently carried out at the Weizmann Institute of Science in Israel in which an extensive set of measurements were made of the time-dependent radial velocity distributions of singly to five times ionized ions in an imploding plasma shell. It was speculated that an ionization wave propagating much faster than the local radial ion velocities was observed. In Section V, an analysis is described in which data similar to that observed in the Israeli experiments is obtained by post analyzing a 1-D MHD calculation.

The correspondence of this data to the Israeli data is discussed. The development of similar diagnostic procedures is planned for FY94 to be used in the analysis of the Saturn, PI, and Maxwell ACE IV data.

- (6) Finally, a small effort continued in FY93 to construct scalable L-shell models for use in developing diagnostics for PRS experiments on DECADE and ACE IV. This work is also relevant to problems such as L-shell burn-through. The model development, which is discussed in Section VI, is patterned after the successful use of hydrogen- to helium-like line ratios to derive information about the state of a plasma radiating in the K-shell. The generalization of these K-shell diagnostic procedures to the L-shell is accomplished by a substitution of the closed shell neon-like ionization stage for the closed shell helium-like stage and the fluorine-like for hydrogen-like stage. In the L-shell, the multiplet structure of the bound states complicates the problem of building reliable L-shell dynamical models; however, resources are available with which to address these problems. The fluorine-like model development described in Section VI makes use of atomic code capabilities that were developed at the Los Alamos National Laboratory.

I. PRS ON DECADE

A. DECADE ENERGY CONSIDERATIONS

Designing DECADE for use as a plasma radiation source (PRS) involves two problems: (1) the efficiency of coupling Marx bank energy to the PRS load must be realistically evaluated for different DECADE PRS front-end designs, and (2) the efficiency of converting coupled electrical energy into K- and L-shell kilovolt radiation must be realistically determined for a variety of load designs and for a selection of low, moderate, and high Z elements. During FY 93, a capability to evaluate the effect of different front-end designs on DECADE Marx bank/PRS coupling efficiency was developed, and a significant advancement was made in our understanding of the scaling of K-shell yields with mass and implosion velocity to DECADE. These developments will be described in this section. The latter advancement was made possible by a systematic comparison of theoretically predicted K-shell yields with measured yields on Double Eagle, Saturn, and Phoenix machines.

When emphasis is placed on technical issues associated with the design of multi-megajoule pulse-power generators, a machine approach to DECADE PRS performance is needed to guide the design of the DECADE generator's PRS front-end (with or without a POS). A PRS load can then be defined in simplest terms by the amount of mass, m , to be imploded and by the initial radius, r_i , from which it is imploded. Both of these quantities are assumed to be completely free variables. The most basic machine design problem concerns the determination of the amount of useful energy that the machine can deliver to the PRS load for conversion into x rays. The simplest way to address this problem is to use a (lumped) circuit model that describes a given DECADE machine to couple to the PRS load. A slug implosion model¹ of the load can then be used to calculate the kinetic energy imparted to the given load by the given machine. These calculations are stopped at a pre-determined radius (2 mm) and the final implosion velocity, v_{imp} , of the load is determined. The choice of 2 mm is governed by two factors: (1) the further in the slug implosion proceeds, the larger v_{imp} becomes and (2) the further out the implosion is stopped, the more likely it is that plasma back-pressure cannot halt the acceleration. Finally, the results of these calculations are displayed on an m - v_{imp} contour plot.

Fig. (1) shows such a plot. The darkened crescent region in Fig. (1) represents the span of implosion velocities that were calculated using the circuit model for DECADE that is shown in Fig. (2) for the range of radii and masses shown: $2 \text{ cm} \leq r_i \leq 3.5 \text{ cm}$ and $0.22 \text{ mg/cm} \leq m \leq 10.6 \text{ mg/cm}$. This darkened region overlaps with three regions that are labeled in Fig. (1) as regions of inefficient, efficient, and inefficient x-ray production respectively. The labeled regions in this figure are for titanium. Because the darkened crescent overlaps the efficient emission region, titanium loads should be able to efficiently convert implosion kinetic energy to K-shell x rays on DECADE, but only for a certain choice of radii and masses. More information about the origin of this figure will be published in an NRL memorandum report entitled "PRS Projections for DECADE".

The model in Fig. (2) contains the following basic elements of a DECADE circuit: the Marx generator, C_1 , the transfer capacitor, C_2 , the transfer switch, R_3 , the pulse forming line, L_3 , the plasma opening switch (PEOS), R_{peos} , the magnetically insulated transmission line (MITL) of the PRS diode, L_4 , and the PRS load, V_{load} . These elements were given the values shown in the figure.

From this lumped circuit of DECADE, one can compute the efficiency of converting the initially stored energy of the Marx bank, E_{Marx} , into PRS kinetic energy. For example, for the same range of masses and load radii that were used to obtain the span of implosion velocities shown in Fig. (1), one obtains the corresponding span of Marx-bank-to-load conversion efficiencies shown in Fig. (3) (for a 3 cm long array). For the Fig. (2) circuit, the largest mass loads, $m \sim 10$ mg/cm, are also the most efficient converters of Marx energy into load kinetic energy ($\sim 15\%$ - 17%). But, as Fig. (2) shows, this mass of titanium on DECADE is an inefficient K-shell radiator. Efficient emission is predicted to occur only for $0.6 \text{ mg/cm} \leq m \leq 1.8 \text{ mg/cm}$. For these masses, the conversion efficiency of Marx bank energy to kinetic energy is between 8% and 15%.

One can anticipate that, at the present time under optimum conditions, 30 to 50% of the kinetic energy generated during a PRS implosion can be converted into K-shell x rays in the efficient x-ray production region of $m - v_{imp}$ space. By multiplying together the above two conversion efficiencies, one concludes that 2.4 to 7.5% of the Marx bank energy can be converted to K-shell x rays by the Fig. (2) circuit model (8% to $15\% \times 30\%$ to 50%). Since $E_{Marx} = 8.5$ MJ, these considerations predict that the Fig. (2) DECADE machine should be able to generate between 200 to 640 kJ of titanium K-shell radiation. This factor of three in x-ray output could be extremely important to the simulator users community.

B. K-SHELL SCALING, THEORY VERSUS EXPERIMENT

Two implosion kinetic energies determine the radiation characteristics of PRS loads: (1) the kinetic energy per ion, $K_i \equiv (1/2)m_i v_{imp}^2$, and the kinetic energy per centimeter, $K_c \equiv (1/2)mv_{imp}^2$, where m_i is the mass of an ion. K_i determines the ability of the load to radiate from the K-shell. If L-shell radiation losses are ignored, then K_i must be larger than a predetermined minimum energy, E_{min} , which one can estimate by the formula, $E_{min} \cong 1.012Z^{3.662}$, where Z is the atomic number of the PRS load. Since K-shell radiation is also emitted per ion in units of E_{min} in the efficient emission region, it is convenient to define a dimensionless kinetic energy per ion, η , defined by $\eta \equiv K_i/E_{min}$. One can then work interchangeably in terms of the variables $\{m, v_{imp}\}$ or $\{m, \eta\}$.

Our present understanding of K-shell yield scaling evolved over a period of the last five years from a concerted theoretical and experimental effort between NRL and Physics International, Inc.. Roughly speaking, it involved the following four separate steps: (1) A simple slug model theory of K-shell yield scaling was developed. and used to plan a set of 1-D radiative hydrodynamics implosion calculations that systematically quantify the radiative capabilities of z-pinchs. In these calculations, m was held constant and η was varied or η was held constant and m was varied. (2) The results from these calculations, when plotted on a log-log graph, showed there were roughly two scaling regimes of K-shell yield with mass, which made sharp transitions into one another. The machine requirements for producing K-shell radiation from elements having atomic numbers higher than aluminum were then predicted. (3) Detailed comparisons were next made of the calculated z-pinch results with carefully analyzed experimental spectral data.² (4) The calculations were then systematically modified this year by enhancing the plasma viscosity, the heat conductivity, and the electrical resistivity through the use of multiplicative factors in order to improve their agreement with PI experiments. They had the effect of significantly modifying the scaling predictions.³ The newly modified scaling relation was used this year to analyze two sets of recently completed Saturn and Phoenix aluminum experiments. The Phoenix experiments were

designed and analyzed this year. Both the Saturn and Phoenix experiments were designed to probe K-shell emission through the predicted efficient emission region and to compare to the theory that was developed from the analysis of Double Eagle experiments. The analysis of these experiments led to the development of a new scaling relation with which to predict DECADE performance.

The experiments at Sandia National Laboratories and at NSWC on the Saturn and Phoenix machines respectively, make it possible to test the yield predictions over two different spans of m and v_{imp} in $m - v_{imp}$ space. The Saturn experiments were performed at the end of FY92. The highest yielding of the different mass load Saturn experiments are listed below in a table. Each array had a length of 2 cm:

SATURN PRS Experiments

Wire Diam (mil)	Wire Mass ($\mu\text{g/cm}$)	Array Diam (cm)	η	Wires #	K.E. kJ	Yield kJ	C.E. %
0.6	120	3.04	22	24	230	8.0	3.5
0.7	160	2.81	17	24	230	12.2	5.3
0.75	185	2.73	15	24	230	22.4	9.7
1.0	330	1.72	6.0	24	170	76.0	44.7
1.2	470	2.29	5.6	24	230	61.2	26.6
1.5	740	1.46	2.7	24	170	30.0	17.6
1.7	950	1.4	2.2	24	170	20.0	11.8
2.0	1310	1.34	1.6	24	170	14.2	8.4
2.5	2050	1.25	0.95	24	170	4.9	2.9

In each of these experiments, 24 two centimeter long wires of different, but standard, wire diameters were mounted at the different array diameters listed in the table. The total kinetic energies and the η values that are listed were computed from a slug model using the Saturn lumped circuit as its driver. The (K-shell) total yields were measured, and each percent conversion efficiency (C.E.) that is listed in the table is the ratio of measured yield to computed kinetic energy in each experiment. For the similar set of experiments carried out at Phoenix in FY93, again, only the highest yielding shots are listed.

The specific location in $m - v_{imp}$ space of these experiments is shown in Fig. (4) along with contours for predicted K-shell yields. The nine dots represent the nine 2 cm load Saturn experiments and the nine triangles, the nine 2 cm load Phoenix experiments. The K-shell yields that were measured in each of these experiments are plotted in Figs. (5) and (6) respectively. In both sets of experiments, the maximum yield was recorded in the experiment that lay within the efficient region but was closest to the $m = m_{BP}$ boundary curve. Moreover, as predicted, the yields fell as the experiments generated more implosion velocity, but moved further from the efficient region. Similarly, as the implosion velocity was decreased and the experiments moved in the direction of the $\eta = 1$ lower boundary line, the yields fell. The yield contours that are drawn in Fig. (4) were

Phoenix Aluminum Experiments

array length = 2 cm

Wire Diam (mil)	Wire Mass ($\mu\text{g/cm}$)	Array Diam (cm)	η	Wires #	K.E. kJ	Yield kJ	C.E. %
0.6	79	2.62	7.0	16	46	8.6	18.7
0.7	107	2.58	5.7	16	52	19.5	37.5
0.8	140	2.25	4.05	16	48.5	26	54
1.2	158	2.35	3.8	8	52	21.7	41.7
1.0	219	2.1	2.6	16	55	.9	33
1.5	246	1.9	2.2	8	46	22.9	49.8
1.6	280	2.0	2.0	8	49	21	43
1.2	315	2.26	2.2	16	60	14.7	24.5
1.6	560	1.15	0.6	16	31	6.5	21

derived from hard implosion calculations (corrected only for the mass breakpoint shift) and do not show the drop in yield with η that is seen in the data. However, soft implosion calculations do show this trend.

An important difference showed up between the Phoenix and the Saturn data. In all of the six Phoenix shots that lay within the efficient region, the percent conversion of kinetic energy into K-shell x rays was greater than the theoretically conservative value of 30%. For Saturn, however, only the maximum yielding of the five experiments within the efficient region exceeded 30%. However, in this one case, the Saturn conversion efficiency of 45% was close enough to the Phoenix maximum conversion efficiency of 54% to lie within the experimental variation of the two machines.

A tentative conclusion can be drawn from the location of the maximum yielding of the Saturn and Phoenix experiments. Since they both lie close to the curve, $y_K = y_{BP} \equiv y_K(m)|_{m=m_{BP}} \equiv y_{BP}(m_{BP})$, one can use this curve to predict an optimal aluminum performance for DECADE given by

$$y_{BP} = 0.0056m_{BP}^{1.514}, \quad (1)$$

when $f_K = 0.5$. This curve is drawn in Fig. (7), and the Phoenix and Saturn data points that represent the maximum yielding experiments are included on the figure. The DECADE and Jupiter points were placed on the curve by choosing the largest mass that can be accelerated to the breakpoint velocity by these machines. For DECADE, this mass was taken from Fig. (1).

C. ACE IV EXPERIMENTS

It is expected that ACE IV of Maxwell Laboratories will come on line within the coming year. This machine is a direct drive monolithic Inductive Energy Store (IES) generator. Since it is the first multi-megamp current IES driver, it is clearly useful to do PRS experiments on ACE IV in support of the DECADE PRS front-end design. In anticipation of such experiments, we

calculated the K-shell yields from argon puff gas loads on ACE IV over a range of initial radii and mass loadings using a transmission line model to describe the load/machine coupling. We found that for an appropriate mass loading and for a pinch length of 3 cm, the total argon K-shell yield should range from 40 kJ for a initial radius of 0.75 cm to 100 kJ at an initial radius of 6 cm. This significant improvement in yield as one moves out in initial radius could be used as a test of large radii implosions to determine if any degradation occurs due to Rayleigh-Taylor type instabilities during the run in.

The calculation of the K-shell radiation yield is adopted from Whitney, et al. scaling (J. Appl. Phys., 67, p.1725, 1990). Recently, this theory has been reworked so that the yield Y_K can be treated as a function only of the final implosion velocity v_f , the mass loading per unit length M/ℓ , and the atomic number Z_{nuc} . Contours of constant yield over the $v_f - M/\ell$ plane are presented for argon in Fig. (8). For purposes of evaluating the predictive capability of such a graph, the measured peak argon K-shell yields (per cm) on DOUBLE EAGLE and SATURN are noted as circles. In the inefficient regime, the yield scales as $(M/\ell)^2$, while in the efficient regime it scales as (M/ℓ) . The K-shell scaling theory becomes invalid when the kinetic energy per particle divided by the energy needed to attain K-shell ionization conditions is less than or close to unity. This ratio is termed η in the reference above, and two values are contained in the plot.

As presented, the K-shell yield scaling is independent of the driver, demanding only a knowledge of the final velocity and mass loading. In order to predict yields for ACE IV, we used the transmission line circuit model for ACE IV pictured in Fig. (9). It has been compiled from information forwarded to Code 6720 by E. Waisman and R. Ingermanson of Maxwell laboratories. For the plasma opening switch (POS) we used their results, which show a quadratic rise in POS impedance to 1.3 ohms in 80 nsec. If we assume that the argon gas puff is initially a thin shell, one can drive a slug model implosion with this circuit and stop the implosion once the radius of the slug reaches 1/10 of its initial radius. The slug velocity at this point is equated with the final velocity v_f . For ACE IV we took the pinch length as 3 cm. The current profiles for various values of mass loading times the square of the initial radius, MR_o^2 , are contained in Fig. (10). For a slug model, the current and implosion time are only dependent upon this product. Note that for $MR_o^2 > 100 \text{ mg cm}^2$, the peak current into the load is 8 MA, and that the inductive notch decreases slightly for longer implosion times.

With the calculated final velocity and the mass loading, which is input at the beginning of the calculation, one can employ Fig. (8) to determine the radiation yields for argon. Contours of constant K-shell yield (not yield per cm) are presented in Fig. (11) as dotted lines. This is the plane of initial radius R_o versus mass loading M , and represents the plane of initial conditions assuming a slug implosion model is an adequate description. Lines of fixed η values are shown as solid. The constant slope lines are labeled with their corresponding value of MR_o^2 in mg cm^2 , and can be used in conjunction with Fig. (10) to estimate implosion times. It is imperative to state that the shape of the curves in this figure are very dependent upon the machine driving the implosion. No general conclusions can be made regarding other generators.

To summarize this analysis, the peak yields for argon on ACE IV as configured in Fig. (9) appear to arise for η between 2 and 3. Consider a total mass loading of 1.5 mgm. If the initial radius is 0.75 cm, one can expect ~ 40 kJ of K-shell radiation Y_K . On the other hand, moving out to 6 cm initial radius more than doubles the Y_K and increases the implosion time from ~ 80 to ~ 340 nsec. It would be useful to run a series of experiments of ACE IV where the mass in the argon gas puff is constant while the outer radius is substantially increased. Information on

the stability of large radius, long time implosions would have direct implications for the design conditions and yield expectations of the next generation of PRS drivers.

D. PRS ISSUES

Load oriented issues must also be addressed in order to optimize DECADE's performance as an NWE simulator. We will briefly discuss some of these issues, and mention some of the work that was done this year in addressing them. They are subsumed under the following four topics:

- PRS Initial Conditions
- PRS On-axis Symmetry and Implosion Stability
- 20 to 30 KeV Photons
- Radiative Collapse

Each of these topics is discussed briefly in turn.

PRS Initial Conditions

Two basic assumptions underlie the scaling calculations described above. All of the hydrodynamics calculations begin with a given mass of pre-ionized cylindrically symmetric plasma tightly located, on average, at the initial position of a wire array. They assume (1) that the power flow from the pulsed power machine can be coupled to the wire load to uniformly ionize it quickly and (2) that the implosion then takes place with all of the wire mass imploding inwards as described by a slug model driven by the $\mathbf{j} \times \mathbf{B}$ forces of the current discharge. These assumptions are not always justified. Large diameter wires do not necessarily ionize uniformly, some of the wire mass may be left behind in the implosion, and mass can be driven in under a combination of slug and snowplow dynamics. The first two of these wire phenomena are suggested by experiments, and the third, by the analysis of PI data that was carried out this year.³ One conclusion that can be drawn from these considerations is that, as machine power is increased, the problem of evaluating the initial response of a wire load to the current pulse could be the most significant part of the power flow problem.

Other evidence, shown in Figs. (12) and (13), was found this year to suggest the importance of the initial breakdown response of a PRS load to the overall performance of an x-ray simulator. In Fig. (12), the Saturn yield data, discussed above, is plotted as a function of array diameter. This figure also includes Double Eagle data. The dip in the Saturn yield at an array diameter of 2.2 cm is correlated to the rise in the wire ion density generated by the wire explosion halfway into the current rise (Fig. (13)). A self-similar hydrodynamics model was used to calculate the explosion dynamics. It assumed that the wire expansion was uniform and that this expansion was driven by a time evolving isothermal plasma. This work is described in greater detail in Ref. (4).

PRS On-axis Symmetry and Implosion Stability

As machine power is increased, the initial array diameter of a PRS load will also need to be increased for several reasons. Large radii implosions will reduce some of the difficulties in getting power to flow initially into the diode and to couple effectively to the PRS. They will also reduce the requirement for a fast rising current pulse. Finally, they should allow higher aspect ratio (i.e. larger ratios of initial to final array diameter) implosions to be achieved. Increases in this ratio will translate into increases in v_{imp} and to a greater likelihood that the K-shell of high Z elements can be ignited by these implosions.

As array diameters are increased, it could become increasingly difficult to maintain the symmetry of the implosion, which is critical for achieving tight, high density implosions on axis. High density is important if efficient x-ray production is to be achieved. One of the impediments to driving symmetrical implosions is the finite number of return current posts that have been used to date.⁵ They automatically destroy cylindrical symmetry and may support the generation of plasma turbulence, which, in turn, softens the pinch and makes x-ray production more difficult. Current and load asymmetries will also lead to 2-D plasma flow effects and to Rayleigh-Taylor instabilities.

Whether or not and by how much load instabilities and asymmetries degrade radiation yield is an open question. 2-D fluid calculations are useful for studying 2-D flow effects in large aspect ratio implosions and for determining conditions for increasing implosion stability and on-axis symmetry with structured large diameter loads. 2-D fluid calculations might also be of use in initiating investigations of plasma turbulence, a process not present in 1-D fluid calculations. However, 3-D calculations are needed if one is to accurately track the late time evolution of turbulence. They are also needed to accurately investigate the nonlinear evolution of Rayleigh-Taylor instabilities and their transition to turbulent flow. If large radius implosions are turbulent (from finite numbers of return current paths, current driven vorticity generation, or Rayleigh-Taylor instabilities), then this turbulence's main effects are already being modeled in our 1-D calculations through the use of multipliers for viscosity, heat conductivity, and electrical resistivity. An important question for large radius implosions, therefore, is: will Rayleigh-Taylor cause 2-D average flow defects to form and how deleterious will they be to x-ray production? However, if these effects can be studied and understood, then they can be mitigated.

20 to 30 KeV Photons

There are three basic processes by which plasmas radiate: bound-bound, free-bound, and free-free. The latter is also known as bremsstrahlung emission. Bound-bound emission comes in two forms: line emission from valence electrons or line emission from inner-shell transitions. The relative strength of these processes in a PRS plasma is valence bound-bound \gg free-bound \gg free-free \sim inner-shell line. One example of free-bound emission is shown in Fig. (14), which contains a power spectrum for argon that was obtained during the course of a 1-D MHD implosion calculation. Notice that the K-shell lines, located at 3 to 4.5 keV for argon, sit on top of two free-bound continua. Also notice that the continuum formed by the recombination of a totally ionized argon ion to the hydrogen-like ground state extends to 10 keV in Fig. (14). A dashed line is drawn in this figure to indicate that if the argon plasma had been hotter (and confined), this free-bound continuum would extend to 20 and 30 keV and beyond. Thus, a hot, dense, confined argon plasma would be an ideal source for 20 to 30 keV photons for NWET (on DECADE?).

Radiative Collapse

The K-shell scaling laws, developed to date, make use of 1-D hydrodynamics calculations in which the current is terminated where early slug model calculations were terminated. These current-off calculations have the utility of making kinetic energy the principle energy input to the plasma so that the calculated x-ray conversion efficiencies pertain only to kinetic energy conversion. In experiments, however, the current does not turn off, and the present scaling laws may be too conservative. Maintaining the current on increases the confinement of the pinch, and

it can also lead to its radiative collapse. Both of these phenomena could enhance the radiative output. They may also enhance production of x rays in the 20 to 30 keV energy range.

Figs. (15) and (16) show the relevance of current-on calculations to DECADE. Because of its large current, DECADE will have the capability of accelerating a wider range of aluminum masses into the efficient scaling regime, depending on the initial radius, r_i , of the aluminum array, than existing simulators have. This point is illustrated by the shaded region drawn in Fig. (15). The vertical line, drawn at 0.8 mg/cm as an example, shows how DECADE will provide a capability to map out the dependence of K-shell yield scaling on η for fixed m . This capability is not available on currently operational PRS simulators. Fig. (15) also suggests that DECADE should provide a capability of exploring radiative collapse behavior over a range of masses from 0.4 to 8 mg/cm.

The role of kinetic energy in the implosion dynamics will also be much more varied in DECADE than for existing PRS simulators. Fig. (16) illustrates this point. This figure is to Fig. (15) as Fig. (3) is to Fig. (1). The numbers that label the boundaries in Figs. (15) and (16) are in one-to-one correspondence. Thus, the implosions between 0.2 and 0.6 mg/cm that lie along boundary 1 in Fig. (15) convert only a small fraction (~ 2 to 4%) of the Marx bank energy into kinetic energy. A substantial portion of the Marx energy may be available, therefore, to drive implosions that radiatively collapse on axis. *DECADE's PRS capability will be essential for carrying out these experiments. They could enhance simulation fidelity capability.*

REFERENCES

1. J. Katzenstein, J. Appl. Phys. **52**, 676 (1981).
2. C. Deeney, T. Nash, R. R. Prasad, L. Warren, K. G. Whitney, J. W. Thornhill, and M. C. Coulter, Phys. Rev. A **44**, 6762 (1991).
3. J. W. Thornhill, K. G. Whitney, C. Deeney, and P. D. LePell, Phys. Plasmas **1**, February, (1994), to be published.
4. K. G. Whitney, J. W. Thornhill, R. B. Spielman, T. J. Nash, J. S. McGurn, and L. E. Ruggles, "Analysis of Recent Saturn Aluminum PRS Experiments", Proceedings of the 3-rd International Conference on Dense Z-pinchs, London, England (1993), to be published.
5. "Advanced Concepts Theory Annual Report 1992, Final Report", NRL Memorandum Report 6722-93-7301 (1993).

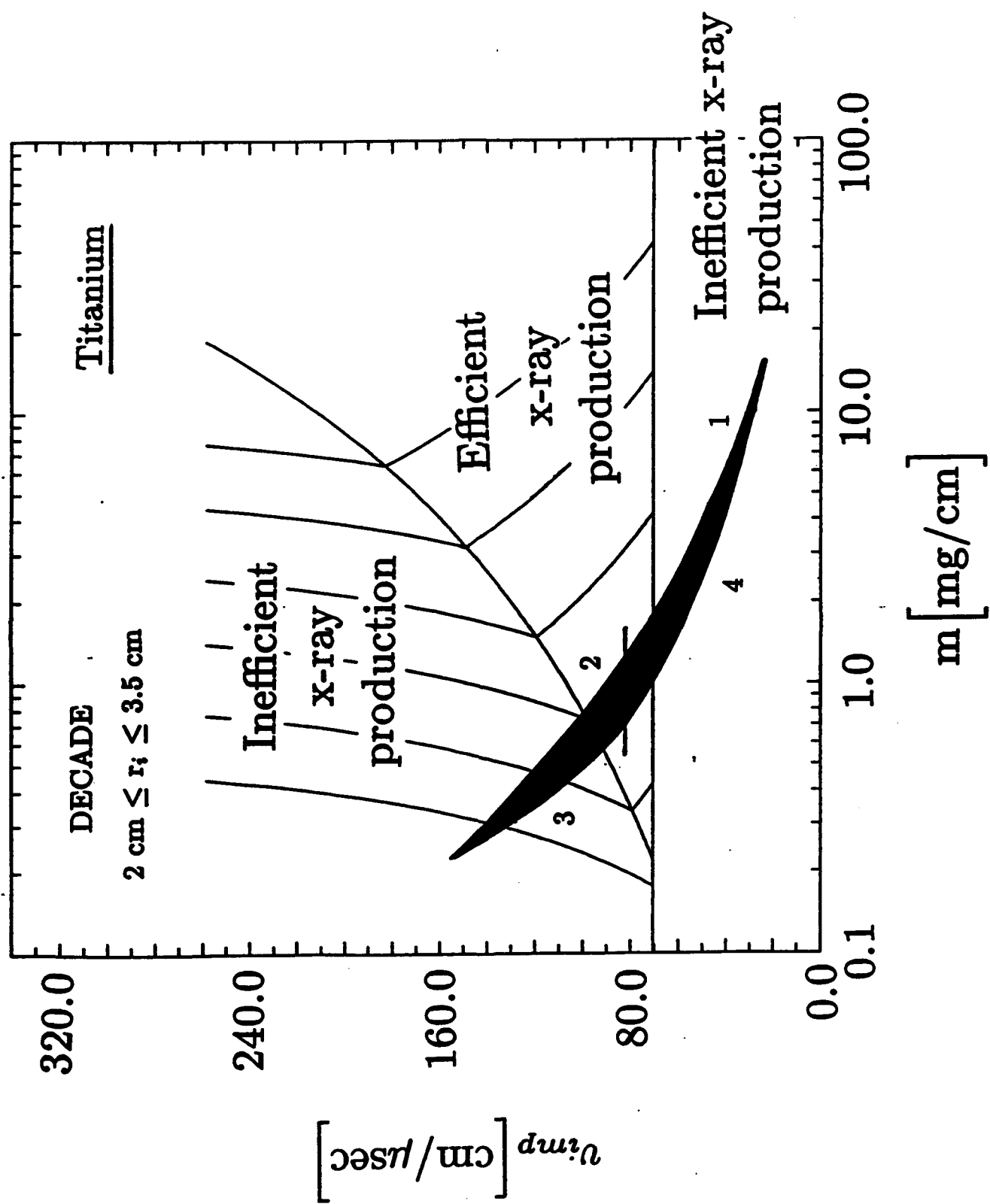
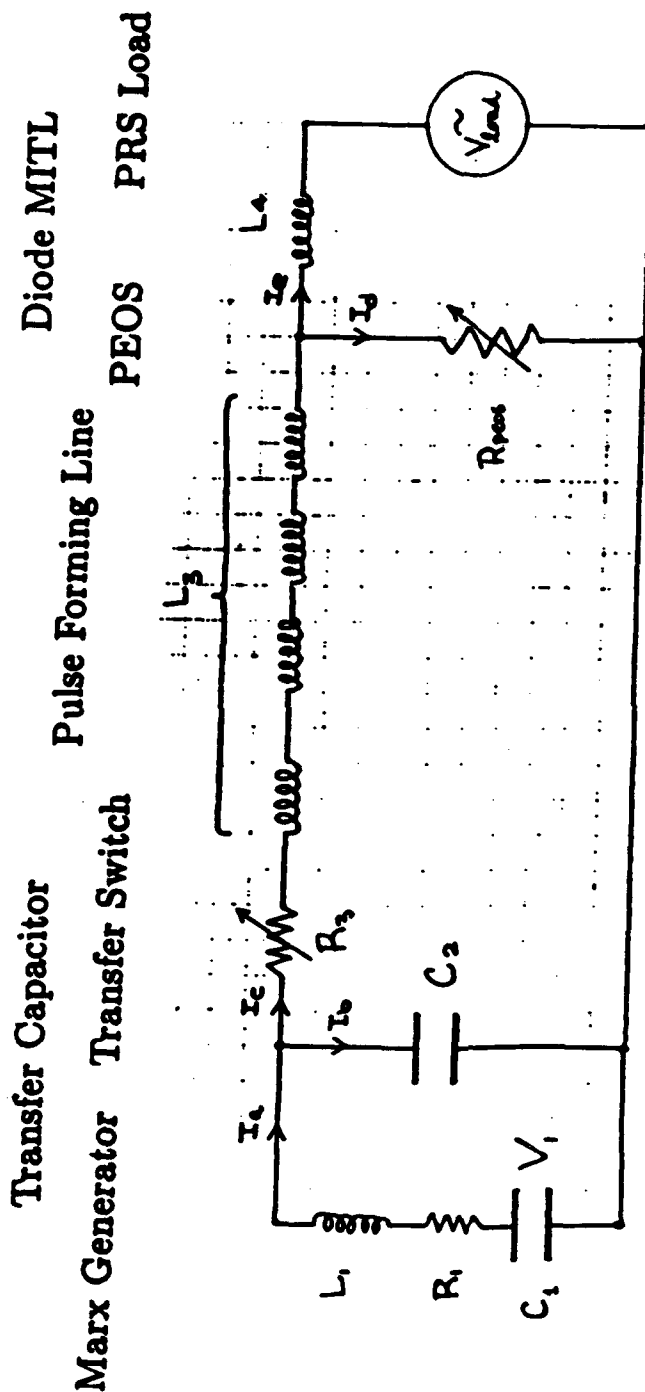


Fig. 1

DECADE CIRCUIT MODEL



Equivalent Lumped Circuit

$C_1 = 21.12\mu F$	$L_1 = 17.7nH$	$L_3 = 9.92nH$
$V_1 = 0.87MV$	$C_2 = 23.6\mu F$	$L_4 = 4.0nH$
$R_1 = 2.56m\Omega$	$R_3 = 100\Omega \rightarrow 0.125m\Omega$	$R_{PEOS} = 0.1m\Omega \rightarrow 0.17\Omega$

Fig. 2

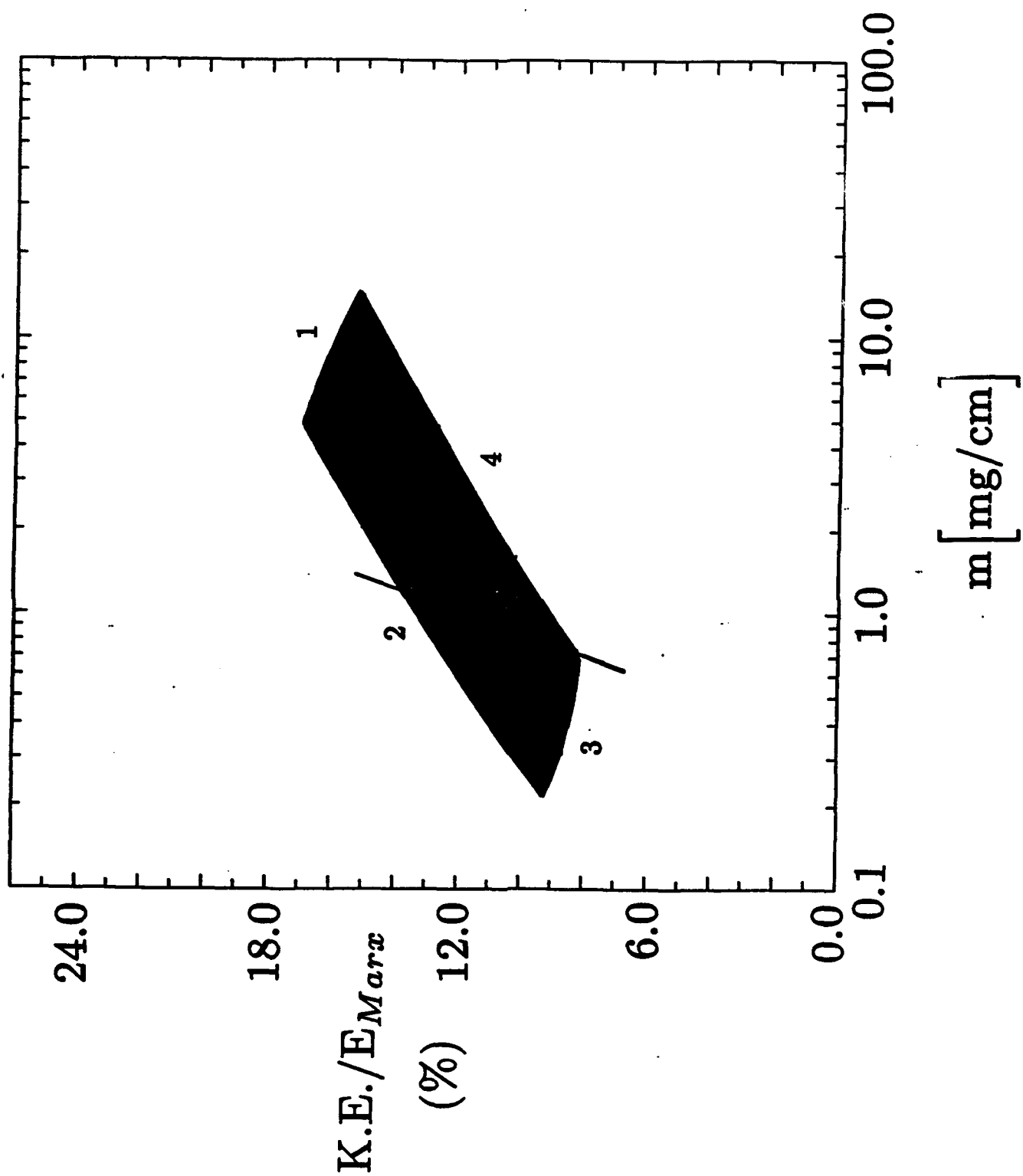


Fig. 3

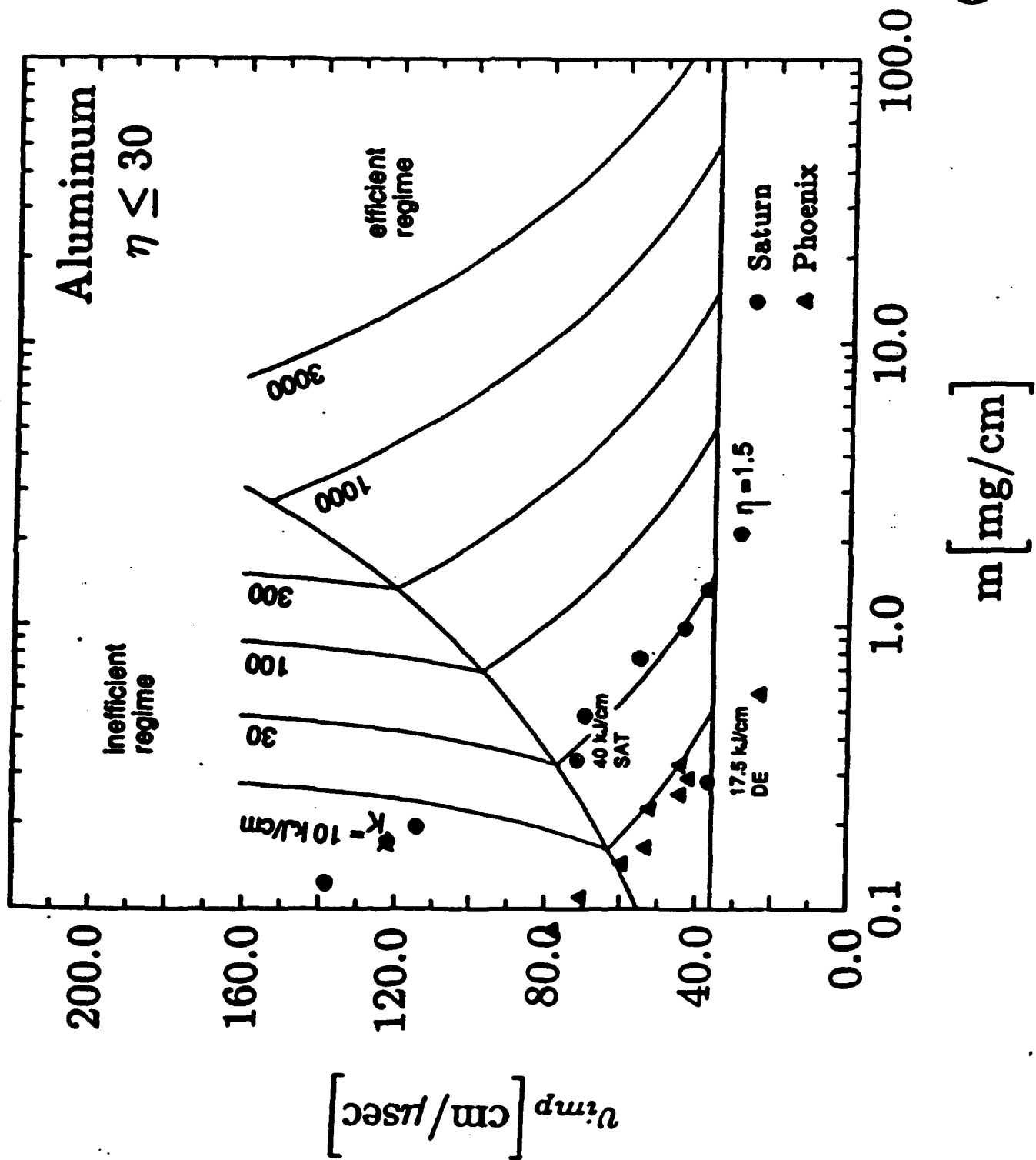


Fig. 4

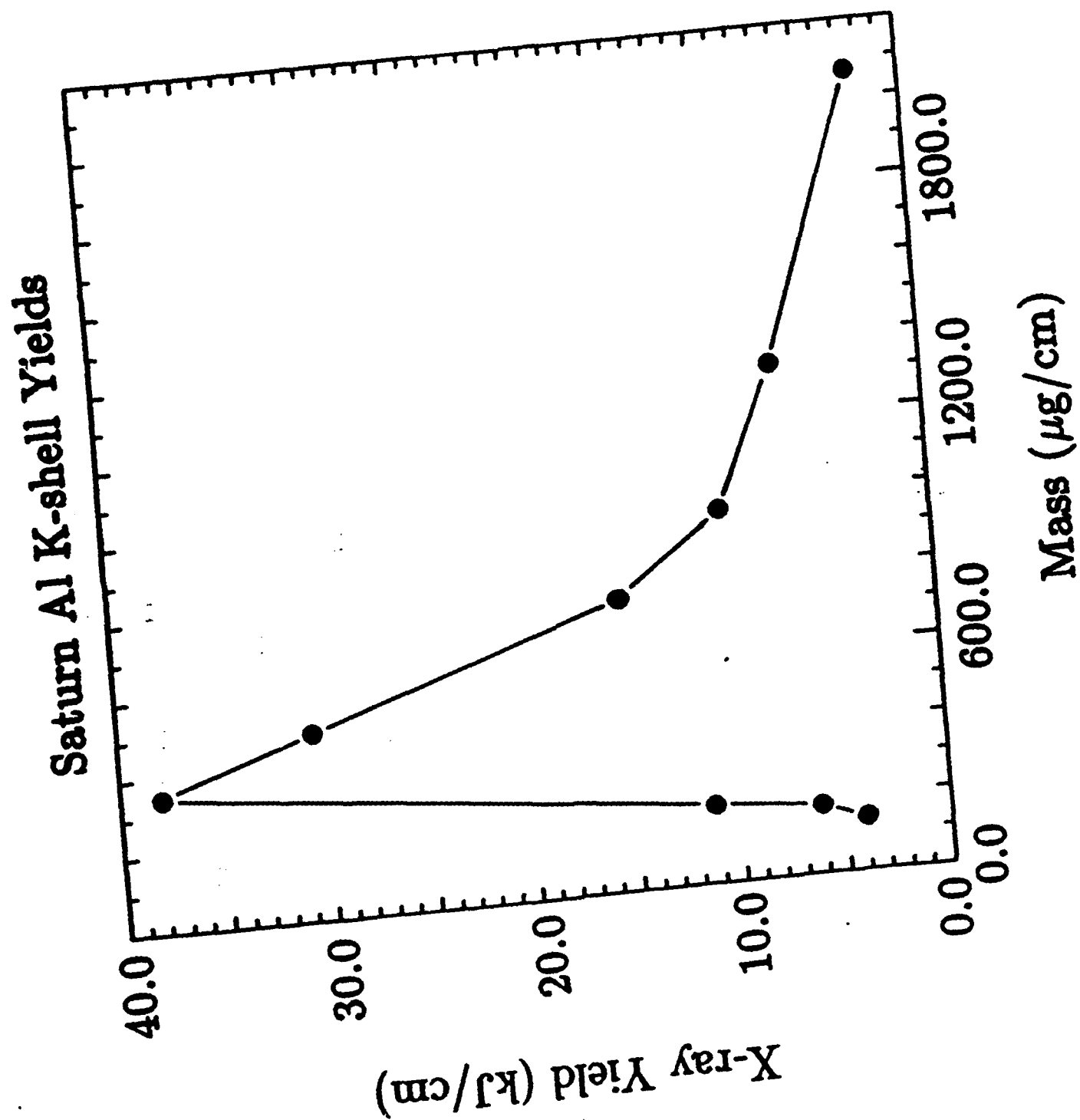


Fig. 5

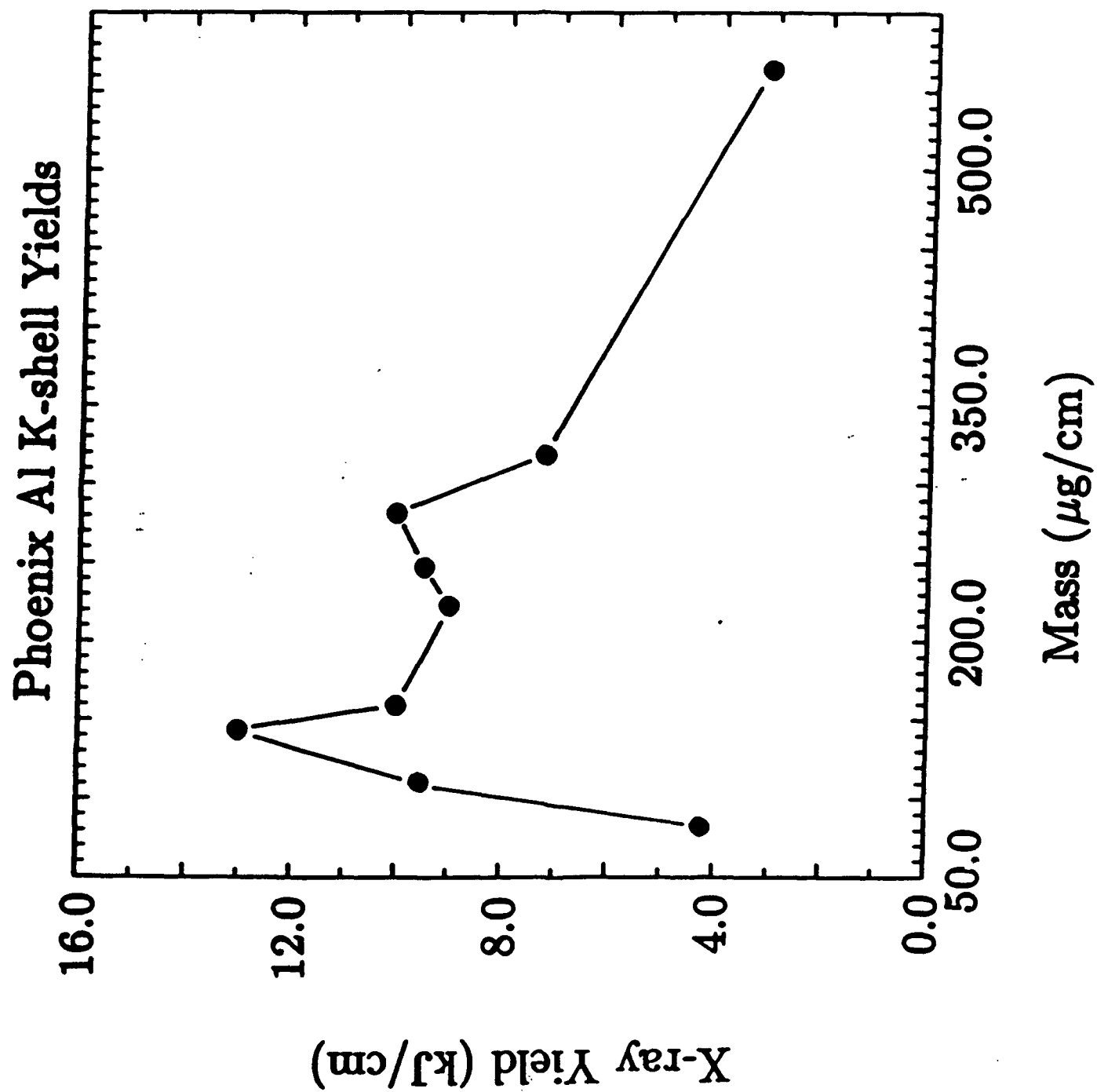


Fig. 6

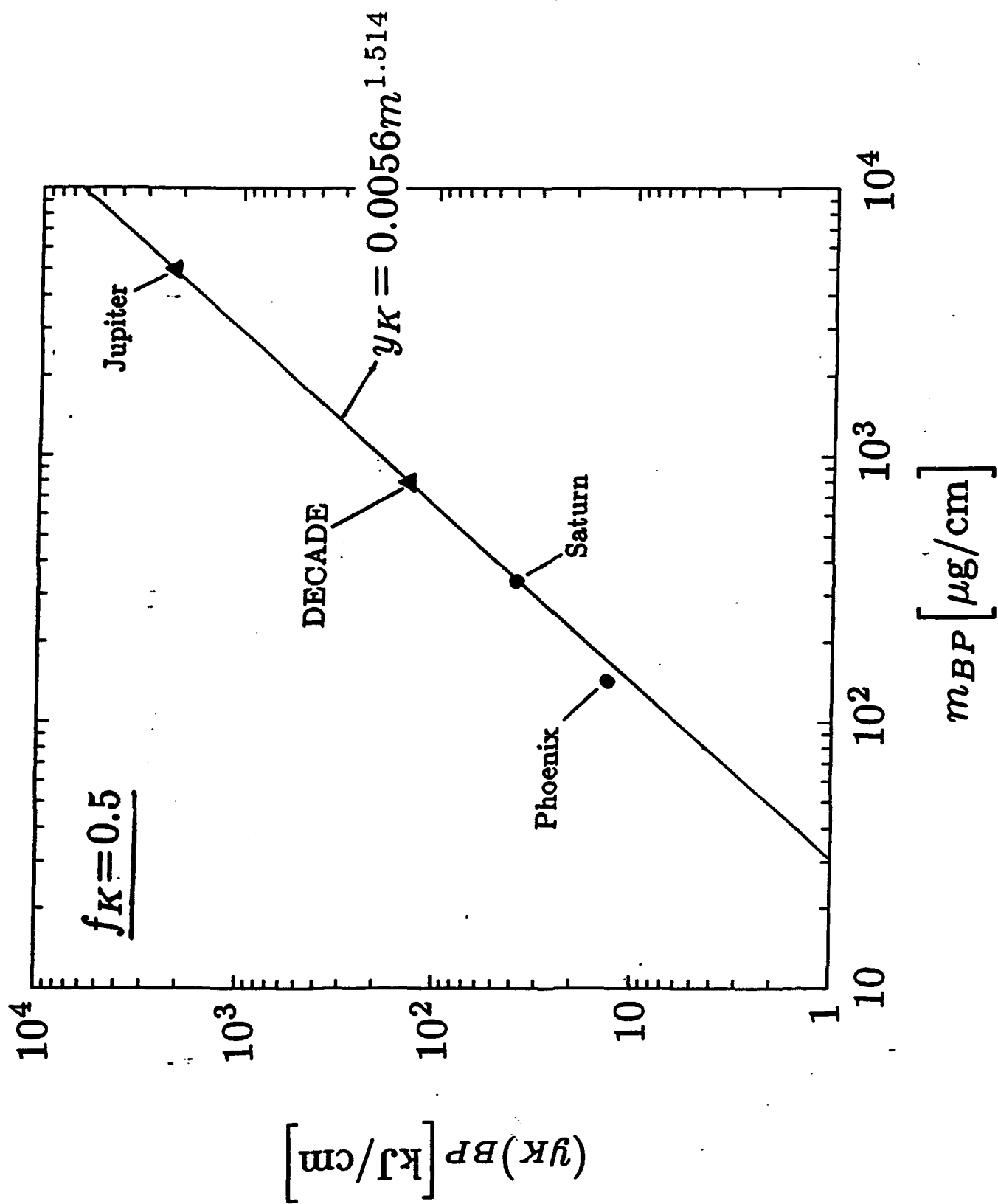


Fig. 7

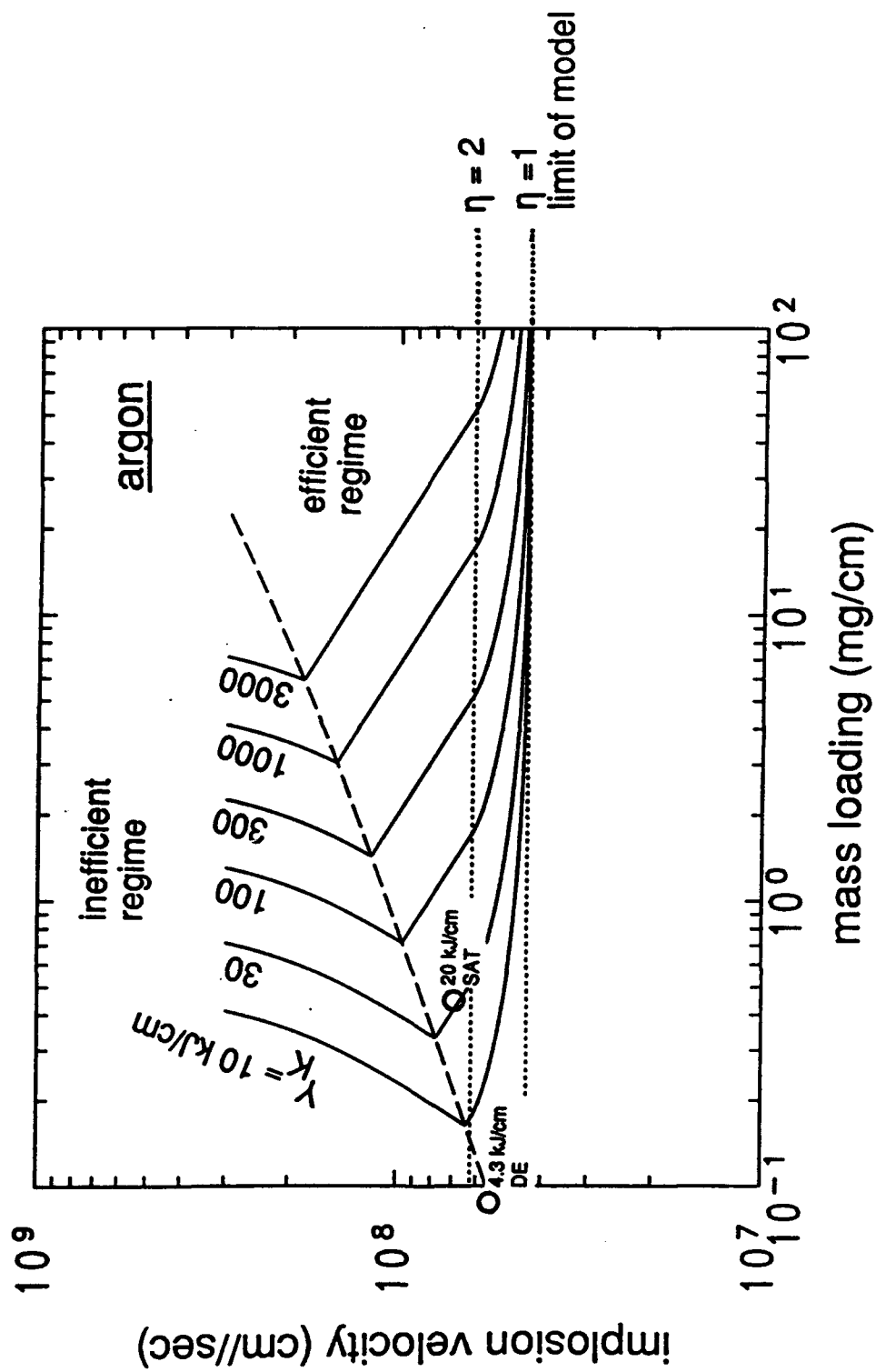


Fig. 8 Contours of constant argon K-shell yield as a function of the implosion velocity and mass loading per unit length. Optimal experimental results for DOUBLE EAGLE and SATURN are plotted.

ACE IV Circuit Model

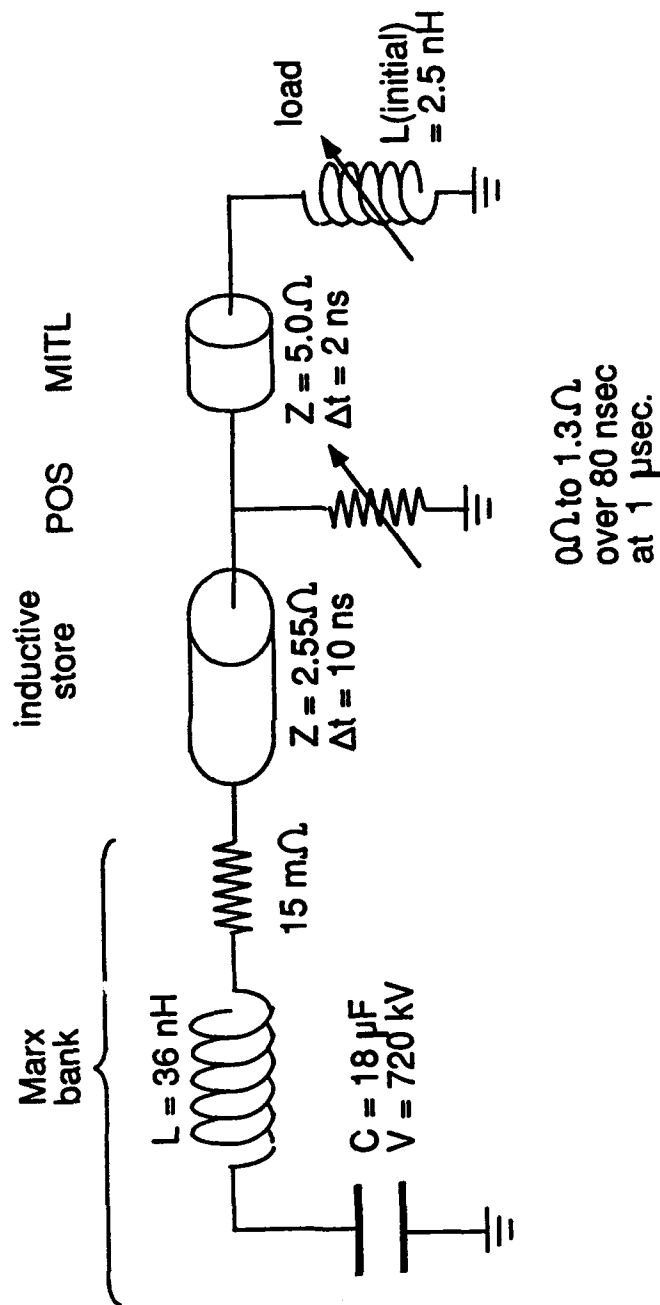


Fig 9 Transmission line model used for ACE IV. The pinch length is taken as 3 cm.

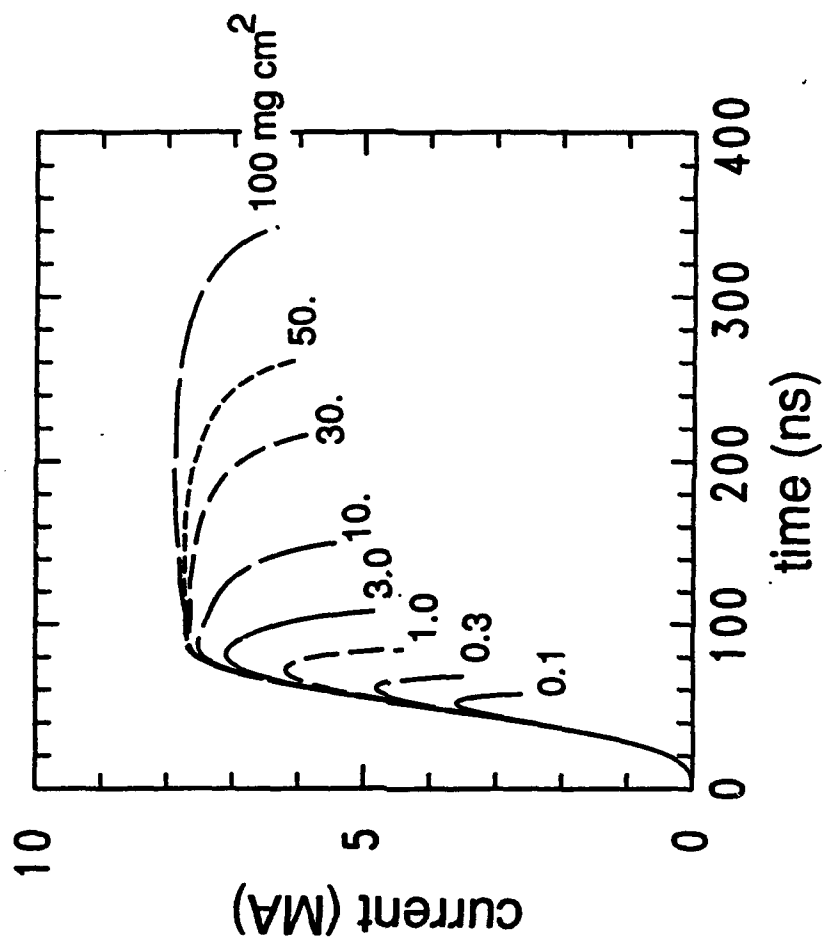


Fig.10 Current profiles for various values of MR_0^2 in units of mg cm^2 . $t = 0$ corresponds to the opening of the plasma opening switch.

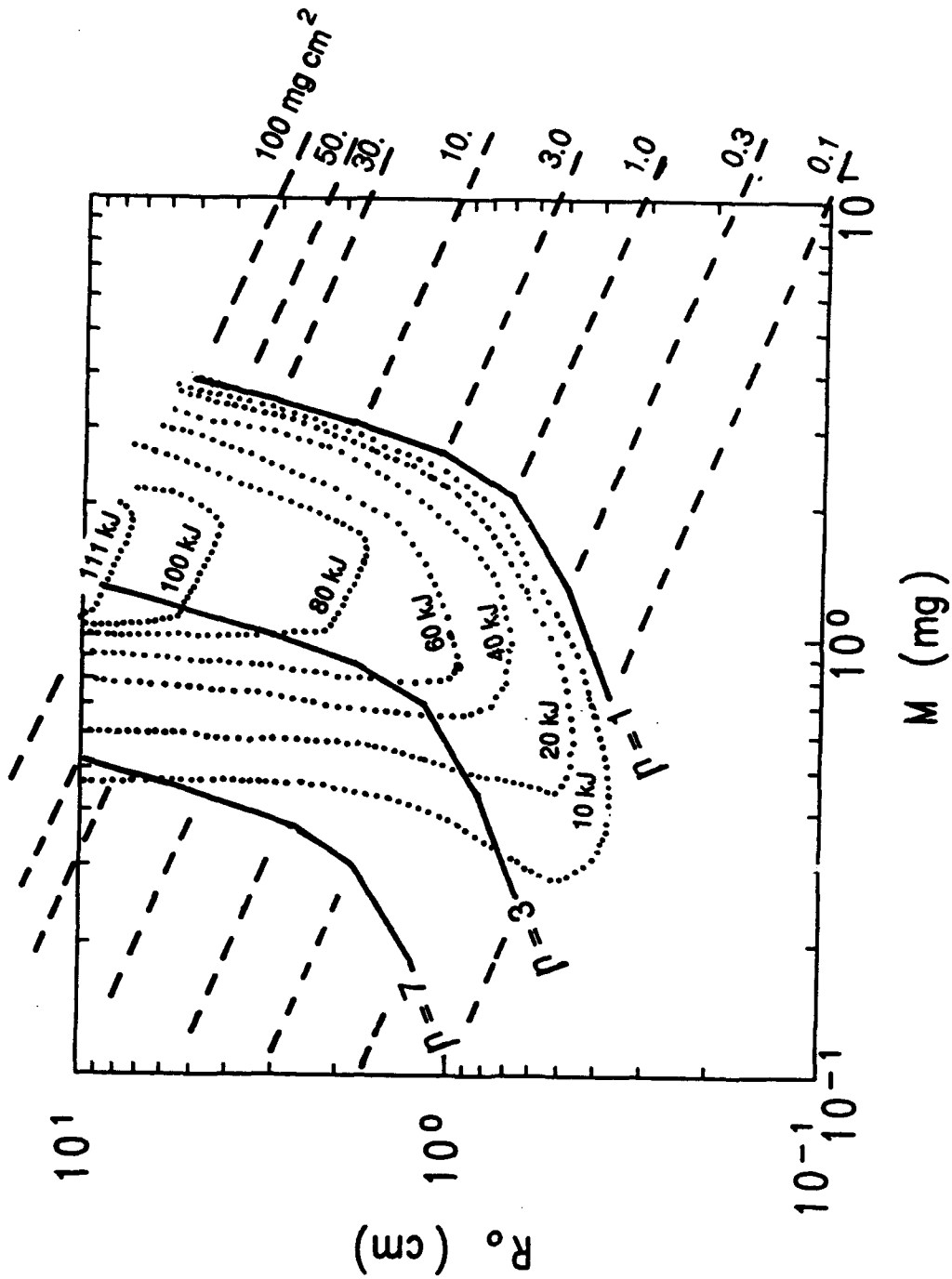


Fig.1.1 Contours of constant argon K-shell yield (dotted) as a function of the initial puff radius and mass loading. Contours of constant n are shown as solid, and constant $M R_o^2$ in units of mg cm^2 as dashed.

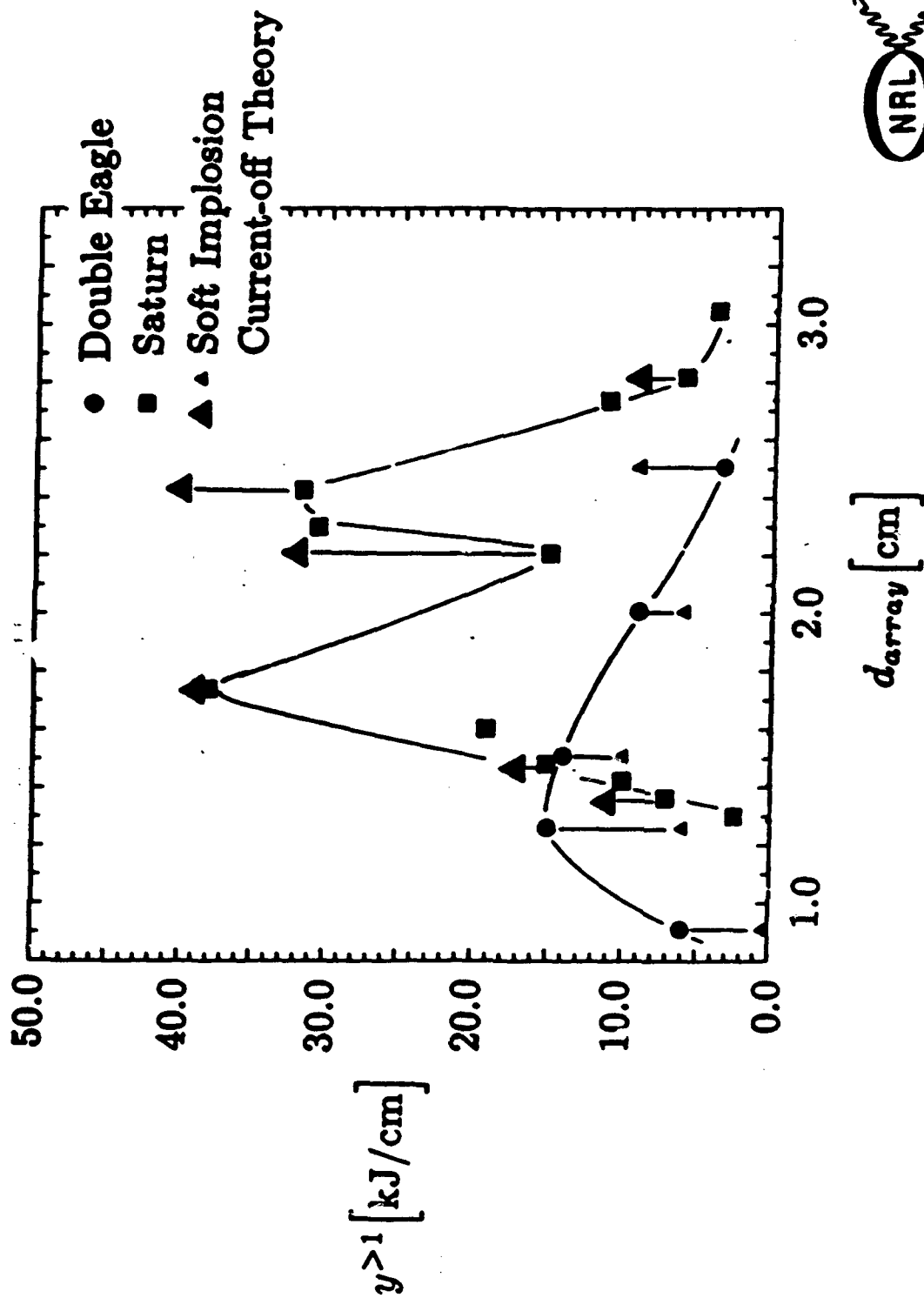


Fig. 12

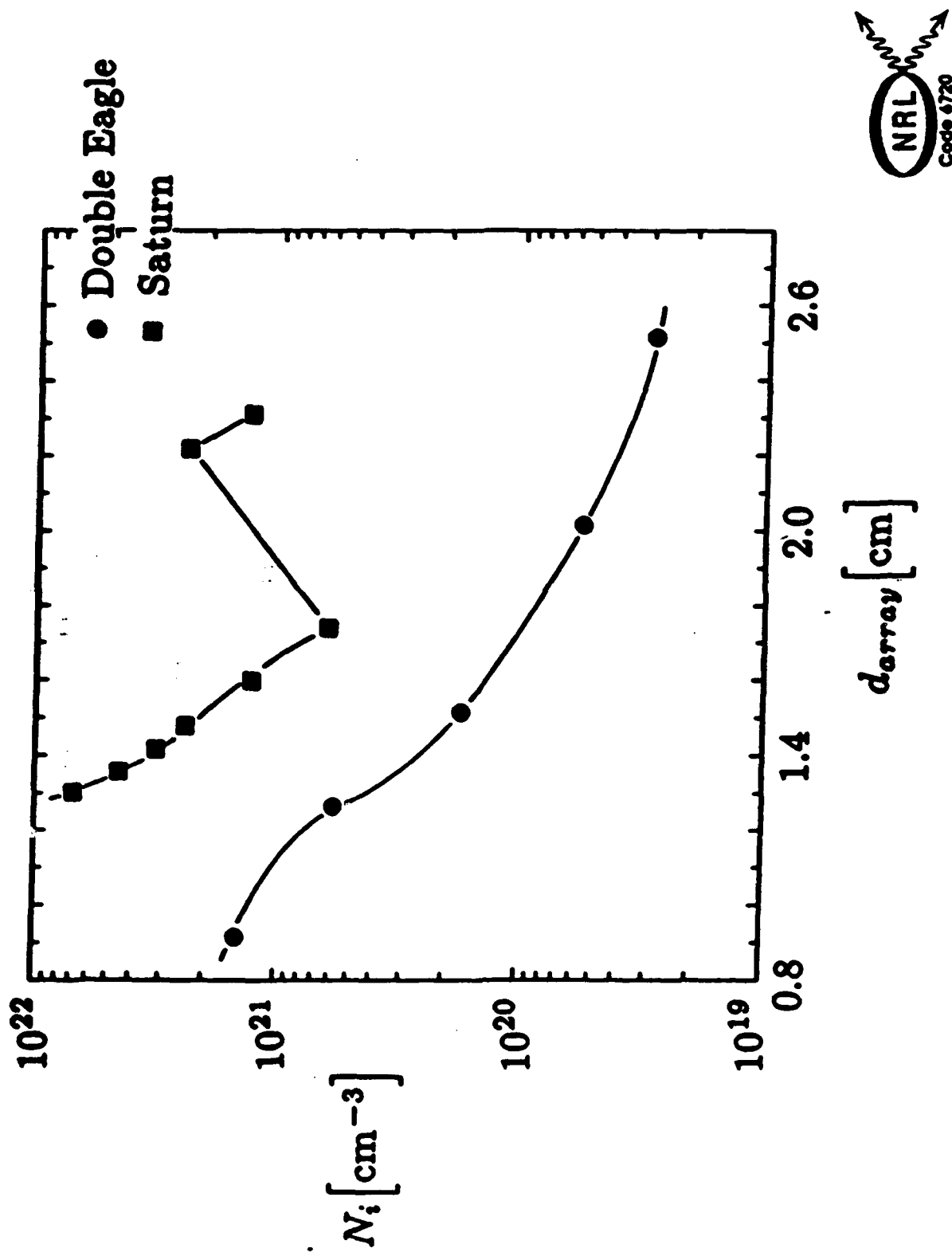


Fig. 13

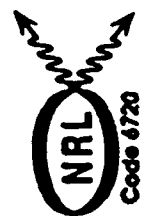
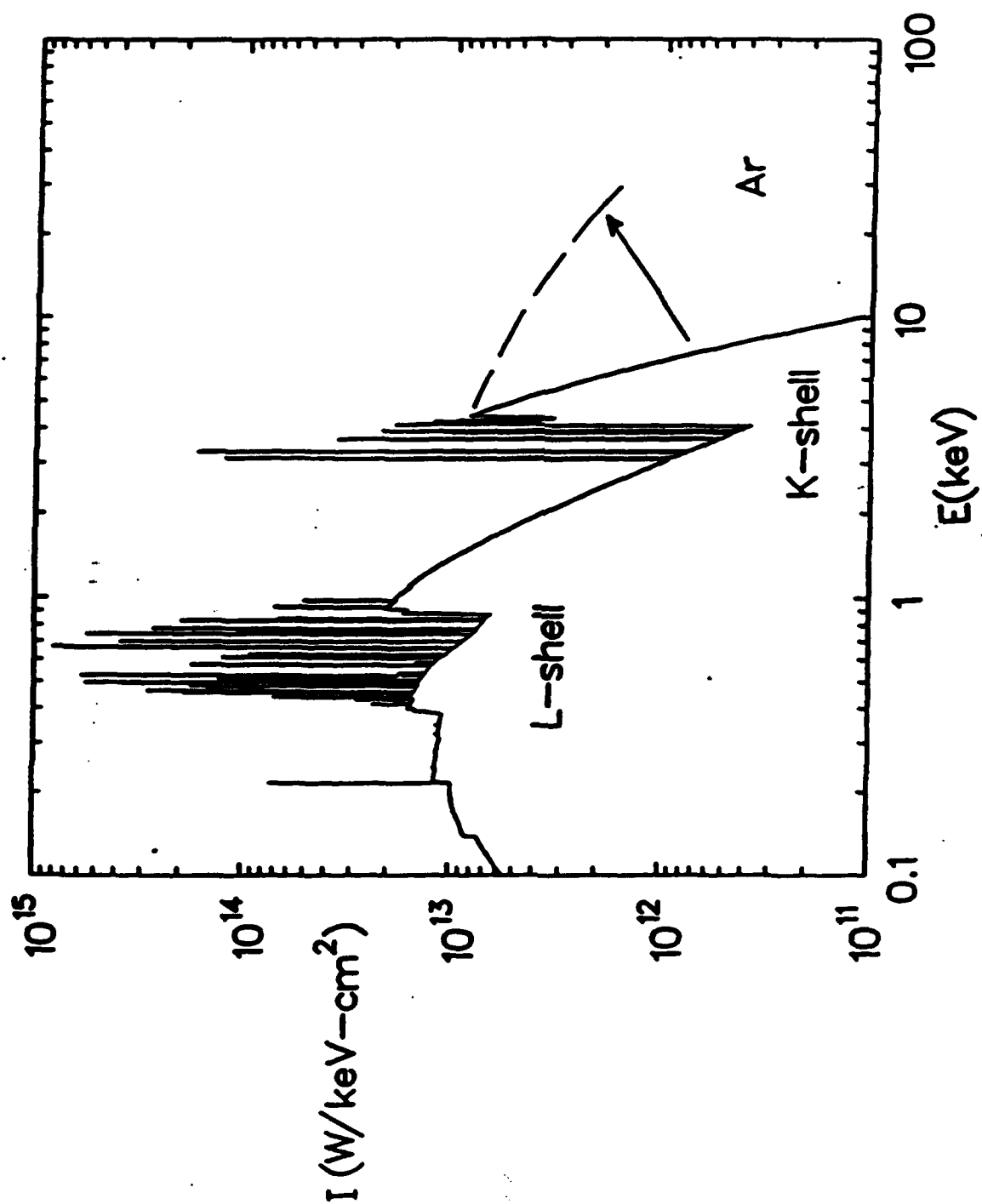


Fig. 14

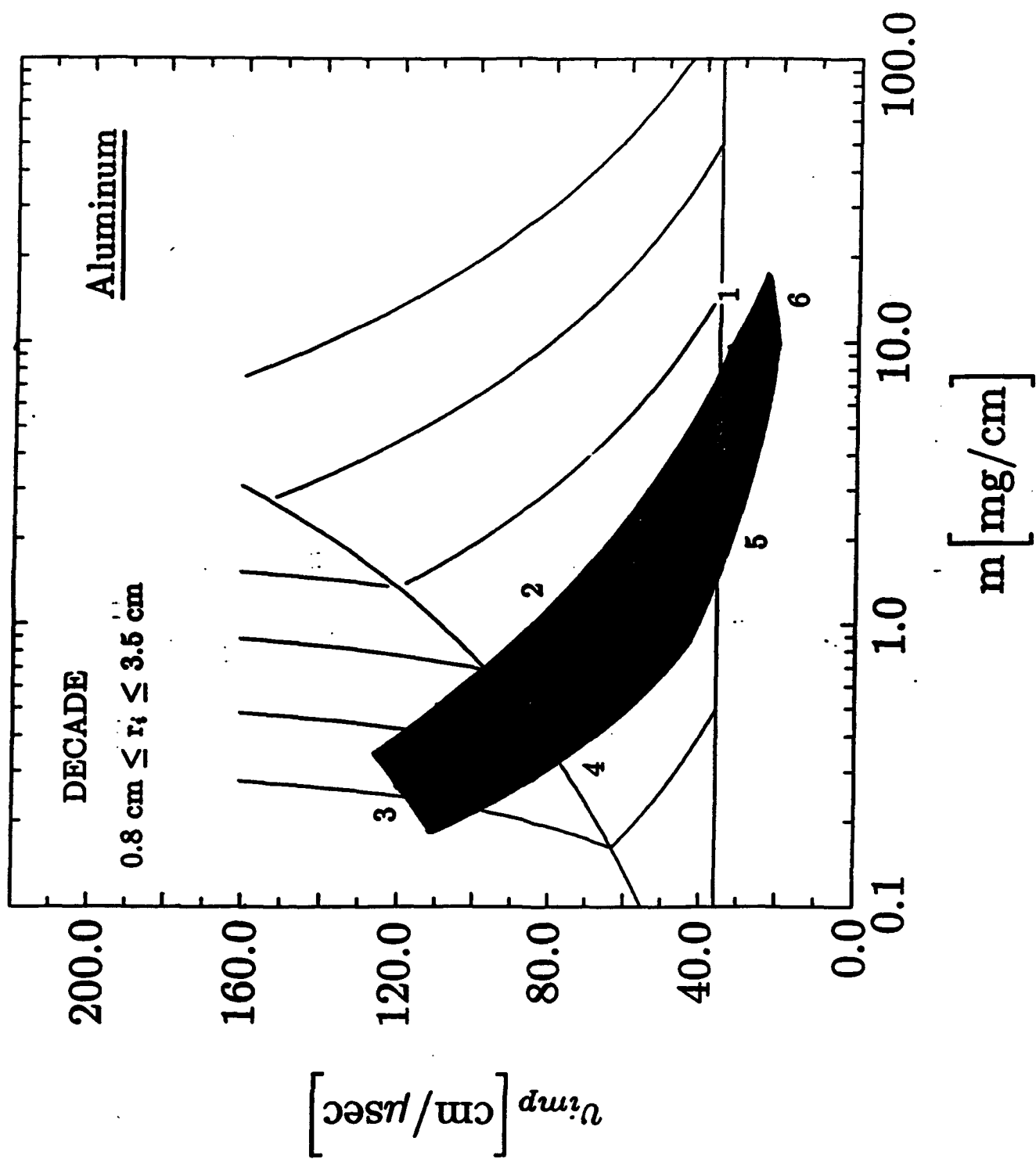


Fig. 15

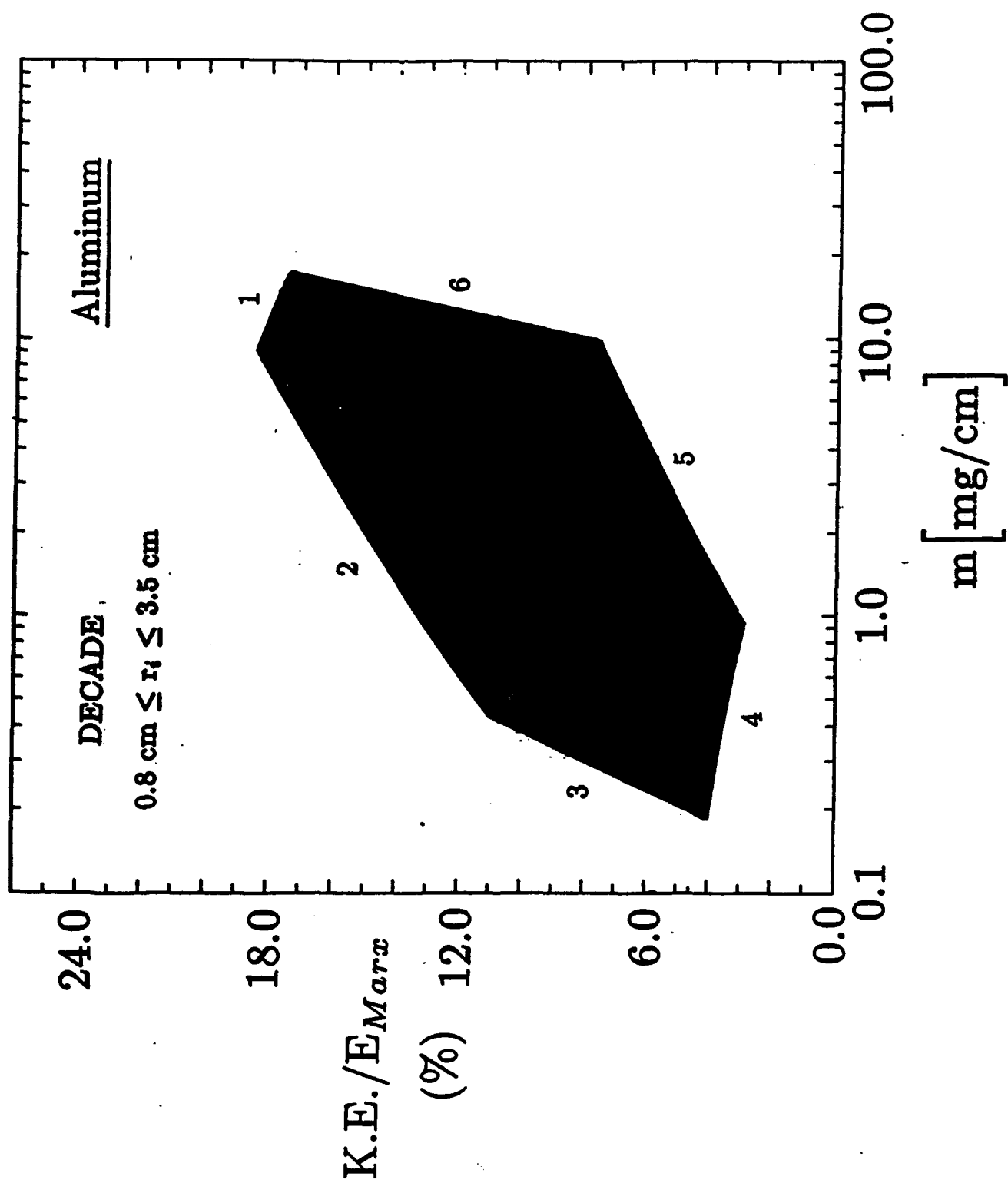


Fig. 16

II. ONE - DIMENSIONAL MODELING OF Z-PINCH IMPLOSIONS

One of the major tasks of our branch is to provide continuing data analysis and guidance for z-pinch experiments performed on DNA simulators. A substantial part of this analysis has been facilitated by comparing experimental results with predictions for the plasma dynamics that are based on one-dimensional (1-D) magnetohydrodynamic (MHD) calculations. The 1-D models are very important because they present a reasonable tradeoff between the two goals of (1) simplicity and (2) sophistication - enough to model the problems of interest. Specifically, they provide important radial information (gradients in temperature, velocity, density, radiation, etc.) that is not present in simpler and less costly zero-dimensional (0-D) 1-cell models, which assume uniform plasma conditions. As an example, because of their lack of radial information 0-D models are unable to show, as the 1-D models are, that it is generally the core and interior regions of the plasma that generate most of the K-shell radiation.

Some problems, such as zippering, nozzle dynamics, and asymmetrical instability development, require multi-dimensional modeling by their very nature. Unfortunately, the models needed for these problems either do not exist or they are so costly that one must usually sacrifice accuracy in radiation transport in order to lower the cost of including extra dimensions. Because of the high cost, whenever the plasma motion is on average one dimensional it is advantageous to use a 1-D model.

Our 1-D models contain (1) a comprehensive description of the ionization dynamics of z-pinch plasmas, (2) an accurate description of the transport of radiation within these optically thick plasmas, and (3) the self-consistent coupling of these dynamics to each other and to the fluid dynamics. Even with these extensive capabilities early calculations^{1,2} predicted roughly two or more orders of magnitude larger ion densities on axis and correspondingly much shorter radiation pulse widths than were seen in experiments.^{3,4,5,6,7} Because of the lack of agreement between calculations and experiment we have developed over the course of the last two years a phenomenological model for plasma turbulence that provides much better agreement between the experimental and calculated state of the stagnation plasma (see Refs. 4, 8, and 9). A summary of this work is given below.

Summary of Phenomenological Modeling of Turbulence

Based on the lack of agreement between calculations and experiment and on 2-D MHD z-pinch calculations^{10,11,12} which showed the possibility of large 2-D flow effects, it seems likely that some of the missing physics in the 1-D description of the z-pinch implosion dynamics is the onset of a 3-D hydromagnetic turbulence.^{13,14} In this case, a 1-D calculation with modified transport coefficients might more realistically describe the implosion dynamics provided the turbulence were uniform and the implosion was, on average, 1-D.

To test this hypothesis, we employed a phenomenological approach in order to incorporate turbulence effects into our 1-D MHD calculations. Multipliers were introduced for the plasma (artificial) viscosity, the heat conductivity, and the electrical resistivity. It was then possible to make an appropriate choice for these multipliers so that the calculations produced approximately the same plasma conditions at stagnation as a Physics International aluminum wire array experiment. In particular, comparisons between experiment and calculations were made for the average stagnation ion densities and electron temperatures as well as for the size of the K-shell emission region and the mass fraction of the plasma emitting in the K-shell.

We found that it is necessary to have large multipliers on viscosity and thermal conduction in order to achieve reasonable agreement with the experimental stagnation conditions of a variety of both argon gas puff and aluminum wire implosions. Large multipliers on viscosity are effective in lowering the stagnation ion densities and large multipliers on thermal conduction are effective in convecting energy out of the hot core, thereby heating more plasma to temperatures that are conducive for K-shell emission while simultaneously lowering the core temperature. It is difficult to determine a unique set of multipliers that gives the best representation for all of the experimental parameters, but it was found that the calculated stagnation conditions do appear to be somewhat insensitive to the choice of multipliers as long as large multipliers are selected. In particular, the choice: 40 for viscosity, 30 for heat conduction, and 20 for resistivity, provided reasonable agreement with all of these experiments, and substantially better agreement than had been achieved in the non-turbulent calculations (see Figs. 1-3). This agreement would appear to provide supporting evidence for the presence of plasma turbulence in z-pinch experiments. This phenomenological approach to the modeling of turbulence in z-pinch implosions based on

benchmarks to experimental plasmas may provide useful guidance for future work that involves the modeling of turbulence in these implosions from first principles.

If z-pinch radiation sources are scaled to higher current machines, then it will be important to know how turbulence phenomena in these plasmas will scale as well. The simplest assumption to make is that it will be as strong in higher current machines as it is in present-day machines. For this reason, we recalculated the yield scaling with mass for both aluminum and argon plasmas using the same transport coefficient enhancements as had been determined in the analysis of the PI aluminum and argon experiments. Softening the implosions has the consequence of requiring substantially more mass (factor of 6) to achieve efficient K-shell yield scaling (for $\eta = 4$) (see Figs. 4 and 5), since turbulence lowers the stagnation ion density for a given mass loading. Consequently, the ability of the plasma to radiate is diminished for a given mass, and the radiative capacity can be increased only by imploding more mass. This factor of 6 has been of major importance for making future predictions about the K-shell yield performance of DECADE and JUPITER simulators.

Future Directions of 1-D Z-Pinch Modeling

From our work on phenomenological modeling, which includes making numerous comparisons between experimental and calculated results, we know that there is still a great deal to learn and understand about z-pinch behavior. It will be necessary to obtain this knowledge and understanding in order to design the plasma radiation source (PRS) loads that DNA requires of its future simulators. Below we discuss a few of the areas of z-pinch research that we are investigating with our 1-D modelling capabilities. Note, there are many multi-dimensional problems, such as optimal nozzle design and minimizing instability growth, that are described in other sections of this report.

(a) post implosion modeling and short circuiting

For implosions that occur late in the current pulse and for those machines which cannot put much current into the load at stagnation because of large induction, late time current flow and confinement may not be so important for determining K-shell emission. However, for several of the Double Eagle argon, krypton, and aluminum experiments that produced substantially more K-shell emission than predicted by current-off turbulence calculations, it is likely that an accurate

model of the late time current effects is needed. The straightforward approach of just allowing the current to flow during stagnation produces results which are not generally in accord with experiment. For example, calculations made for low mass loads such as the 42 $\mu\text{g}/\text{cm}$ Physics International (PI) experimental argon load show that keeping the current on leads to K-shell yields more in accord with experiment but it also leads to an elastic bouncing behavior that causes the K-shell radiation to be emitted over 100 ns (see Fig. 6). Neither the bounce behavior or the long emission times are characteristic of the experiment. One can speculate that part of the long emission time behavior could be due inherently to the 1-D nature of the model, which only allows uniform radial motion. If the theoretical plasma is allowed to move axially after stagnation, then part of the stored internal energy will not be available to do work against the magnetic field. The result will be a smaller radial expansion and a shorter time between radial contractions.

As another example, current-on calculations made for the more massive PI aluminum loads (474, 277, and 164 $\mu\text{g}/\text{cm}$) produced radiative collapses for which there was more energy coupled into the load and radiated in the K-shell than was observed in the experiments. For this reason we will continue to investigate the possibility of alternative current paths and shorting of the diode which could reduce the energy coupling to the load and magnetic field confinement of the plasma. Some of this work as it relates to Gamble II and Double Eagle was presented in the 1990 DNA annual report. More recently, a short circuit analysis of the Saturn aluminum experiments showed that the total radiative yield behavior that was exhibited in the experiments had the same trend as the energy coupled into a shorted diode. The following example is for a short that occurs when the voltage across the diode is 3MV.

Mass $\mu\text{g}/\text{cm}$	Anode radius (cm)	Total Exp. Radiation (kJ)	Coupled Energy 3MV short (kJ)	K-shell Yield Exp.-(kJ)	K-shell Yield Theory - (kJ)
120	2.4	172	235	8	14
160	2.4	170	258	12	20
185	2.4	196	278	22	24
330	2.4	331	346	63	79
470	2.4	364	383	61	120
740	2.4	338	433	30	76

While this work does not supply 100% conclusive evidence that shorts are playing a predictable role in the dynamics of the implosions, it does demonstrate that shorts deserve more experimental and theoretical consideration.

(b) generating > 30 keV photons

Our estimates, which are based on applying current K-shell yield scaling results to xenon ($Z=54$) plasmas, show that at best tens of kilojoules of 30 keV photons might be obtained using Jupiter class machines (see Appendix). To address the problem of attaining significant yields (hundreds of kilojoules) of > 30 keV photons using future simulators, we began an investigation into examining the efficiency of producing high energy recombination photons. This scheme entails using a z-pinch to heat the core of a moderate Z material, Ni for example, to very hot temperatures and then rely on radiative recombination to the heliumlike and hydrogenlike states to produce the high energy photons. Thermal bremsstrahlung is also present but its coefficient is substantially smaller than that for recombination radiation. Since the free-bound (and Bremsstrahlung) emission is proportional to $Z^3 Ni^2 \exp(-\frac{h\nu}{kT})$, there should be proportionately more photons coming out at high energy as the core temperature of the plasma is raised. We do not expect to attain efficient yield scaling of 30 keV photons using this scheme; however, we do feel that we can do better than would be attained by imploding xenon on Jupiter. The major reason behind this speculation is that the stagnation density (Ni) is much larger (which implies the radiation efficiency can be larger) when imploding large mass moderate z plasmas as opposed to low mass high z plasmas.

The study we are initiating involves fixing the mass of a nickel plasma at $2000 \mu\text{g}/\text{cm}$ and fixing the initial radius at 2.0 cm. The load is then imploded using a linearly ramped current profile that is terminated when the outer radius of the pinch reaches 0.2 cm. Under these conditions we found that the > 30 keV radiation is a maximum for a current profile which produces a peak current of 51 MA in 50.4 ns. The work done on this plasma is $\cong 4 \text{ MJ}/\text{cm}$, which is well within the realm of a Jupiter class machine. Fig. 7 shows what the predicted yields are above each energy level for the 51 MA calculation and in particular it shows that 27 kJ/cm of > 30 keV photons are being produced. Since we have only sampled a small portion of the available parameter space in terms of mass loading and energy coupling to the load there is good reason to be optimistic that more than 27 kJ/cm of > 30 keV radiation can be generated by Jupiter class machines. We are

also investigating DECADE's capability of producing > 20 keV photons.

(c) diagnosing core physics

Because our 1-D model uses cell-to-cell coupled probability of escape techniques to transport radiation^{15,16,17} there is an inherent uncertainty in inferring the final emitting zone of an escaping photon because of the averaging over the line profile. Thus, spatial comparisons between the sizes of the experimental emission regions, which are based on x-ray pinhole pictures, and our calculated sizes are somewhat problematical. This has not been a problem for analyzing the PI experiments because it was usually only the inner regions of the plasmas that were hot enough to ionize into the K-shell while the outer regions remained too cold and underionized to be effective reabsorbers of K-shell radiation. Therefore, even though the exact zone from which a K-shell photon escaped was unknown, the size of the source region of plasma from which it escaped, in these calculations, was fairly well defined. However, when we began an analysis of the Saturn aluminum data we found evidence that this is not the case. For example when we apply the spectroscopic techniques of Coulter et al.¹⁸ to the Saturn data we find that the average temperature of the K-shell emission region of the best K-shell emitting load ($330 \mu\text{g}/\text{cm}$) is 600 - 900 eV with approximately 30 % of the mass participating in producing K-shell emission. The problem is that the 600 - 900 eV temperatures seem to be much lower than expected because we know that similar mass loadings for argon have produced considerable K-shell emission on Saturn, which would require much higher temperatures. This is also in accord with our 1-D analysis which shows the average K-shell emission region temperature to be approximately 1600 eV. It is also in accord with an earlier study in which we applied our spectroscopic technique to a 1-D aluminum calculation¹⁸ and found that the spectroscopic averaging process predicted smaller temperatures. At this point we are investigating the possibility that there is substantial absorption and reemission of K-shell radiation taking place in cooler regions of the Saturn plasmas that are affecting the Lyman and He-alpha line ratios and consequently our spectroscopic analysis.

In the past we have always distributed some mass of the plasma all the way to the axis. This procedure has provided numerical stability by providing back pressure early in the stagnation that softens the implosion. This procedure may be adequate for gas puff simulations because of the divergence of the gas from the nozzle towards the axis, however, it is not clear that wire

array implosions behave in this same manor. Therefore we have begun an investigation into the differences in stagnation dynamics between a shell implosion, which may be more indicative of a wire array experiment, and a snow plow implosion, which is more characteristic of a gas puff calculation.

Appendix: Simple K-Shell Yield Scaling

After conversations with members of the PRS community it became apparent that several members were having difficulty in applying our PRS K-shell yield scaling results to DECADE and JUPITER class machines. Apparently, the community is interested in a singular choice of initial load conditions that will optimize K-shell emission, whereas, our results predict that there is a broad range of mass loads and initial radii that will produce nearly the same optimal K-shell yield from a given element and machine. In order to facilitate usage of our work by the PRS community we decided to propose our own simple K-shell yield scaling relation. This relation makes a singular judicious choice of initial load conditions that is founded upon the principles of our earlier 1-D scaling work. Based on the kinetic energy coupling E from the machine to the load this scaling relation predicts the optimal mass load M_{opt} and the expected K-shell emission as a function of atomic number Z of the load. The initial radius can be found using a simple slug model or, if it is applicable, a sinusoidal model can also be used. The scaling relation is derived by calculating the largest value of η , defined as η_{max} , that can be achieved, for a given machine kinetic energy coupling to the load E (j/cm), while still imploding enough mass to insure efficient K-shell yield scaling. That is η_{max} satisfies the equation

$$\eta E_{min} M_{BP}(\eta)/A = E \quad (1)$$

where A is the atomic mass (g), E_{min} is the minimum energy needed to ionize into the K-shell (j/ion), and M_{BP} is the break-point mass (g/cm). All of these quantities are defined in Ref. 2. Note M_{BP} has been phenomenologically determined to be a factor of 6 greater than the value quoted in Ref. 2.⁶ A useful approximation for the kinetic energy coupling E is given by

$$E = 1607 I^2 \quad (j/cm) \quad (2)$$

where I is the peak load current (MA). Equation (1) can be solved numerically for η_{max} or it is

given approximately by

$$\eta_{max} \cong (6.3 \cdot 10^5 E/Z^{7.51})^{1/3} \quad \text{for } \eta_{max} < 7. \quad (3)$$

The K-shell yield scaling Y_k (j/cm) is given by:

$$Y_k = 0.3E \quad (j/cm) \quad \text{for } \eta_{max} > 2.0 \quad (4)$$

$$Y_k = 0.3E(-\eta_{max}^2 + 4\eta_{max} - 3) \quad (j/cm) \quad \text{for } 1.25 < \eta_{max} < 2.0$$

The optimal mass loading $M_{opt} = M_{BP}(\eta_{max})$ and it is approximately given by

$$M_{opt} \cong E^{2/3} 1.7 \cdot 10^{-7} \quad (g/cm) \quad \text{for } 1.25 < \eta_{max} < 7 \quad (5)$$

For $\eta_{max} < 1.25$ the following relations apply

$$M_{opt} = 1.3 \cdot 10^{-5} E/Z^{2.552} \quad (g/cm) \quad (6)$$

$$Y_k = 1.3 \cdot 10^{10} E^3/Z^{15} (j/cm) \quad (7)$$

Equations (6) and (7) show that a Jupiter machine coupling 5 MJ/cm of kinetic energy to a load can expect to achieve 17 kJ/cm of xenon K-shell emission. Note, there is still a great deal of uncertainty in the yield scaling at low η .

References

1. J. W. Thornhill, K. G. Whitney, and J. Davis, J. Quant. Spectrosc. Radiat. Transfer 44, 251 (1990).
2. K. G. Whitney, J. W. Thornhill, J. P. Apruzese, and J. Davis, J. Appl. Phys. 67, 1725 (1990).
3. C. Deeney, T. Nash, R. R. Prasad, L. Warren, K. G. Whitney, J. W. Thornhill, and M. C. Coulter, Phys. Rev. A, 44, 6762 (1991).
4. C. Deeney, P. D. Lepell, B. Failor, J. Meachum, S. Wong, J. W. Thornhill, K. G. Whitney, and M. C. Coulter, "Radius and Current Scaling of Argon K-shell Radiation," accepted for publication, J. Appl Phys. (1993).

5. M. Gersten, W. Clark, J. E. Rauch, G. M. Wilkinson, J. Katzenstein, R. D. Richardson, J. Davis, D. Duston, J. P. Apruzese, and R. Clark, *Phys. Rev. A*, 33, 477 (1986).
6. R. B. Spielman, R. J. Dukart, D. L. Hanson, B. A. Hammel, W. W. Hsing, M. K. Matzen, J. L. Porter, in *Proceedings of the Dense Z-Pinches Second International Conference*, Laguna Beach, CA, edited by N. R. Pereira, J. Davis, and N. Rostoker (AIP, New York, 1989), p. 3.
7. N. Loter, P. Layton, D. Monjo, D. Parks, J. Rauch, W. Rix, P. Steen, E. Waisman, K. Ware, W. Wnuck, M. Coulter, and K. G. Whitney, *Bull. Am. Phys. Soc.* 36, 2400 (1991).
8. J. W. Thornhill, K. G. Whitney, C. Deeney, and P. D. LePell, to appear in *Phys. Plasmas* 1, February (1994).
9. K. G. Whitney, J. W. Thornhill, C. Deeney, P. D. LePell, and M. C. Coulter, in *Proceedings of the 9th International Conference on High-Powered Particle Beams*, Washington, DC, edited by D. Mosher and G. Cooperstein (NTIS, Springfield, VA, 1992), p. 2044.
10. T. W. Hussey, N. F. Roderick, and D. A. Kloc, *J. Appl. Phys.* 51, 1452 (1980).
11. T. W. Hussey, M. K. Matzen, and N. F. Roderick, *J. Appl. Phys.* 59, 2677 (1986).
12. C. Deeney, P. D. Lepell, F. L. Cochran, M. C. Coulter, K. G. Whitney, and J. Davis, *Phys. of Fluids B* 5, 992 (1993).
13. J. Dahlburg, private communication (1993).
14. T. A. Zang, R. B. Dahlburg, and J. P. Dahlburg, *Phys. Fluids A*, 4, 127 (1992).
15. D. Duston, R. W. Clark, J. Davis, and J. P. apruzese, *Phys. Rev. A* 27, 1441 (1983).
16. J. P. Apruzese, J. Davis, D. Duston, and R. W. Clark, *Phys. Rev. A* 29, 246 (1984).
17. J. P. Apruzese, J. Davis, D. Duston, and K. G. Whitney, *J. Quant. Spectrosc. Radiat. Transfer* 23, 479 (1980).
18. M. C. Coulter, K. G. Whitney, and J. W. Thornhill, *JQSRT.* 44, 443 (1990).

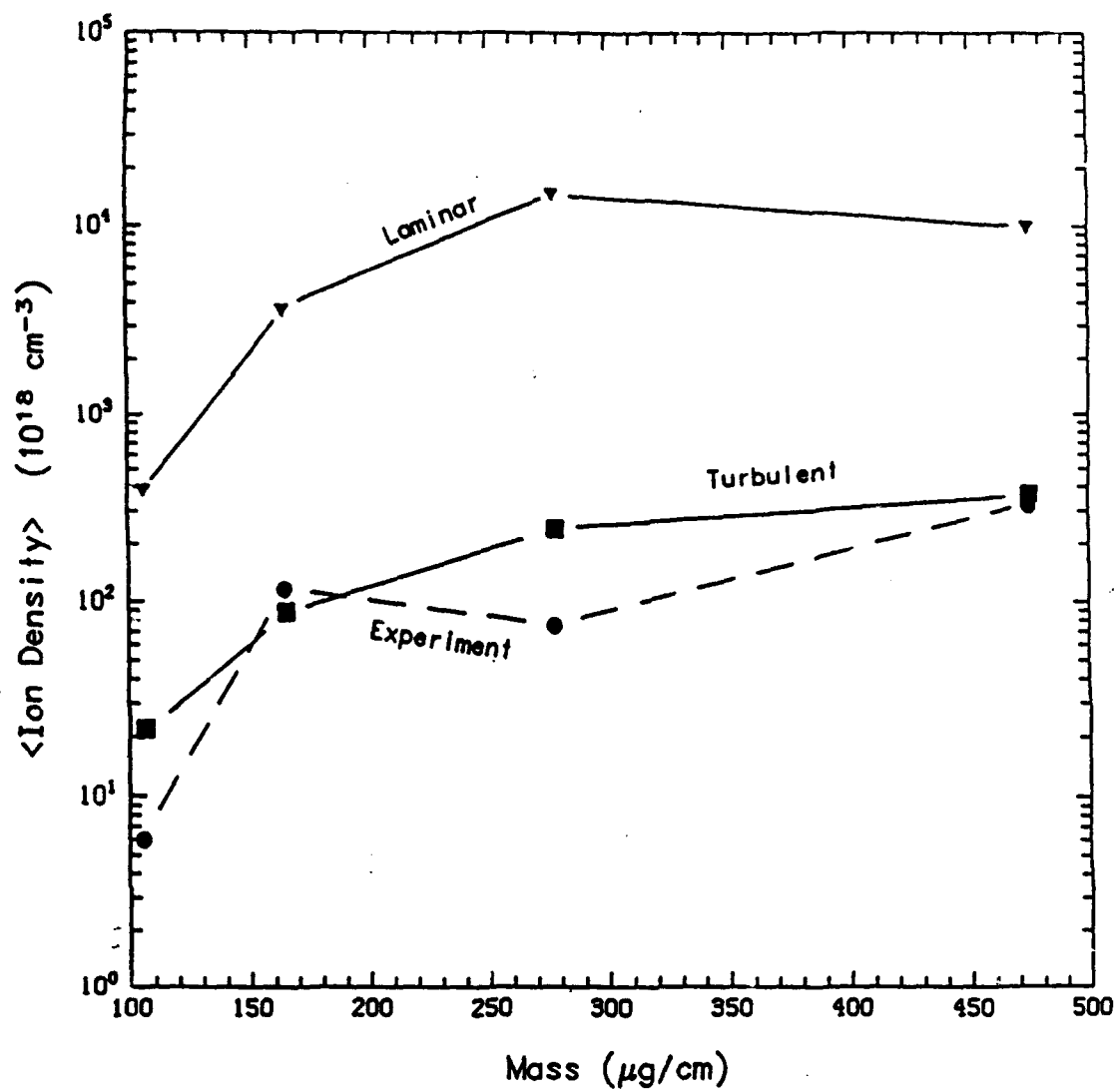


Figure 1. Laminar, turbulent, and experimental stagnation ion densities as a function of aluminum load mass.

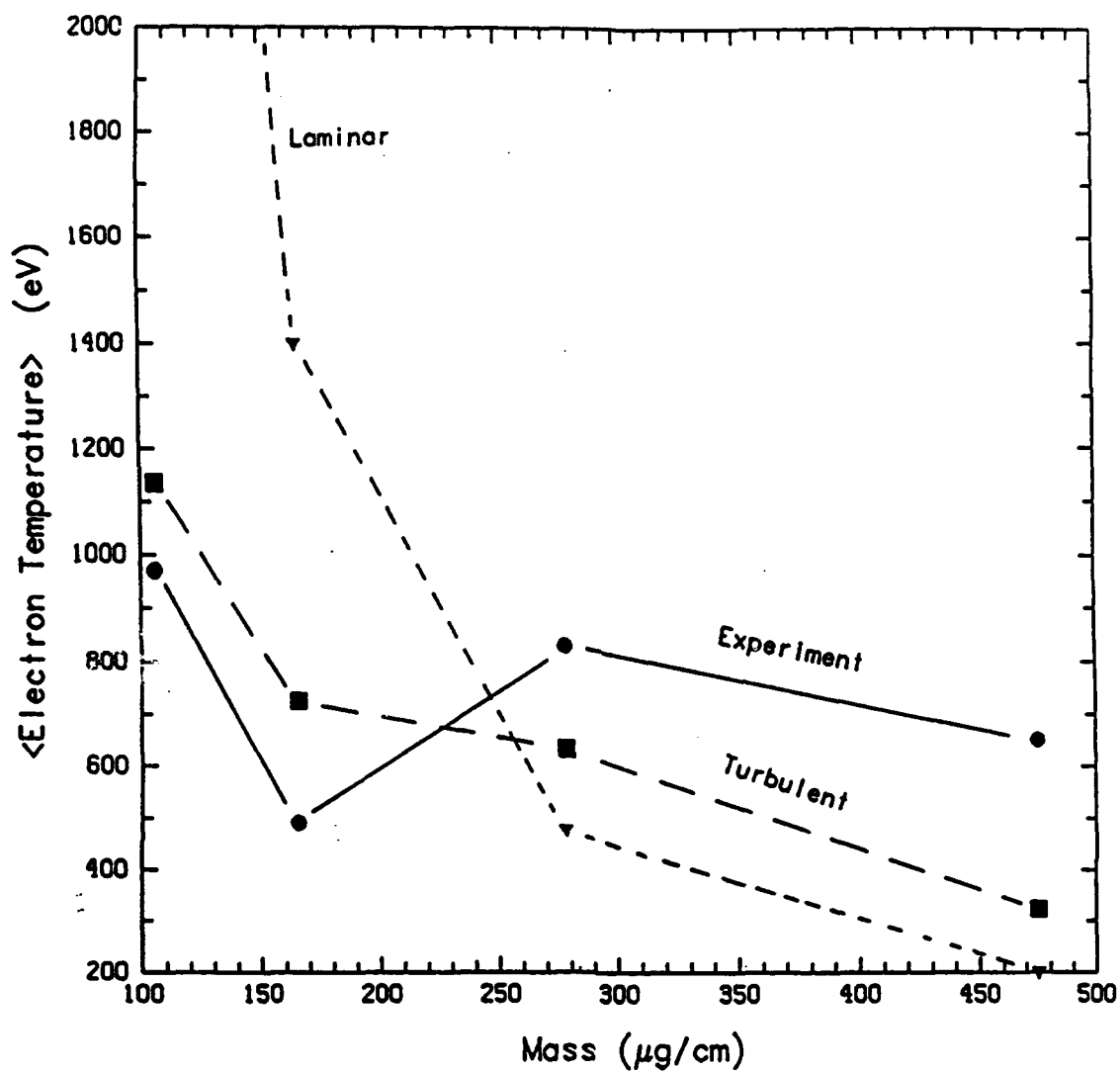


Figure 2. Laminar, turbulent, and experimental stagnation electron temperatures as a function of aluminum load mass.

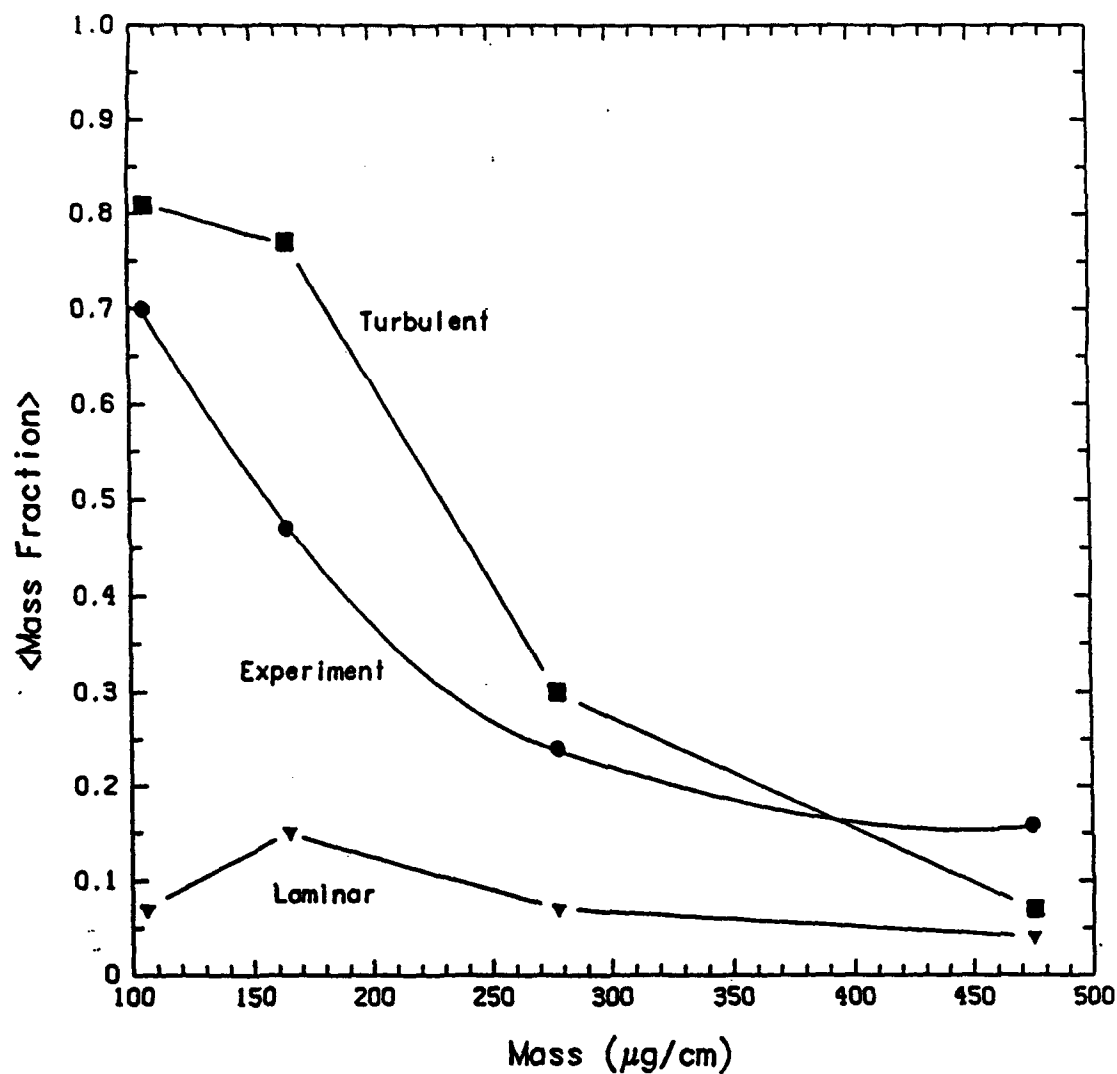


Figure 3. Laminar, turbulent, and experimental mass fractions of the plasma emitting in the K-shell as a function of aluminum load mass. The multipliers on the transport coefficients for the turbulent calculations are: 30, 40, and 20 for heat conductivity, viscosity, and resistivity, respectively.

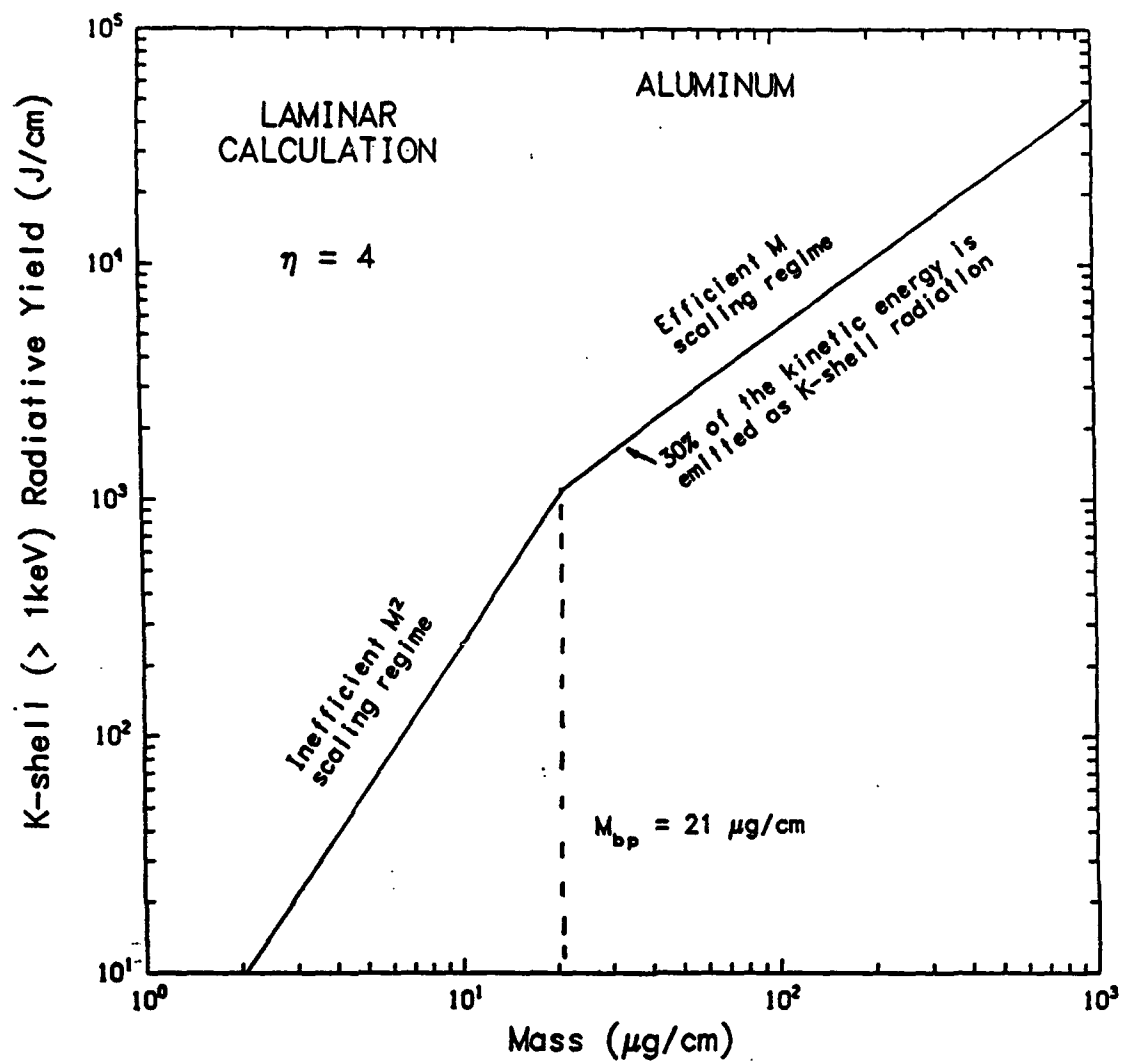


Figure 4. Non-turbulent aluminum K-shell yield scaling with mass for $\eta = 4$.

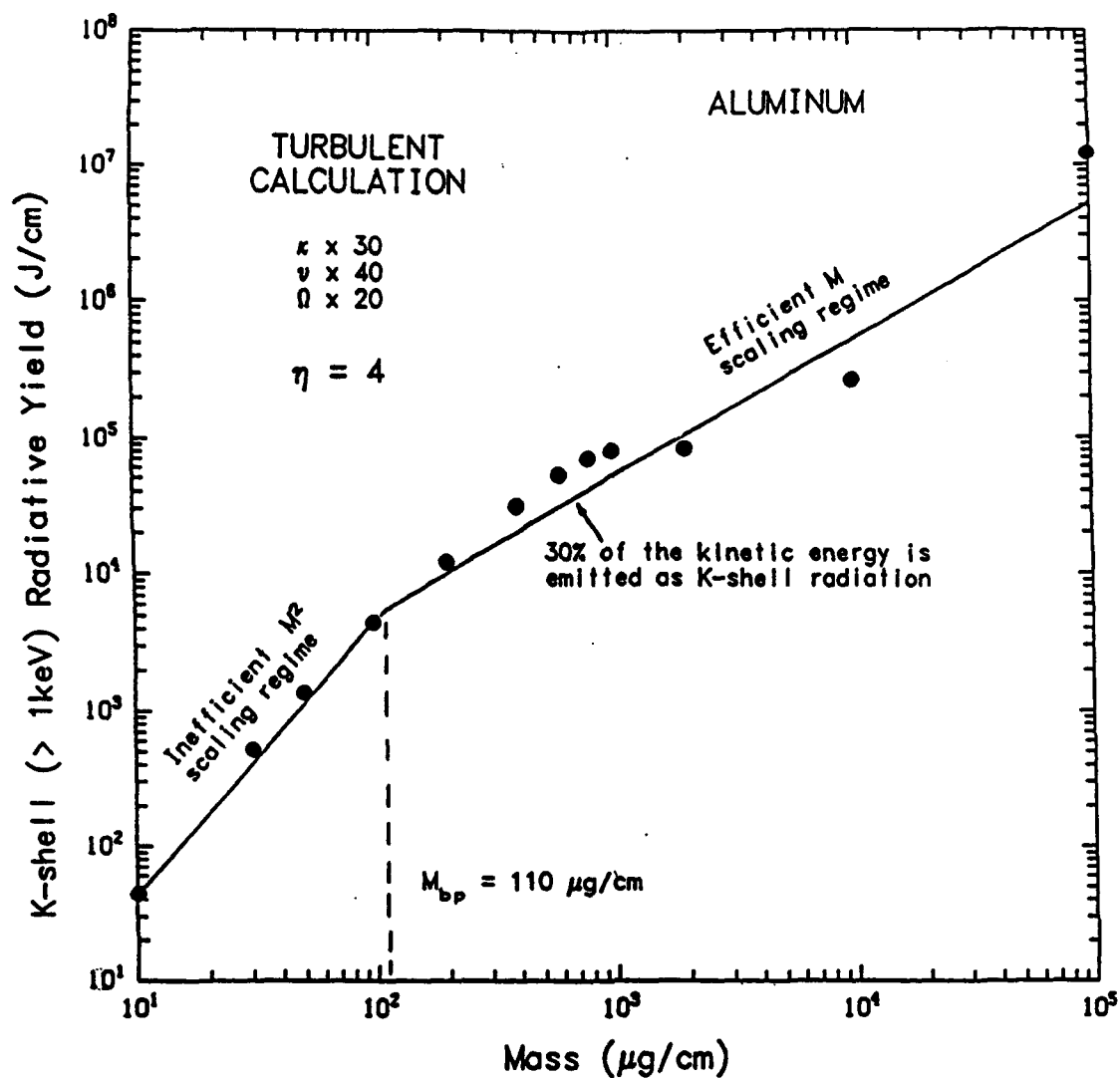


Figure 5. Turbulent aluminum K-shell yield scaling with mass for $\eta = 4$. The multipliers on the transport coefficients are: 30, 40, and 20 for heat conductivity, viscosity, and resistivity, respectively.

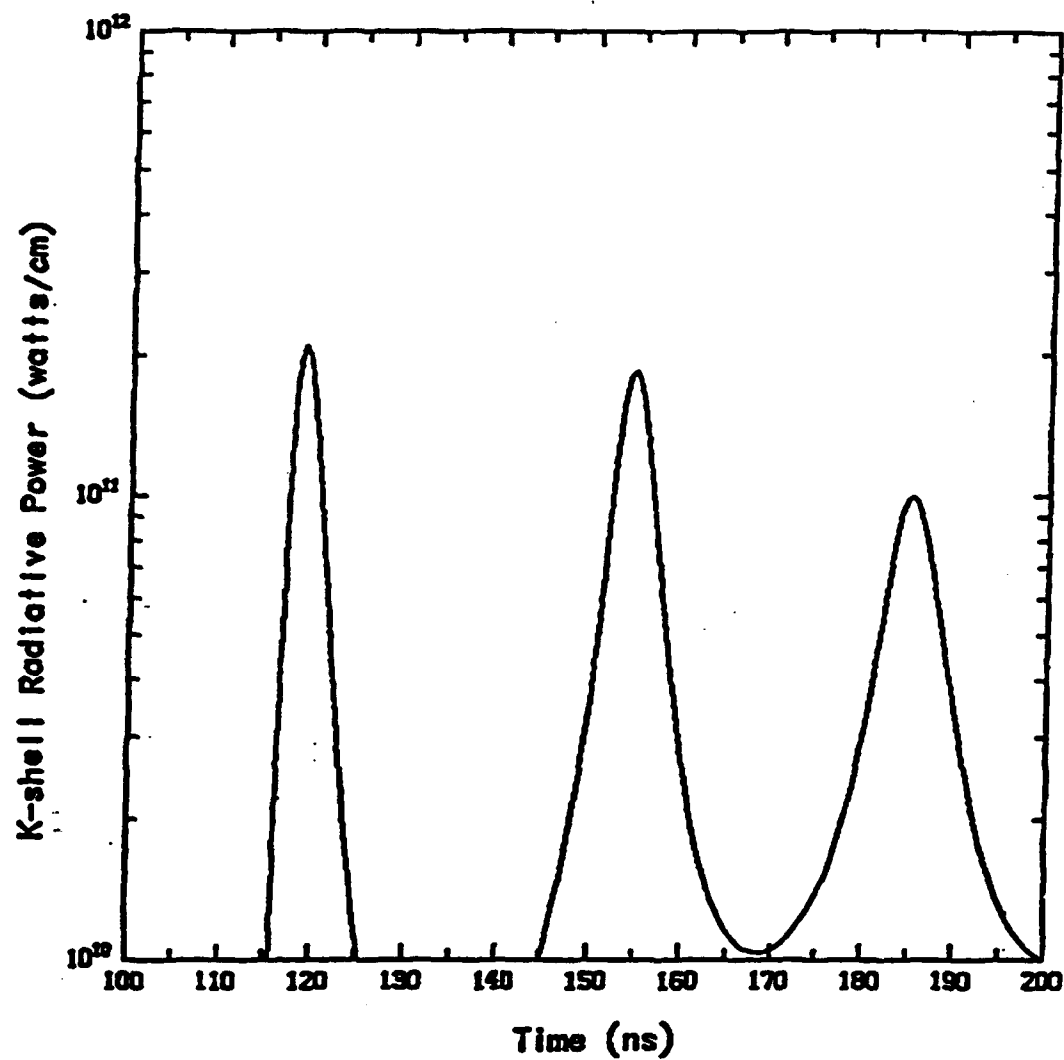


Figure 6. The calculated time evolution of K-shell emission power from a $42 \mu\text{g}/\text{cm}$ load is shown. In the calculation, the current and enhanced transport are kept on throughout several stagnation and rebound cycles of the pinch.

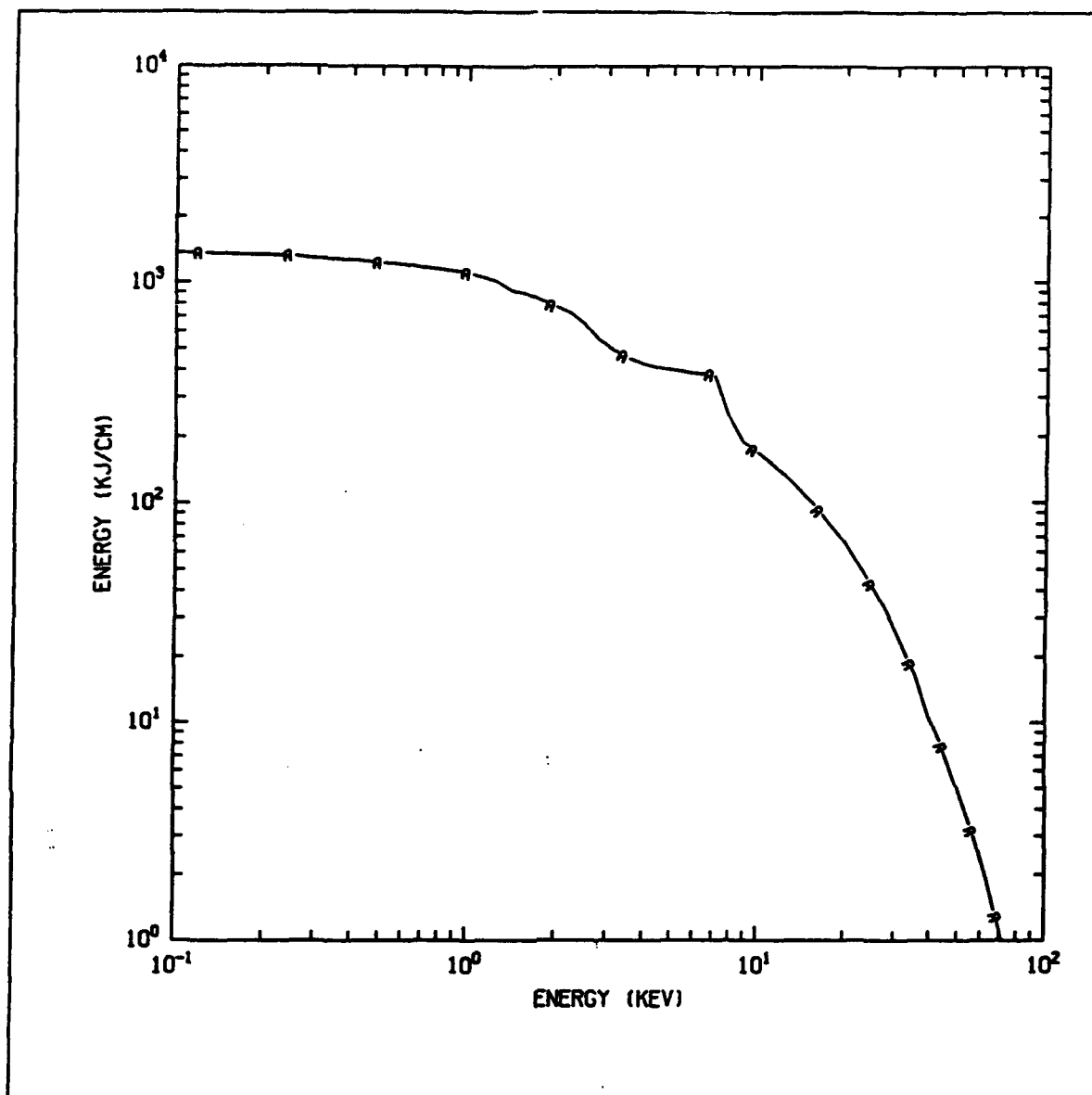


Figure 7. Time integrated emission above each photon energy level for a 2000 $\mu\text{g}/\text{cm}$ nickel load.

III. PRS Load Simulation

Throughout this past year, several topics in the area of 2-D modeling were addressed: (1) the viability of PRS loads in large current machines (i.e., on the order of 30 MA and larger), (2) Support of ongoing Gas Puff Experiments, and (3) code improvement and modification.

(1) Large Current Machines

During the past year, a large number of simulations were made which aimed at evaluating PRS loads on a hypothetical large current driver. We concentrated on 80 MA, 60 MA, and 40 MA peak current in the load during the runin from an initial radius of 8 cm (a 3cm diode length was assumed). These were Krypton gas puff loads. The driving current in these simulations used the circuit model with a 70 nsec switch time and a 12 nh inductor on the inductive store side of the circuit. An additional assumption was made that there is a total of 2.5 nh inductance on the load side of the switch which is coupled to an additional 2.5 nh short circuit load inductance. Naturally, this last source of inductance increases as the implosion proceeds and the radius decreases. The initial energy in the storage inductor was adjusted until the desired load current during the runin was achieved. The results from our 2-D computer code, PRISM, operating in a 1-D mode show peak K-shell yields of approximately 860 kJ/cm, 400 kJ/cm, and 100 kJ/cm for 80 MA, 60 MA, and 40 MA peak load currents. The yields were obtained for implosions occurring at 140 nsec and masses which were 3.3 mg/cm, 2.3 mg/cm, and 1.1 mg/cm, respectively. A caveat for these results is the fact that a radiation lookup table routine with no transport was used. This can overestimate the radiative yield when larger masses are used. For instance, 1-D results at higher mass levels show yields which decreased unrealistically as the mass was increased.

Our subsequent work on 2-D modeling have shown that loads which start at this large a radius are highly unstable (see discussion below). The requirement for smaller radii greatly reduces the kinetic energy which can be converted to radiation.

One of the important issues for large radii loads is the relevance of the Rayleigh Taylor (R-T) instability. We have modeled this instability in two-dimensions using

parameters relevant to PRS loads on future pulse-power generators. We examined implosions from a 10 cm radius, with a 3 mg/cm Krypton mass loading, and a 50 MA current in the load. In these calculations a moving mesh was used with the highest resolution concentrated in the vicinity of the peak density of the compressed shell. The mesh in these simulations was continually adjusted to remain at 10 cm by following the peak in the shell density in time. This simplification can be justified because the aspect ratio (radius of the shell/width of the shell $\gg 1$) is large. In addition, this procedure allowed us to start the 2-D instability runs with steady state profiles obtained from initial 1-D runs. In this fashion, compressive transients which could spoil the desired mode structure are avoided. These results have shown that the growth rate is on the order of $1-3 \times 10^7 \text{ sec}^{-1}$ up to 10^8 sec^{-1} for a wavelength roughly equivalent to the shell thickness.

Next, a series of simulations were made which started with initial 1-D solutions but in which the compressed shell was allowed to move through the mesh, i.e. implode. These annular gas puff shells exhibited Rayleigh-Taylor instabilities when accelerated from initial radii of approximately 10 cm. The instabilities were found to have a growth rate as high as $1-2 \times 10^8 \text{ sec}^{-1}$ which amounts to an e-folding time of 5 - 10 nsec. This is in agreement with the fixed location results discussed above. The somewhat higher growth rates come about because during the implosion, the acceleration increases as the pinch moves inward. In simulations of a gas annulus imploding from 8 cm, growth rates were measured as high as $1.3 \times 10^8 \text{ sec}^{-1}$ for short wavelength perturbations (50 MA peak current). Therefore, only 35 nsec is required for a 1 percent perturbation to grow exponentially to 100 percent. Obviously, this is well before peak radiation would occur at maximum compression on-axis. This disrupts the imploding gas well before the final collapse stage. In this particular case, the pinch had moved from 8 cm down to about 5-6 cm before disruption.

We further examined the stability of implosions with radii from 4 cm up to 10 cm. These implosions are driven by a simple circuit (described above) which consists of an inductor with roughly 120 MA switched into the load with a 70 nsec switch. This results in roughly a 50 - 60 MA driving current during the implosion. However, it is important to note that scaling laws can be applied so that the results should be similar for lower currents as well. For instance, changing the mass-radius

product, MR^2 , would result in a lower peak current, I , and shorter implosion time for the same circuit but \dot{I} would remain the same. Parameters within the circuit can be altered to adjust \dot{I} . A simple calculation shows why such a configuration is very susceptible to the classical Rayleigh-Taylor instability with growth rate $\gamma = \sqrt{kg}$, where $k = 2\pi/\lambda$ and g is gravity or acceleration. If one assumes an approximately uniform acceleration, a , the distance traveled by the shell is given as $d = \frac{1}{2}at^2$ where t is time. The amplification of the initial perturbation is then $e^{\gamma t}$, with $\gamma t = \sqrt{2kd}$. Note that this term is independent of both time and acceleration. It is well known that for shells undergoing acceleration, the most dangerous growth occurs when $k\Delta \simeq 1$ where Δ is the shell thickness which itself depends on the shell mass, acceleration, etc. For the moment, however, if we take $k=2\pi/0.2$ cm and assume that the shell is completely disrupted when a perturbation is amplified by a factor of 10^4 , the shell will travel only about 1.3 cm before disruption occurs. This is an idealized argument which assumes classical planar geometry with a sharp boundary. However, it is realistic enough to shed light on the difficulty in driving thin shells in from large distances as is being proposed for future PRS machines (i.e., DECADE and JUPITER). This is also consistent with the results cited above.

Simulated 2-D implosions using the circuit outlined above with two different fill conditions are presented in Figures 1 and 2. These simulations were for initial plasma configurations which are shells (i.e. $\Delta/R \gg 1$) and uniform fills.

Figure 1 shows the time history of the fraction of mass in zones with greater than 1.25 the average mass, the fourier component across the column of the mass difference for 4 nodes, and the fourier component for 2 nodes. The mass of the shell was 3.33 mg/cm (Krypton) in an initial shell configuration starting at a radius of 6 cm. The initial perturbation was introduced with a slight kinking of the column at four evenly spaced nodes. In Fig. 1, it can be seen that there is linear growth for the four node mode followed by a phase of more rapid growth during which the mass accumulates rapidly in the Rayleigh-Taylor spikes.

This accumulation is evidenced by the curve which shows that the fraction of mass in zones with greater than 1.25 of the average mass grows rapidly to 1. At the end of the run, the disrupted shell had moved to a radius of about 4 cm (i.e., over a distance of 2 cm). This is roughly the disruption distance given by the simple

argument outlined above and is not encouraging for a thin shell design which must implode over a large distance. Figure 2 shows the time history (the same quantities are plotted as in Figure 1) but for a uniform fill implosion with the same mass and circuit as in the shell implosion. In this case it can be seen that the initial mode grows linearly but is then suppressed while the 2 node mode grows and also is subsequently suppressed.

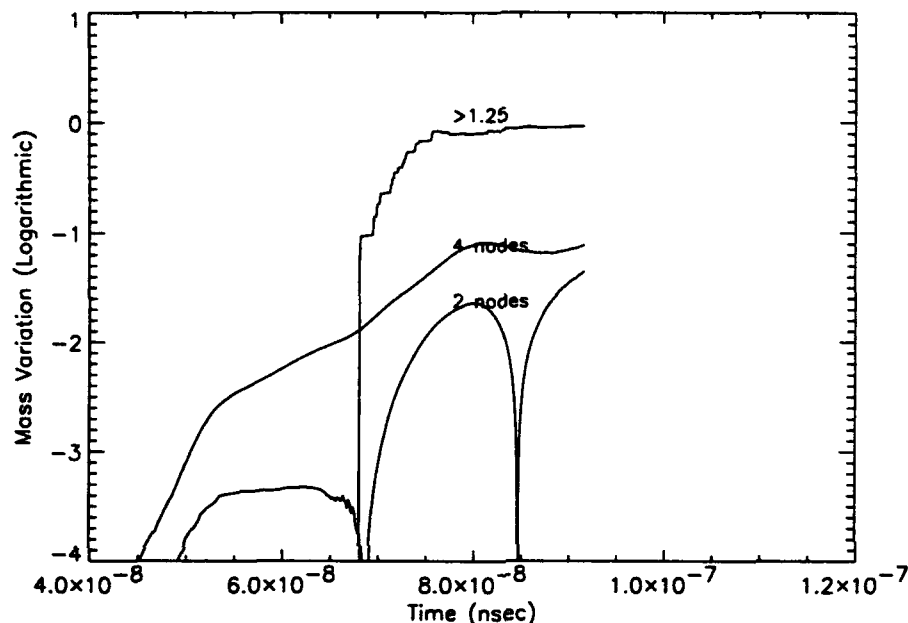


Figure 1 Fraction of mass in zones with greater than 1.25 the average mass and, fourier components of the mass variation for 2 and 4 nodes for a shell implosion.

The result is that the mass accumulation growth is delayed when compared to the shell implosion. The final state at about 112 nsec consists of a single node (i.e., $1/2$ wavelength) in the computational box with the dense portion of the plasma well inside 1 cm. This type of implosion offers hope that plasma may reach the axis over a long runin distance without being totally destroyed as happens with a thin shell. Recently, Gol'berg and Velikovich (Phys. Fluids B 5,1164(1993)) have proposed that an implosion of a uniform fill configuration can lead to some suppression of the Rayleigh-Taylor instability through accretion of mass onto the imploding shell. This work seems to support the results of our simulations. The penalty for such

designs, however, is that in uniform fill loads a large portion of the mass may not reach the required kinetic energy to significantly radiate in the K-shell.

The task in the upcoming year will be to optimize designs for large radii PRS loads which produce the necessary bulk kinetic energy while maintaining some integrity during the implosion. This investigation could have significant impact on the design of PRS sources for future pulse-power simulators.

Our conclusions to date on the stability of imploding loads to the Rayleigh Taylor instability can be summarized as follows: Imploding shells appear to break apart (over several cm of runin length) for the cases we have considered: 10 cm down to about 5 cm. Note that these are radius values, not diameters. A simple argument based on the acceleration determined from $d = 1/2at^2$ and a growth rate given as \sqrt{ka} , where k is the inverse wavenumber, gives a distance, d , of roughly 2 cm before significant breakup of thin shell would occur. Our simulations show that somewhere around a 3 cm radius, implosions of Krypton gas shells would seem to be viable. This analysis is based on the series of runs discussed above and the observed distances over which disruption occurred.

Uniform fill implosions present a different story. We have been able to bring the load in from 5-6 cm and have observed an interesting phenomena. That is, as the implosion proceeds, the snowplow picks up extra mass from the fill gas which broadens the shocked snowplow region and suppresses the initial wavelength. The result is that eventually only the longest wavelength available in the computational box ($1/2$ wavelength from $z=0$ to $z=z_{\max}$) is seen. For numerical resolution reasons, the length along z cannot be set to the size of the machine because the wavelengths are related to the width of the snowplow. This is much narrower than the diode length. Therefore, it should be noted that this result may be somewhat dependent on how large we set the size of the numerical box. Uniform fill implosions appear to be more stable than thin shell implosions. On the negative side, significant heating is seen in these implosions ahead of the snowplow which leads to hollow implosions. Currently, our effort is being directed toward assessing the role of radiation in these implosions. Analysis of the uniform fill runs show that the implosion velocities reach 5×10^7 cm/sec after about 65 nsec of a 100 nsec implosion. Near final implosion, it appears that velocities as high as 8×10^7 cm/sec can be achieved. This should

provide enough energy to produce Krypton K-shell radiation.

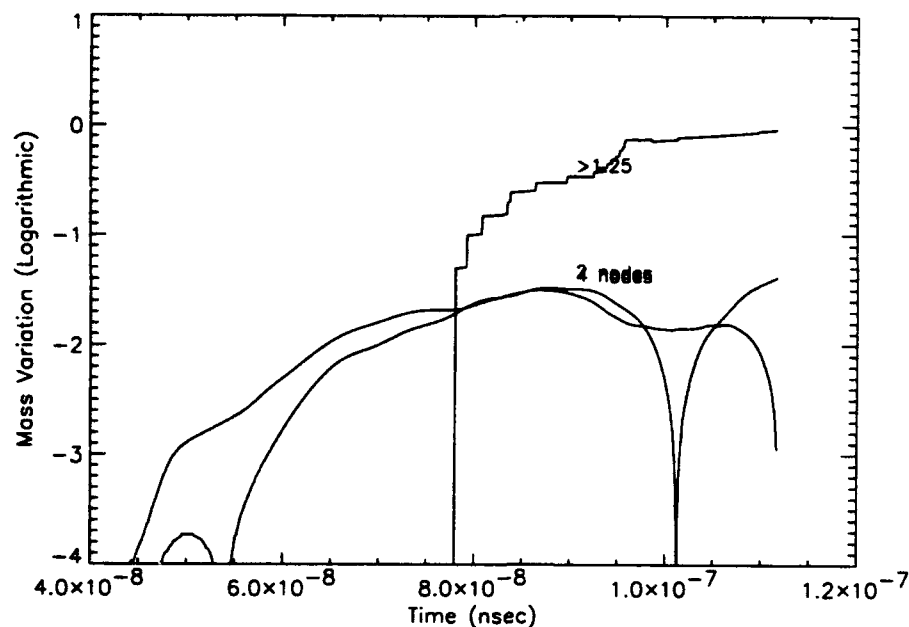


Figure 2 Fraction of mass in zones with greater than 1.25 the average mass and, fourier components of the mass variation for 2 and 4 nodes for a uniform implosion.

(2) Support of Ongoing Gas Puff Experiments

Several computer simulations were made in support of planned and ongoing experiments on the Double-Eagle pulse power generator at Physics International (PI). These experiments are designed to test new nozzles with smaller exit apertures. The narrowest aperture used to date has been 4 mm. In the new designs, this will be reduced to 2 mm. One of the important areas in which the NRL radiation-hydrodynamics branch can contribute in the future is to provide simulation studies of the gasdynamics of innovative nozzle designs. This is more important for upcoming machines where the tradeoffs discussed in the previous section requiring structuring the design with multiple puffs, for instance. This necessitates a clearer understanding of the nozzle gasdynamics. In the past, both our simulations and the PI experiments have shown improvement when the aperture was reduced from 8 mm to 4mm. However, simulations performed during this past year have shown

only small differences in yield when a further reduction is made to 2 mm. Table I shows the results for the standard Double Eagle parameters which have been used in the past. That is, 1.25 cm radius, 50 $\mu\text{g}/\text{cm}$ Argon mass, and 3.3 MA peak current. A linear current ramp model was used. Both nozzles were tilted inwards at a -10° tilt.

<u>Nozzle Exit Aperture</u>	<u>Yield</u>
0.4 cm	6 kJ
0.2 cm	5.2 kJ

Table I.

Examination of the simulation results show that thinner shells are more prone to breakup on the way in and appears to be the cause of the lower yield. This phenomena is similar to the results discussed in the previous section and demonstrates its relevance to current experiments.

The experimental schedule will now take this into account. Fewer of the new nozzles with 2 mm apertures are being constructed than had been originally planned. However, there will be a few shots made with the 2 mm aperture nozzles in order to compare simulation and experiment. This collaboration demonstrates that the cooperation between computer simulations and experimental planning can result in savings of time and money.

(3) Code Improvement and Modification

In support of our 2-D work on gas puff experiments, the computer code PRISM is being made available to several users. That is, it is presently making the transition from a single user environment to a multi-user production environment. This has required that the interface and post-processing packages be made more user friendly and adaptable. In addition to its use in simulating PRS load dynamics, PRISM will be used in studying the dynamics in other areas of interest to DNA such as switch plasmas. The code was modified so that it could run on the Los Alamos DNA Cray machines under UNICOS as well on large UNIX based workstations.

(4) Papers presented on this work

A paper on our previous work dealing with issues in 1-D and 2-D PRS implosions was presented at the Third International Conference on Dense Z-pinches at Imperial College, London. The abstract reads: "Non-LTE radiation hydrodynamic numerical simulations in 1-D and 2-D are performed for multi-terawatt driven argon and krypton gas puff loads. The influence of enhanced transport coefficients on the plasmas' implosion dynamics and the effects it has on the radiation yield and spectral distribution are discussed. Also presented are simulations for the performance of a krypton gas puff driven by a class of future drivers."

Some of the work discussed above was presented in an invited talk at the IEEE meeting in early June on the physics of PRS loads: Radiation Hydrodynamics of Z-Pinch Plasmas, J. Davis, IEEE Conference 7-9 June 1993, Invited Paper 4B5-6.

IV. DECADE Power Flow

• Coupling Issues for DECADE

The introduction of inductive energy stores (IES) to pulse power driven Plasma Radiation Sources (PRS) has made possible an order of magnitude or so reduction in the total size of the pulser modules and a potentially significant decrease in the risetime of the output current pulses. NRL is involved in a specific effort to understand power flow to the PRS load in an IES machine in support of the DNA DECADE simulator. As part of that program we have developed and tested a transmission line model that resolves the Plasma Opening Switch (POS), and connects that model to a simple "gas bag"^[1] PRS model. This work is intended to provide a simplified but comprehensive model to develop some scaling guidance for the design of PRS loads in DECADE. Several issues, such as: the low overall system efficiency, the possibility of POS restrike and other MITL losses, and PRS peak voltage, have been addressed.

The "gas bag" PRS model is used to assess the peak kinetic energy transferred to the model load, then a kinetic energy calibration model, based upon both the absolute load mass and the specific kinetic energy (per ion) delivered during the rundown phase, is used to estimate the expected yield. If K_{peak} is the largest kinetic energy transferred to the load, and \mathcal{N} is the total number of ions in the load, then the kinetic energy per ion can be normalized to the energy required to achieve K shell ionization and emission. The resulting ratio is a measure of implosion quality, viz. if

$$\eta \equiv \frac{K_{peak}}{\mathcal{N} 1.46 Z^{3.51}}, \quad (1)$$

is larger than 1, then ample energy has been supplied to excite the element's K shell. The theory goes further to relate the expected yield to the parameter η and the total mass relative to a mass break point which defines the boundary between efficient ($Y_K \propto \mathcal{N}$) and inefficient ($Y_K \propto \mathcal{N}^2$) yield scaling, viz.

$$\mu \equiv \frac{m}{m_{BP}} = m_i \mathcal{N} \frac{b(\eta)}{a(\eta)}, \quad (2)$$

where $a(\eta)$ and $b(\eta)$ are calibrated through fits to the 1-D MHD solution data. Further modifications to the yield scaling are folded in when $\eta \approx 1$ and when the stagnation radius is made larger than that seen in the calibrating MHD studies, but the result can be expressed as a simple function $Y_K(\eta, \mu)$ which is proportional to \mathcal{N} for $\mu > 1$ and \mathcal{N}^2 for $\mu < 1$.

• Power Flow in DECADE Point Designs

The detailed DECADE point design used here has a full specification^[2] elsewhere. An element by element summary description is shown here for the full (parallel) 16 module line in Fig. 1., and a single DECADE module (SDM) is obtained from this circuit by multiplying all the impedances by the number of modules, including the impedances of the convolute since the SDM is presumed to drive an short circuited convolute and PRS. In the SDM version of the model the current entering the POS element is not divided by the number of modules.

In a typical calculation the transfer capacitor (TC) is charged to 1800 kV, a level somewhat higher than the expected Marx charge. The overcharge serves to make up for energy that would continue to flow into the TC as it discharges into the POS and the inductive storage region formed by the PFL MITL. The water output line is long enough that only one pulse from the TC can ever interact with the model PRS load, the transit time from TC to load, back to the TC, and then back to the stack voltage monitor exceeds 300 ns. So long as model PRS rundown times are less than 200 ns, the model line will be an accurate representation of the full pulser shot, to include the voltage reversal and recoil of energy back to the TC that occurs at about 400 ns after the onset of the TC discharge. The stack voltage monitor signal point, shown on the figure, is a routine model output, as is the current *shunted* by the POS, and the load current at the feed MITL/convolute boundary. Feed MITL losses are modeled with additional shunts and attenuators in the area indicated. The convolute and load model has two design limits -- dubbed "low risk" and "sporty"^[3]. For transmission line calculations the sum of the delay times shown (1.76 ns) and the total inductance

of the front end options shown ($102.4 \rightarrow 71.56$ nH) can be used to set an impedance $Z = L/\tau$ for a single combined element lying between the feed MITL and the PRS load proper. Widening this inductance range somewhat ($105 \rightarrow 70$ nH) defines the "low risk" to "sporty" spectrum of inductances used in the energy coupling studies.

Turning to the POS element, it conforms to the PI design in physical dimension and appears to the primary transmission line as:

- i an input impedance (which varies with the time development of the conduction phase A-K gap upstream of the Hall snowplow),
- ii a lumped shunt, and
- iii an output impedance (which corresponds in a full line model to a 16 element parallel combination of lines with the listed anode and cathode radii).

In calibrating this POS model only one free parameter, the initial ion density, is available. A value of $6.25 \cdot 10^{12}$ ions/cm³ when used in the Hall snowplow conduction phase model established *both* the proper conduction time (≈ 290 ns) and the proper peak conduction current (≈ 2.05 MA) for the fixed length and radii of the PI design. This operating point is quite insensitive to the subscale gridding of the POS model, a $21 \rightarrow 41$ cell change in spatial resolution changed the peak conduction current by only 20 kA. The addition of the series resistance in the MITL changed these current values as well, bringing the peak conduction current down to 1.94 MA. All these changes are well within the expected range for enhanced resolution of the same physics, and, hence, we regard the present operation of the Hall Snowplow conduction phase model^[4] as adequate for the SDM point design. Again, the ambient density choice is the only free parameter in the simplified Hall snowplow conduction phase model, all other relevant lengths and times have been carefully set in accordance with the PI design specifications.

• The PRS in a DM1 Environment

The next task in the POS/PRS modeling effort was the establishment of the baseline performance of a single DECADE module (SDM) as conceived by PI. As

discussed above, the initial prediction of POS conduction time and peak conduction phase current was quite successful in that a choice of $6.25 \cdot 10^{12}$ ions/cc produced in the simulation both the correct conduction time (290 ns) and the correct conduction current (2.0MA).

Since the PRS is electrically isolated from the circuit during the conduction phase, any study of its properties should proceed from a fixed initial condition. In modeling the DECADE line, therefore, the POS conduction phase was computed up to a time just prior to the opening event and saved as a restart file. Having established this fixed conduction phase database, the rundown and stagnation of a model PRS load in the SDM was computed over a domain of several load masses on the order of $25 \rightarrow 200 \mu\text{g/cm}$. Early runs showed a poor energy coupling to these loads, on the order of 5 % of the energy available in the IES region, but this was due to an incorrect input to the models front end inductance. The addition of more inductance to the front end in modeling the SDM resulted, as expected, in the coupling of additional energy to the load, whether it was a matched load or a model PRS. For example, taking PIs general range of 3—7 nH for the parallel hookup, choose 5 nH and thus obtain an 80 nH single element fixed load inductance (prior to the PRS). The energy coupling rises to about 35 % of the energy delivered to the IES in the conduction phase. Of course the lumped inductance of the front end is only part of the line specification. The actual impedance jump at the transition into the front end is important in establishing the best model because the reflection coefficient for that interface plays a role in the complicated power coupling process that follows the POS opening. Since PI furnished the more detailed treatment of the SDM front end discussed above, allowing both the lumped inductance and the transition impedance to be taken into account, this coupled energy fraction has remained higher. In all the studies below which vary the POS and front end parameters into a fixed SDM PRS load, the overall front end inductance was constrained to the range of $70 \rightarrow 105 \text{ nH}$.

Having established a reasonable operating range for the SDM line model, in terms of POS and PRS feed parameters, the next logical step was to examine the details of

the model's operation for fixed POS parameters and a PRS mass near the optimum for energy transfer to the load. Note that optimum load cavity (or front end) energy transfer mass is usually not the optimum mass for kinetic energy transfer, but the two masses are close. Examples of the SDM operational scenario are shown below. In "SDM Line Profiles" (Fig. 2) the line's three propagation media (water, oil, and vacuum) are shown in the "bar legend" and the abscissa is in time delay [ns] along the transmission line. The current profile peaks at 2.05 MA just upstream of the POS, which is caught in the act of opening. About half the current resident in the IES is beginning to move toward the load. The voltage profile peaks at 11.8 MV just downstream of the POS, but this voltage is a factor of three or more greater than either the peak load voltage or the peak stack voltage seen later. The line impedance profile peaks at 22.4Ω at the oil/vacuum transition and constrains the profile of energy density to peak immediately upstream of the POS, viz. within the IES.

In SDM Line Waveforms (Fig. 3) are shown the time series for energies, voltages, and currents. No energy reflects from the matched load a resistively terminated inductance that matches the local output impedance of 4.5% at the end of the MITL. The load absorbs about 35 % of the energy delivered to the IES by the transfer capacitor. The load energy history and line input energy history are shown in the red and green curves. The load current peaks at about 2/3 MA, mostly due to the somewhat larger inductance of the front end parameters. Note that the load voltage peak is more than twice the stack voltage peak, due to different local impedances.

The surface plots compare the matched load and PRS with respect to current, voltage, and POS restrike. In "Line Current In Space and Time" (Fig. 4), the spatial scale is now physical path length (8m), and the broad yellow line cuts the surface at the oil/vacuum transition. The only significant feature distinguishing the two current histories is the null in line current that occurs for the matched load but not for the PRS. Comparing the "Line Voltage in Space and Time" (Fig. 5) histories, the PRS produces slightly higher peak voltages at opening all along the MITL section of the line. The MITL section is marked by a more open grid on the surface plot, arising

from the longer spatial increment for a fixed time delay. For either load the POS opening event sends a reflected voltage pulse back to the TC, then to be reflected again back toward the load. The secondary reflection might be artificial, due to an impedance jump in the model where it couples to the TC, but it has no effect on the PRS dynamics calculation because enough delay is built into the model output line to provide isolation. Comparing next the "Current Fraction Shunted" (Fig. 6) histories, the existence of a current null for the matched load forces a POS restrike (at very low current of course) because the low line current cannot magnetically insulate the gap, even when the full POS gap is quite large, as in the PI design. The restrike here shows the sensitivity of this particular numerical diagnostic to the restrike condition. So, even though the test cases chosen for the PRS model tend to show no serious restrike, the diagnostic would pick it up if the model line voltage and current solution predicted it. It would appear that current nulls are more dangerous than higher voltages in producing a restrike situation.

The next step after matched load studies was the addition of a PRS load in a mass range determined to provide load stagnation before 500 ns. Energy transfer to the load continued to be about what was expected from earlier work. In the case of the PRS load the details of the "gas bag" stagnation dynamics are shown on Fig. 7. Compared to the matched load, for the PRS the load current is a bit larger ($3/4$ MA), and the energy absorbed is down to about 10 % of the peak transferred energy. Stack and load voltages are comparable to the matched load case. The peak kinetic energy delivered to the load is 1.3kJ , while the inductance change is 13.6nH at peak compression, see below. A graphic summary of the SDM performance with a nominal 80nH front end and a PRS load is shown below (Fig. 8). In the line plots the normalizing value for any particular (color coded) quantity is shown in the legend accompanying the graph.

The overall electrical performance of the SDM calculation appears to be in fine agreement with the calculations done at PI when compared on the basis of line current and voltage waveforms. As a continuing effort to evaluate the model we furnished PI

a detailed graphic summary of the SDM model electrical output at the relevant test points for comparisons. Once the fundamental electrical performance of the model was established, the examination of PRS load kinetic energy transfer commenced with a finer resolution scan of mass to determine the optimum kinetic energy mass loading for the inductance and impedance parameters fixed by the SDM line design.

Several studies were carried out to understand the interaction of a POS with a given PRS load. Operating near the optimum kinetic energy transfer, one may construct any of several POS parameter scans to determine the sensitivity of the final PRS kinetic energy (T_f) to POS behavior. There are three particular variations of interest:

- (i) Since density changes the conduction time, fix the POS sheath gap (D_{POS}) and vary the initial POS density (n_{oc}) to vary T_f (n_{oc}).
- (ii) Since the equilibrium sheath gap size (D_{POS}) at the start of opening partially determines the gap impedance increase, fix the conduction time (through n_{oc}) and vary the gap to determine T_f (D_{POS}).
- (iii) Examine the sensitivity of the energy delivery to the late time impedance of the POS model.

As discussed above the restrike tendency (item iii.), as measured by the open phase energy dissipation in the switch (E_{POS}), may be larger for larger kinetic energy delivery. So one means of investigation is to examine progressively lower mass cases, until the motional impedance on the rundown can be made large enough to cause some POS dissipation.

The second SDM study reveals a clear tendency for the PRS to perform better for larger POS gaps at the start of the opening phase. The initial gap is always pushed to the largest allowed value in the typical POS/PRS calculation, so the variation of the initial gap size might be expected to vary only the initial energy transfer to the load. It turns out however that the DM1 front end parameters are such that a large value for D_{POS} tends to produce a large amplitude "sloshing" of energy into and back out of the PRS front end. So much so that the PRS actually begins a clear implosion, slows

down as the current leaves it, then surges on as the next crest returns from reflection near the POS. In a well optimized rundown there are as many as three of these sloshing episodes. Lowering D_{POS} toward the 0.5 mm range inferred from Hawk opening phase behavior, one finds that the energy sloshing is reduced in amplitude and slightly lengthened in period. The peak energy delivered to the PRS front end, and the peak kinetic energy of the PRS, and the peak load current decay modestly in the process. The behavior is shown in Fig. 9. Notice that the peak load current in these transients can exceed the POS conduction phase peak current.

Completing the program of study just laid out, the first of the SDM studies cited above (load kinetic energy with POS density) reveals a clear tendency for the PRS to perform better for early "firing angles", as determined by the initial POS density. As the conduction phase is made shorter and the POS made to open at smaller current level, the kinetic energy to the load rises by about 20 percent, as shown in Fig.10. These studies only varied the POS density and that density cannot be taken to zero. The strict direct drive case thus required a slight code modification and it was added in the full line simulation, allowing a true direct drive series to be done as reported below.

•The PRS in a Full DECADE Environment

Combining 16 DM1 modules in parallel to form the full DECADE machine model is a simple matter of dividing the line impedances by N_{module} , the number of such units used. In addition, the front end inductance is divided by N_{module} while keeping the same time delay, in order to transform to the parallel impedance. The current feeding the POS model is also divided by N_{module} to preserve the conduction time and peak current in each POS module. On the POS output side, the voltage across the shunts is preserved by maintaining the same relative voltage decay factor that occurs for a single module POS model in equivalent electrical circumstances. Elsewhere in the circuit, the transfer capacitor (TC) is transformed to maintain the same quarter cycle time, and each line shunt or attenuator is also adjusted to the parallel equivalent.

The net effect of the transformation is a single line model carrying N_{module} times more current into the array of POS units. When the POS modules open, their parallel impedance determines the energy dissipated and transferred downstream to the PRS load that now experiences the implosion force generated by the combined currents. Similar to the behavior seen in modeling DM1, the POS opening event in DECADE creates quite a bit of ringing in the front end between the POS and the load, and the transient excursions of current about the low frequency component can lead to load currents in the 30 MA range. The high transient peak current is smoothly degraded by the rundown of the PRS however, and typical drive currents just prior to stagnation are in the 12 \rightarrow 18 MA range. There is also some sensitivity to the early resistance value inferred for the PRS slug phase, a factor 10 change in this resistance can lead to a factor of almost 2 in the expected K shell yield for loads close to the $\eta \geq 1$ domain. However, as the kinetic energy rises into the domain sufficient for substantial K-shell yield this sensitivity gets weaker.

The useful comparison of two point designs differing only in front end inductance on the load side of the convolute can be established by examining a similar array of load masses for each design. The POS behaviour is fixed in both cases by calculating from a restart file taken at the end on the conduction phase and simply shifting the downstream load and convolute model components.

For a lower inductance front end the study reveals that it takes (roughly) a 40 % drop in the inductance to achieve a 8 - 10 % increase in the yield, for the higher mass cases. Conversely, any convolute inductance in the proper range can therefore be increased somewhat if, for example, that increase were designed around allowing a longer implosion distance for the PRS -- a modification which could improve the yield by a much larger percentage.

Moreover, the peak kinetic energy transfer is found to occur for a lower mass as the convolute inductance is increased. A higher inductance implies a lower kinetic energy at any fixed mass, while a lower inductance gives a better compression for the pinch and a slightly larger change in load inductance prior to stagnation.

• The PRS in a Direct Drive DECADE Environment

Unlike the above study of PRS and POS performance as the POS density was decreased to change the "firing angle" of the DECADE line, a true direct drive removes the POS completely, viz. there is no conduction phase and no attempt to sharpen the power delivery from the transfer capacitor. This is a very attractive option from the standpoint of operational simplicity, because essentially all the electrical and mechanical measures of PRS performance are improved at higher mass loadings over even the best case scenario based on the removal of front end inductance. At lower mass loadings the comparison swings back to favor the POS configuration slightly, but in no case does the direct drive option exact a major penalty on kinetic energy delivery.

The comparison can be refined further by examining the transfer of kinetic energy in the two options. In Fig. 11 are shown contour plots of the peak kinetic energy (K_{peak}) achieved in the two cases. The POS option offers a more sustained delivery for lower masses, due to its quick opening time, on a wide domain of initial radii; while the direct drive option offers a more regular variation in delivered energy, due to the absence of reflections in the front end between the POS and the convolute. The same reflections were responsible for the surge behavior seen in the SDM studies discussed above. The POS option also offers a modest increase in delivered kinetic energy on the domain [$mR^2 \approx 200$, $R \approx 5$], but this performance variation is undoubtedly contingent on the accuracy of the POS model in terms of opening time and voltage standoff.

When the yield scaling $Y_K(\eta, \mu)$ is examined for these two kinetic energy delivery options, the resulting yields are similar for low Z materials, c.f. Fig.12(a,b), and marginally favorable to the POS driver for higher Z materials, c.f. Fig.12(c,d). Given the similarities in yield performance shown here and the level of uncertainty in POS operation, a DECADE line built to drive Al or Ar would almost certainly be better configured as a direct drive system. If the primary load domain is moved up to Cu or Kr, then there is clearly something to be gained in POS mode. The behavior of the POS driver with respect to restrike, reclosure, voltage holdoff and overall energy

dissipation then becomes the pivotal question. A POS placed too close to the load convolute could lose all the advantage shown in these figures by injecting plasma into the feeds and either slowing or diminishing the energy flow to the PRS.

• Project Guidance

The present studies have demonstrated that DECADE is reasonably sure of reaching the early PRS radiation goals assigned to it, e.g. 200 kJ of Cu K shell. The POS is of at least marginal utility in achieving this end, provided that it does not expend much plasma into the downstream MITL and convolute. Should the "sneezing" POS present such a problem, a simple fix would be to operate in direct drive mode, with only a modest drop in the yield for loads like Cu and a more serious reduction for Kr. A more complete fix would involve a focus on two follow up study areas with a more detailed line model.

The first area would be the investigation of kinetic energy transfer and convolute impedance changes corresponding to modifications in the final PRS feeds. The focus would be to demonstrate that a wider stalk, and the larger initial load radius that would allow, could be tolerated with regard to the added inductance very close to the load. The experience to date suggests that such a wider stalk would be a small perturbation to the overall power flow and a great help in getting better kinetic energy transfer to the pinch. In addition the examination of axial magnetic fields to stabilize the long rundown options would clearly be advisable.

The second area involves the improvement of the POS model to accept a new gap dynamics equation (developed this year, but not tested extensively). The POS may be placed closer to the convolute in order to shorten the risetime into the load, and the new operating domain should be investigated with regard to the possibility that the POS will physically reclose due to the stresses of the larger applied voltages. In addition a more complete MITL loss model could be added to assess the impact of downstream POS material.

The knowledge developed through these additional studies would also help in

much needed studies supporting the Jupiter concept.

References

1. R.E.Terry, NRL Memo Report 6870, p.116
2. R.E.Terry, "PRS and POS Interaction in DECADE, Part III",NRL Memo Report (in preparation).
3. C. Deeney, private communication.
4. R.E.Terry, NRL Memo Report 6722-93-7301, p. 97.

Fig.1 Parallel Decade Model

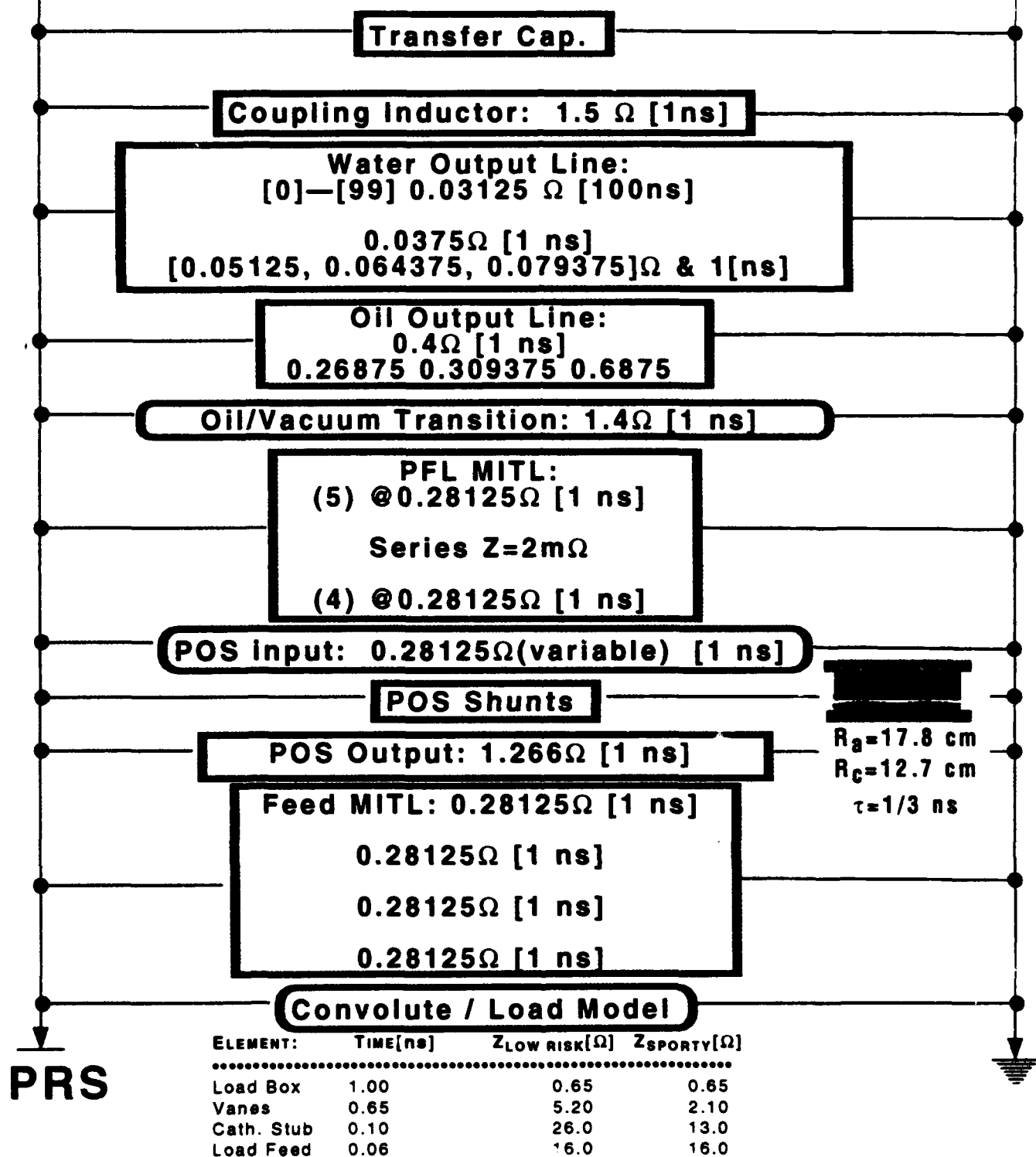
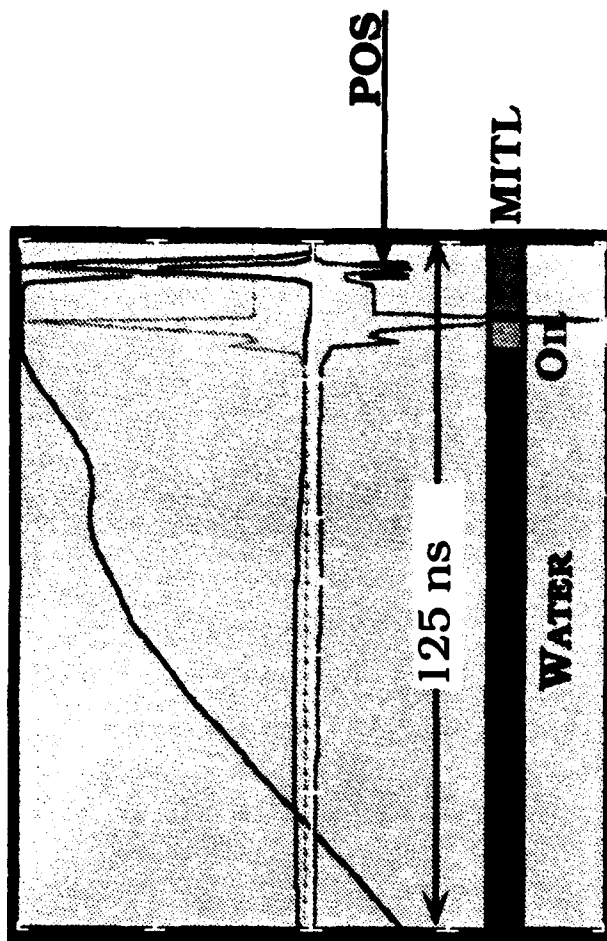
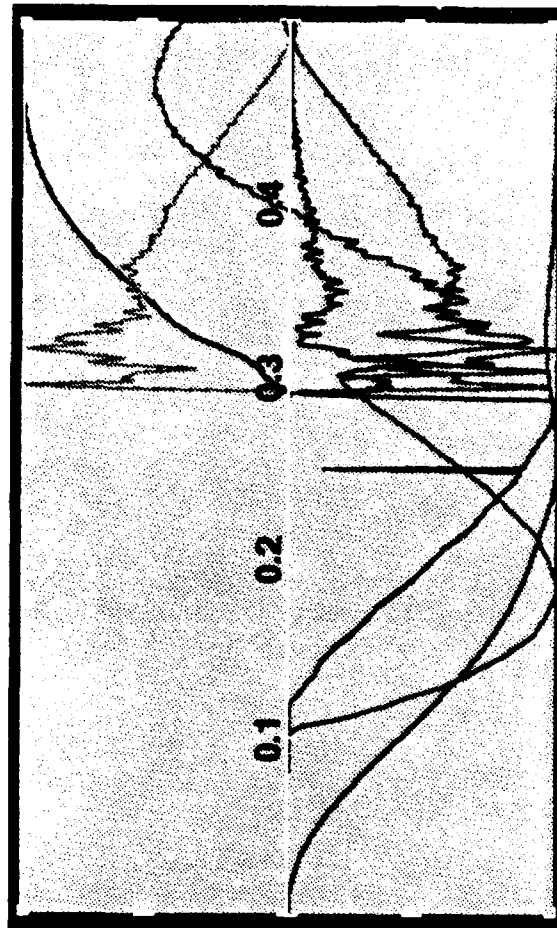


Fig.2 SDM Line Profiles in V,I at 290[ns], just as the POS opens.



+V[kV]	+I [kA]	Z[Ohms]	-E[J/cm]
1.18E04	2.05E03	2.24E01	1.57E03
..[A]..	..[B]..	..[C]..	..[D]..

Fig. 3 SDM Line Waveforms on [0 – 0.500 μ s] with a matched load.



Eload[J]	ElineIn[J]	Vload[kV]	load[kA]	Rload[cm]	I POS[kA]	V stack
9.66E04	2.72E05	3.11E03	6.66E002	2.00E000	2.03E003	1.35E003
..[A]..	..[B]..	..[C]..	..[D]..	..[F]..	..[G]..	

Fig. 4 Line Current in Space and Time

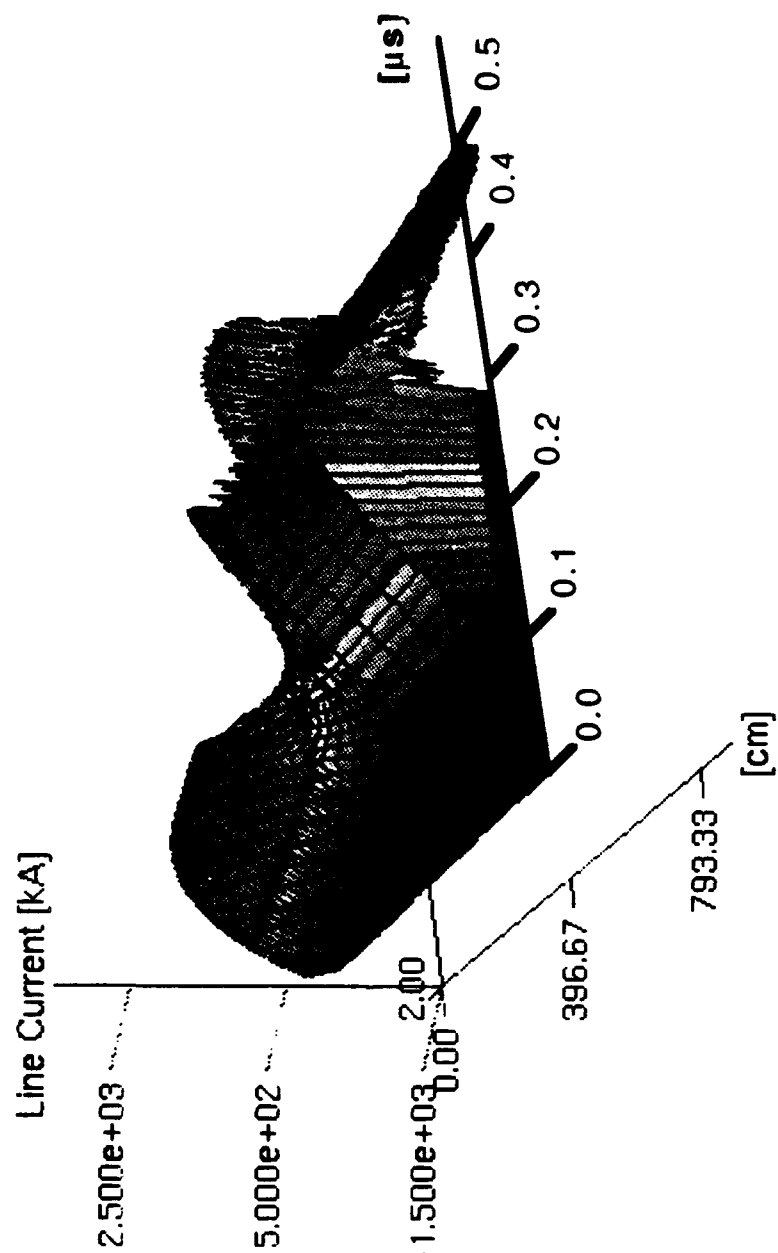


Fig. 5 Line Voltage in Space and Time

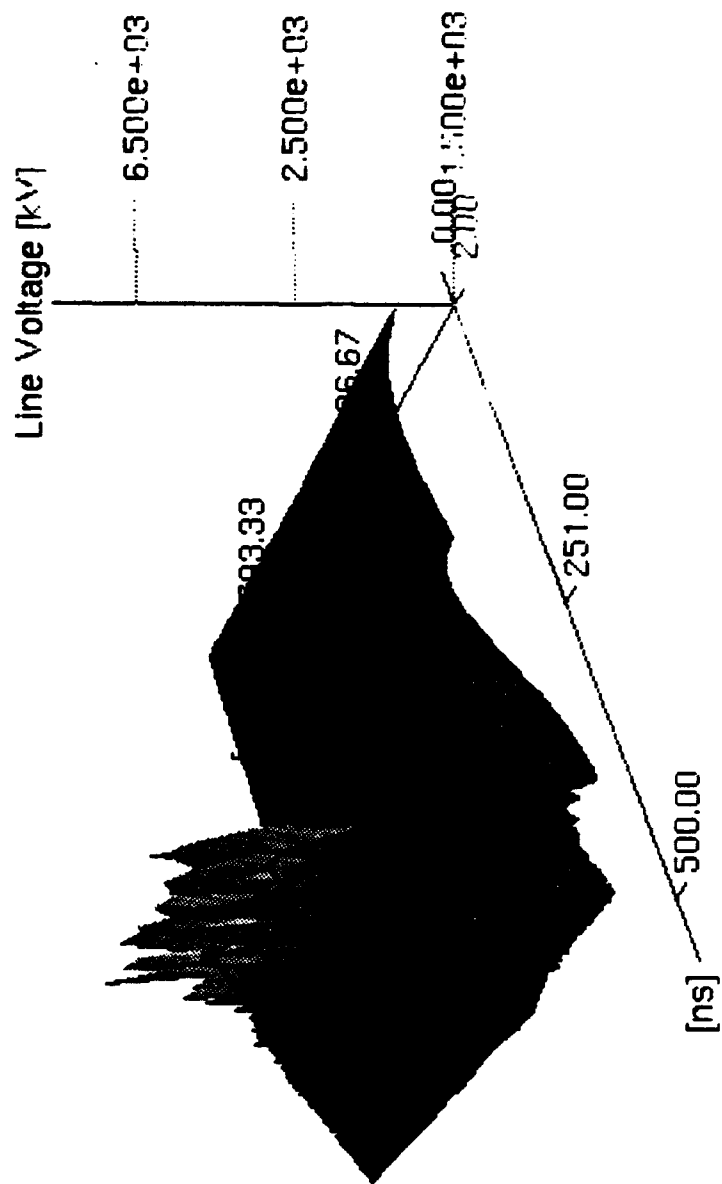


Fig 6 Current Fraction Shunted - Matched Load

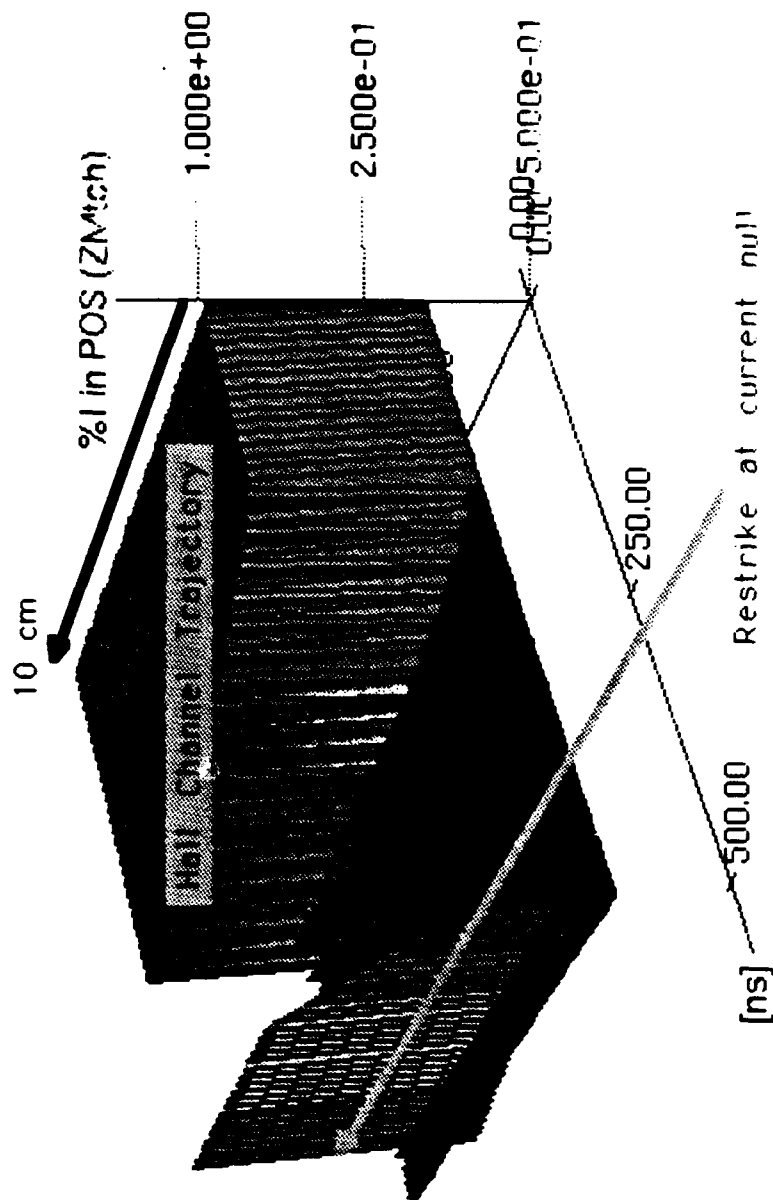
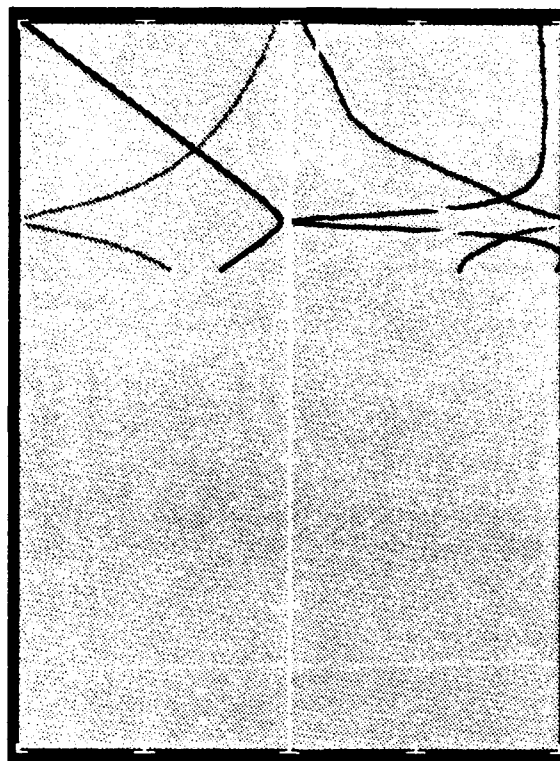
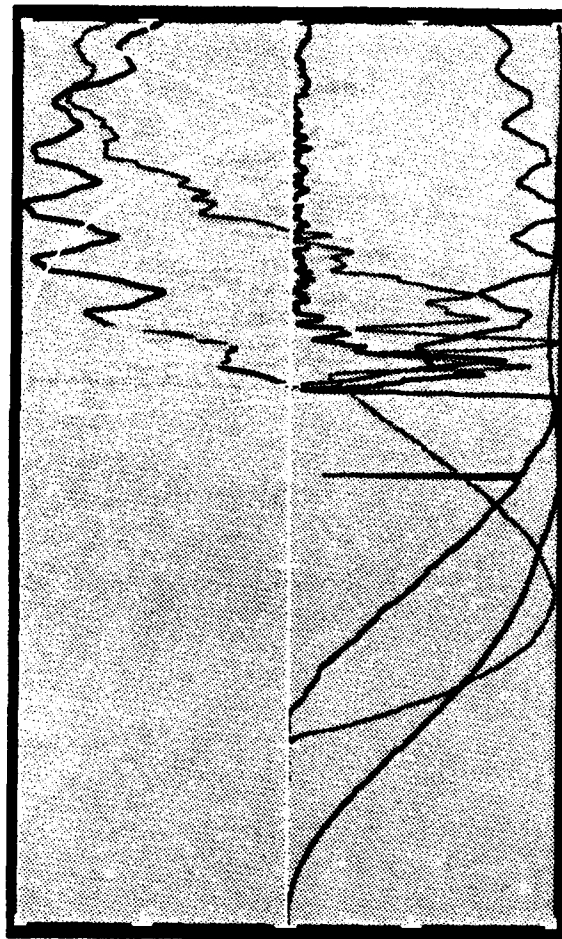


Fig. 7 PRS dynamics on $T=(300,500)[ns]$.



$R[cm]$	$KE[kJ]$	$L[nH]$	$E_{ind}[kJ]$	$Q_{int}[kJ]$
1.90E00	1.30E00	1.36E 01	2.32E00	2.56E00
..[A]..	..[B]..	..[C]..	..[D]..	

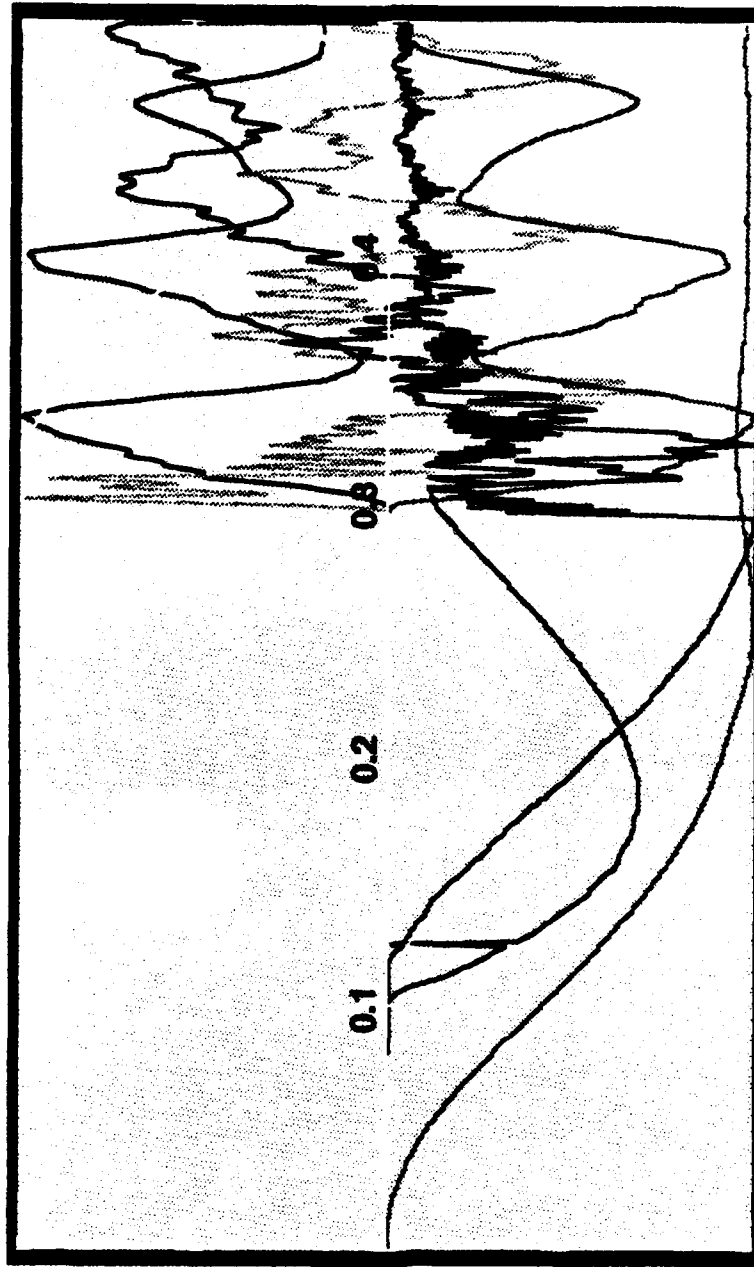
Fig 8 SDM Line Waveforms [0 – 500ns] , for a 10 μ g/cm Ne load



Eload[J]	ElineIn[J]	Vload[kV]	Iload[kA]	Rload[cm]	IPOS[kA]	V stack
2.23E004	2.72E005	4.59E003	7.40E002	2.00E000	2.06E003	1.37E003
..[A]..	..[B]..	..[D]..	..[F]..	..[G]..		

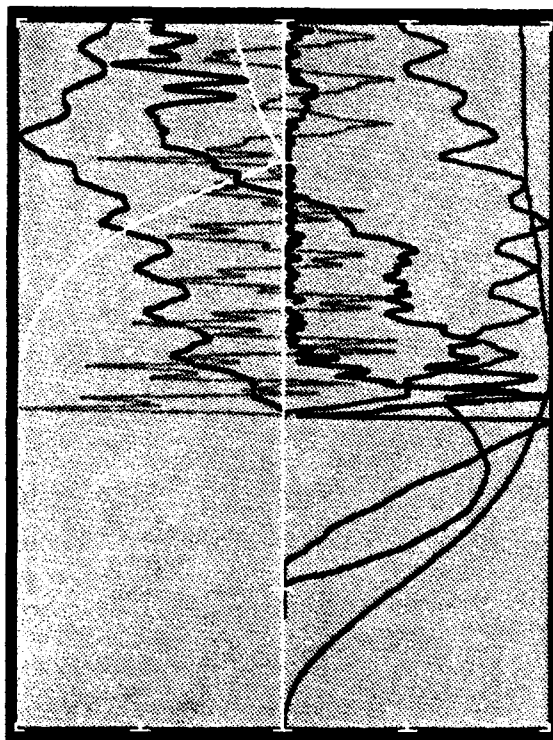
Fig. 9 POS gap size and KE performance

- Large gaps at opening set up surges to the load and result in a better KE transfer.



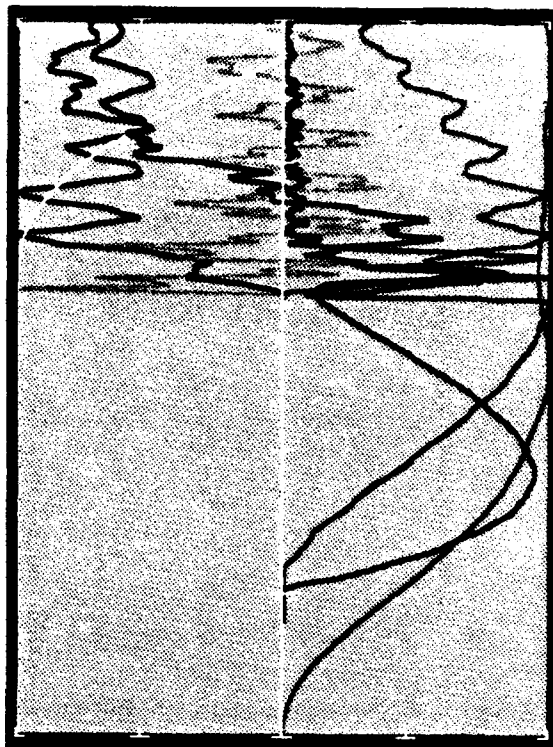
E _{load} [J]	E _{lineIn} [J]	V _{load} [kV]	I _{load} [kA]	R _{load} [cm]	I _{POS} [kA]	V _{stck}
8.53E004	2.71E005	6.24E003	2.40E003	2.00E000	1.95E003	2.00E003
..[A]..	..[B]..	..[C]..	..[D]..	..[F]..	..[A]..	..[A]..

Low [0.00005-10¹²] POS Density Waveforms.



Eload[J]	Eline[J]	Vload[kV]	Iload[kA]	Rload[cm]	IPOS[kA]	V stick
7.67E004	2.72E005	3.01E003	1.72E003	2.00E000	1.40E003	1.77E003
-(A)-	-(B)-	-(C)-	-(D)-	-(E)-	-(F)-	-(A)-

High [8.25-10¹²] POS Density Waveforms.



Eload[J]	Eline[J]	Vload[kV]	Iload[kA]	Rload[cm]	IPOS[kA]	V stick
5.30E004	2.73E005	4.70E003	1.90E003	2.00E000	2.10E003	1.43E003
-(A)-	-(B)-	-(C)-	-(D)-	-(E)-	-(F)-	-(A)-

Fig. 10 Low POS density allows more energy to the load

Fig. 11

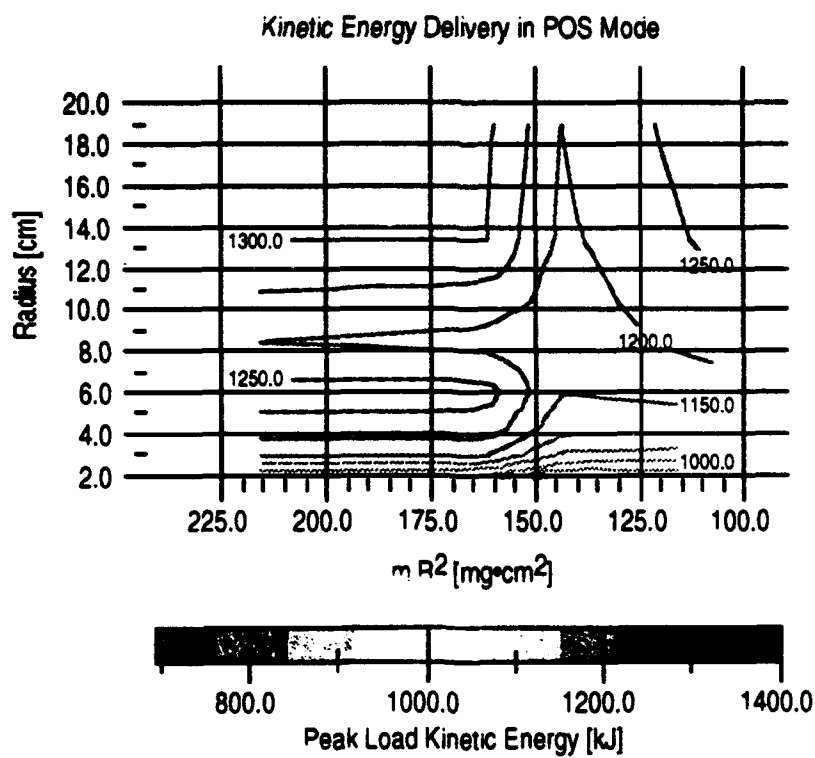
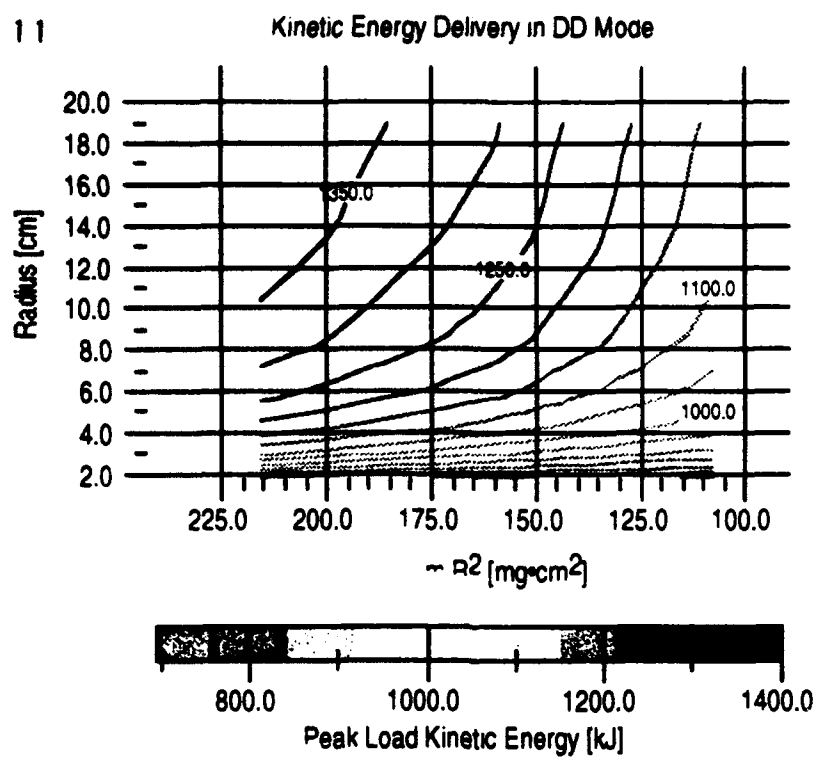


Fig. 12 Yields from Direct Drive and POS modes in Decade

(a) Aluminum Loads

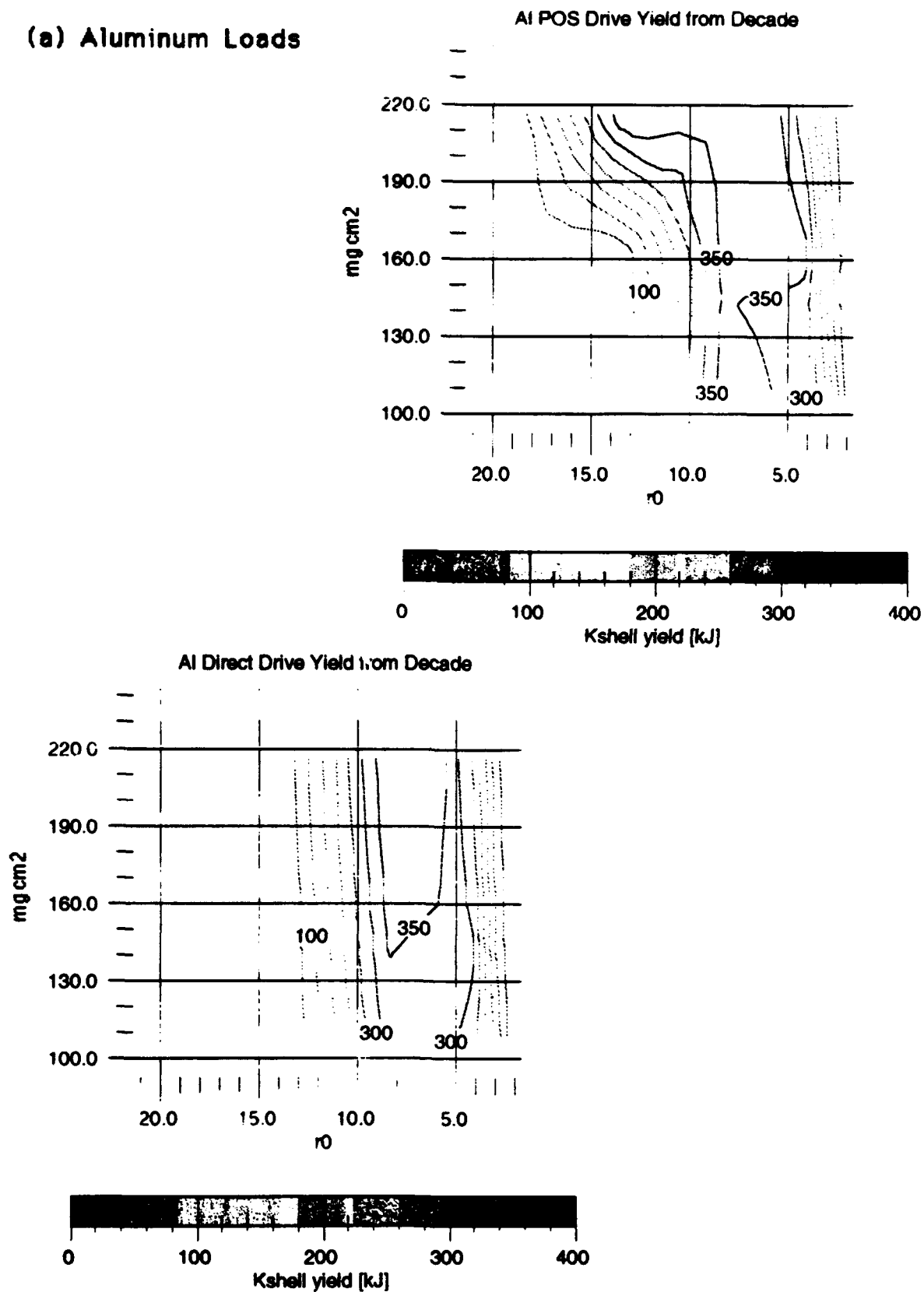


Fig. 12 Yields from Direct Drive and POS modes in Decade

(b) Argon Loads

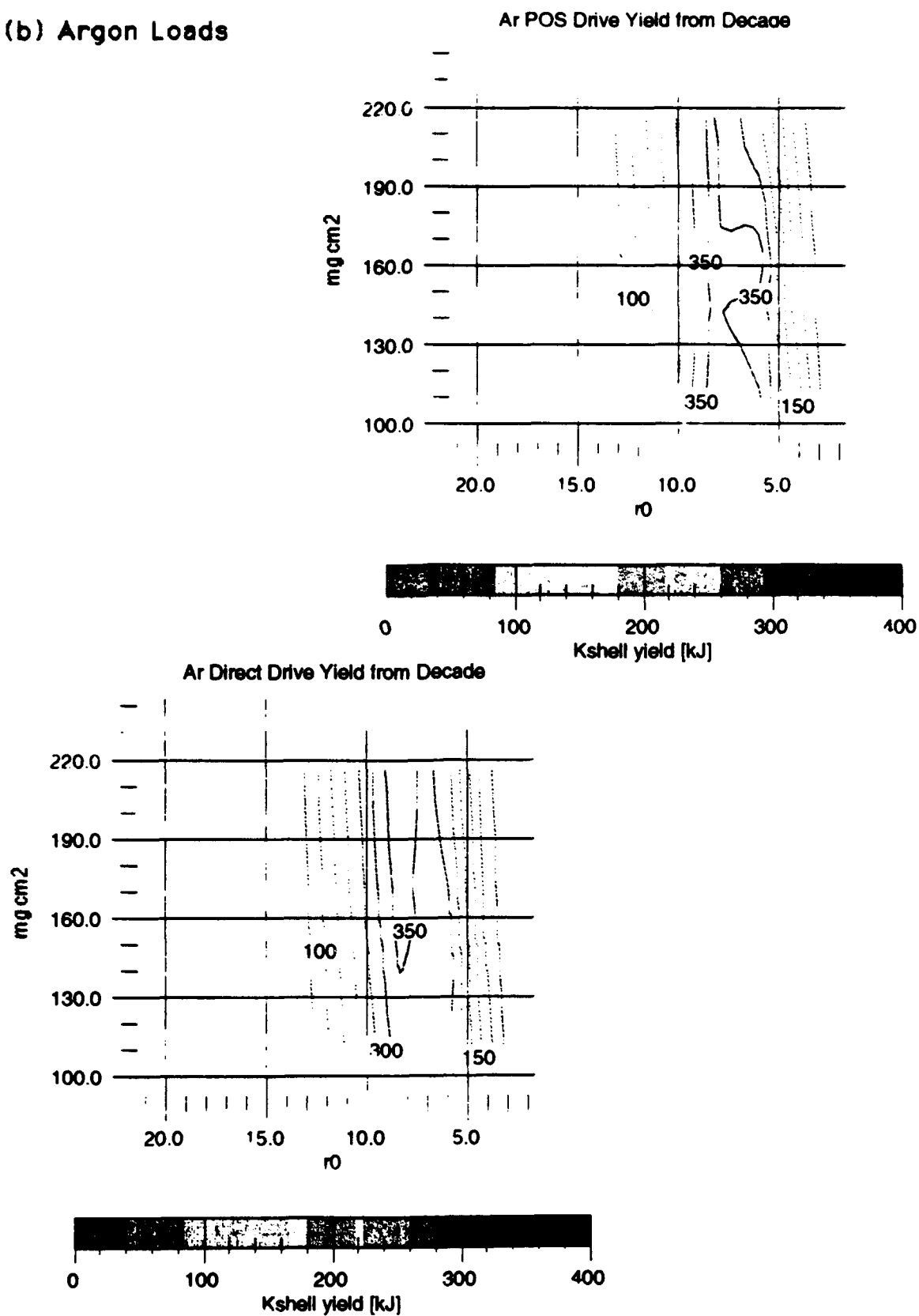


Fig. 12 Yields from Direct Drive and POS modes in Decade

(c) Copper Loads

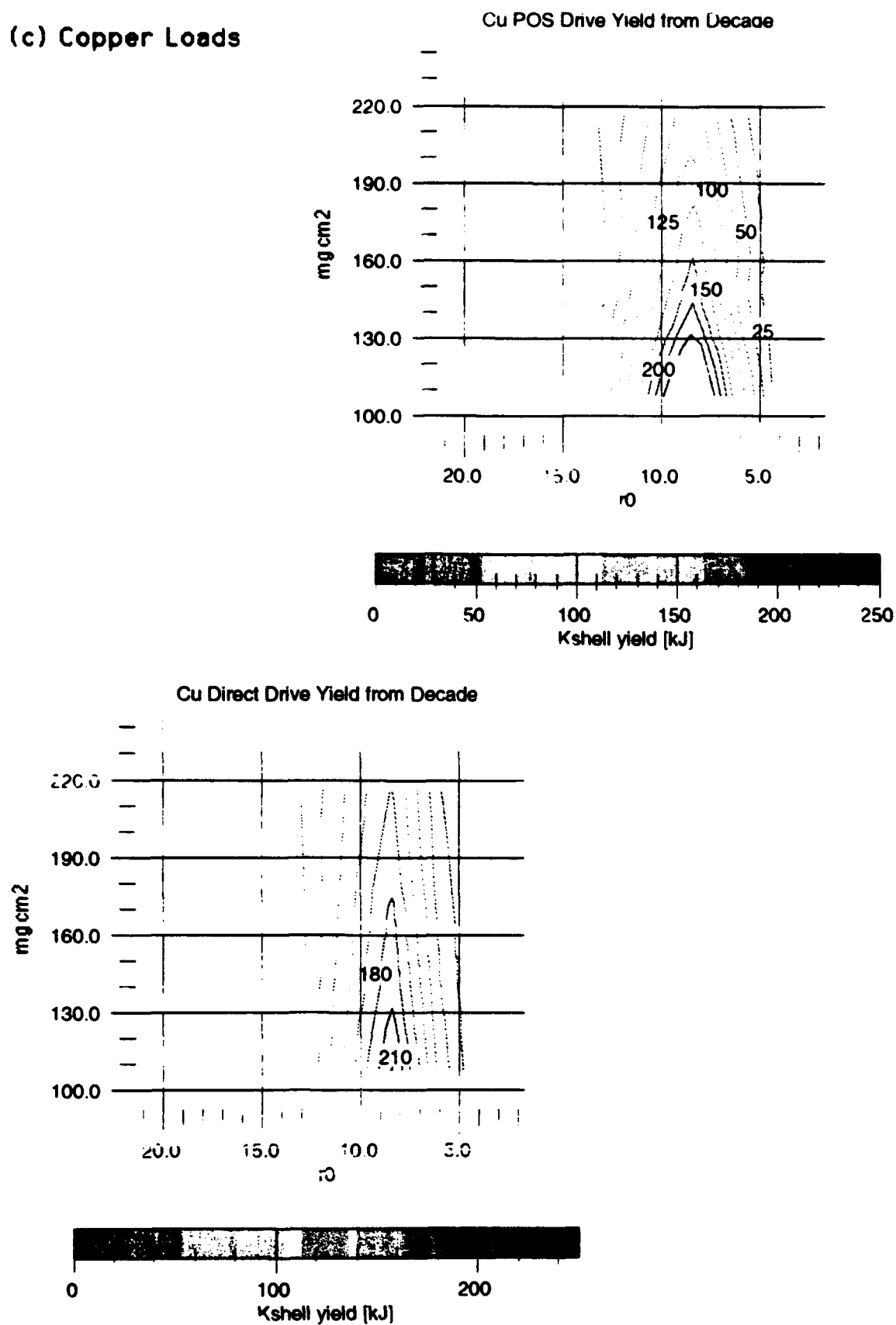
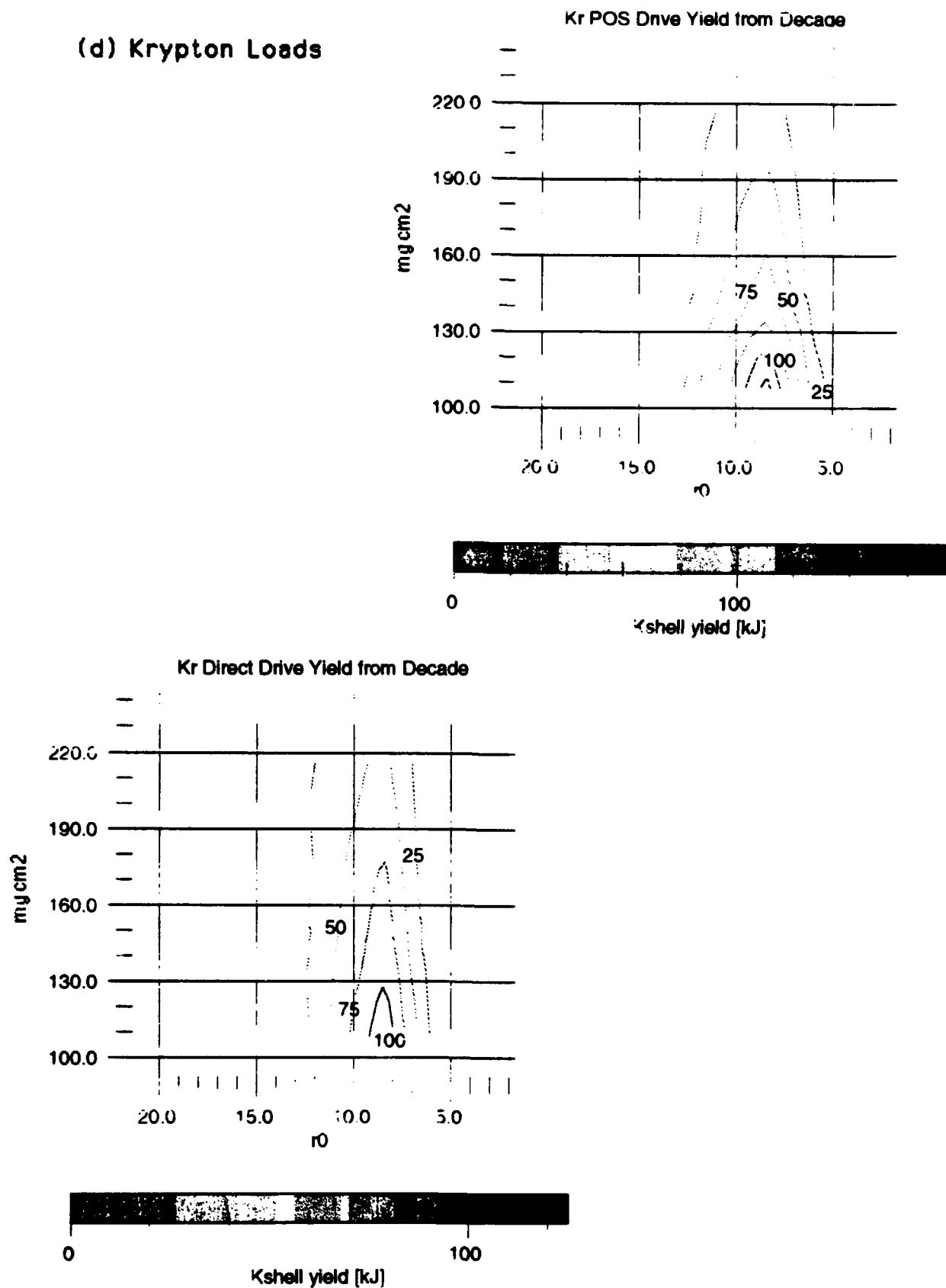


Fig. 12 Yields from Direct Drive and POS modes in Decade

(d) Krypton Loads



V. ANALYSIS OF MHD DATA

Predictions of DECADE performance and the design of better loads to improve performance depend on the ability to successfully match theoretical models with experimental data. Besides predicting gross yields and implosion times and their relation to shot parameters, theoretical models should accurately follow the load dynamics during the pinch. More detailed comparisons between machine performance and model predictions would make it easier to identify where theoretical models should be extended or where load characteristics should be modified. This will increase reliability and lead to more accurate theoretical models.

Even in the absence of detailed experimental measurements, the complexity of numerical modeling makes it essential to develop the highest quality analytical tools. Analysis of MHD data is very similar to that of experimental data: Both numerical models and experimental instruments produce raw data that has little direct or obvious physical significance. The meaning in terms of physical quantities and underlying processes must be deduced by analyzing this raw data and making inferences. The challenge in analyzing experimental data is to deduce plasma conditions from measurements like spectra and fields, while the challenge in analyzing MHD data is to infer experimental measurements from numerically determined plasma conditions.

A recent series of experiments by G. Davara, M.E. Foord, Y. Maron and collaborators at the Weizmann Institute of Science¹ has utilized both radially and axially resolved measurements of spectra and the process of ionization to obtain information about heating, compression and transport within the pinch. Such spatially resolved measurements (especially the radial profiles) have rarely if ever been obtained before for a z-pinch implosion, and provide useful information about pinch dynamics. The quantities measured are easily computed using numerical models, and comparison of such measurements with model predictions could be an important check on the models.

Our PRS model includes full 1-D MHD mass transport as well as detailed ionization and radiation dynamics, and is thus highly nonlinear. Small deviations of pinch parameters from model predictions could result in large discrepancies between predicted and actual implosion times or radiative yields, both because the dynamics are nonlinear and because new processes come into play. For example, viscosity is dependent on plasma conditions, the electron distribution and the presence or absence of turbulence; different viscosities will result in different implosion times, different temperatures and degrees of compression, and so, in a nonlinear way, in different yields and spectra of radiation. The radiative component of this is particularly important, because the pinch radiates strongly, particularly at stagnation, and because the radiative output depends sensitively on the degree of ionization attained in the plasma, which in turn depends on the peak plasma conditions. Radiation is also affected by the electron distribution function in the interior, and this has been shown to be critically dependent on the conductivity and degree of magnetization, which in turn depend on the mobility of the electrons. Electron runaways could also result from

rapid radial current penetration, decoupling the load from the generator and inducing hydrodynamic instabilities farther along the axis. We have previously shown² that runaway electron production is sensitively dependent on the electric/magnetic field ratio.

In this report, we will first briefly describe the results of the Weizmann Institute experiment and then show the analogous results obtained from a detailed 1D MHD-based radiative-hydrodynamic model³ of an implosion with parameters appropriate for DECADE. The presentation is not meant to be a direct comparison between the two sets of data. This would not be appropriate, because of the great difference in implosion parameters in the two cases. Rather, it is meant to demonstrate the capability of our numerical model to computationally obtain the same kind of data as the experiment. These data could serve as a point of comparison between model and experiment, if similar measurements could be made on high-power machines as were made on the Weizmann apparatus. The data are also useful in themselves, because they give insight into the complex ionization dynamics described by the model. Thus, the analysis is part of a continuing program to assure self-consistency and to obtain maximum physical insight from the model results. This kind of analysis will be extended in the future to provide a more intuitive understanding of implosion dynamics in DECADE, Saturn and other machines.

Experimental results

The Weizmann Institute experiments utilize a low power, carbon dioxide gas puff z-pinch. The load is injected with initial radius $R \approx 2$ cm and annular extent $\delta r \approx 5$ mm. The peak load current $I_{max} \approx 250$ kA, with $V_{max} \approx 30$ kV potential difference, and the current rise time is about $1.1 \mu\text{sec}$. The implosion timescale is about 600 ns.

The experimenters used a 1.3 m spectrograph (resolution 0.04 Å) coupled to a high-resolution streak camera (100 ps temporal resolution), with sensitivity between 2000 Å and 8000 Å. The spatial resolution was 0.5 mm horizontally and 2.0 mm vertically. Relevant to the present report, they measured the radial position and velocity of oxygen charge states in the load (O II through O VI). The time-evolution of the charge-state position showed the speed of ionization, while the Doppler broadening in the spectrum showed the velocity of the ions.

The experimenters found that each charge state behaved individually. The ionization front, defined by the appearance of O II, advanced much more rapidly than any Doppler shift-derived species velocity, and reached a maximum of $10 \text{ cm}/\mu\text{sec}$ just before stagnation. Initially neutral, the gas progressively ionized at the outer edge, which was the hottest point (18 eV at 80 ns before stagnation). Species velocity was much faster for ions at higher degrees of ionization; the O II maximum velocity was about $4 \text{ cm}/\mu\text{sec}$, while O VI reached a maximum of $10 \text{ cm}/\mu\text{sec}$ just before stagnation.

The features that will concern us here are an ionization wave propagating faster than the local

fluid velocity, and the faster kinetic velocity of higher charged states (probably related to the localization of ionization at the outer edge). Ionization was surmised by the Weizmann Institute group to be driven by electron heat conduction, and the ion fluid velocity derived primarily from ion-ion collisions rather than a pressure gradient. Our model results for a high-power aluminum implosion behave similarly to the Weizmann Institute CO₂ implosion, although the story is more complicated. The ionization front velocity exceeds the fluid velocity, and the higher charge states have greater velocity than lower charge states, but in the model results not all ionization occurs at the outer edge.

Model results

Here, we will show calculations of radially-resolved ionization state populations and plasma conditions from a numerical (1D MHD) model of a high-power implosion of aluminum. These numerical results are the same quantities reported from the experiments, "measured" to arbitrary precision with the theoretical model.

The 1D MHD model used³ has been used extensively to model implosions from a variety of PRS devices. Besides MHD particle dynamics, it includes full radiation and ionization hydrodynamics; for these calculations, 55 atomic states were included in the model, including all 14 possible ionized states of aluminum and many of their possible excited states. A lumped circuit model was used, in this case with Saturn-based circuit parameters. The model utilizes enhanced transport, so that transport coefficients have been phenomenologically adjusted to match observed implosion parameters: electrical resistivity is set to 20 times, thermal resistivity is set to 30 times, and viscosity is set to 80 times the Spitzer value.

The load was an aluminum plasma with mass mass loading of 330 $\mu\text{g}/\text{cm}$, length 2 cm, and radius between 1.18 and 1.23 cm ($\delta r = 0.5$ mm). Initially, the temperature is about 10 eV, the ion density is $1.8 \times 10^{19} \text{ cm}^{-3}$, and the plasma consists only of Al V and Al VI.

A plot of the load current and voltage during the modelled implosion is shown in Fig. (1). The time $t = 0$ is defined to be when the voltage is initially applied. The current reaches a maximum of 8.8 MA at 69 ns, and was arbitrarily cut off at the point of maximum compression. The maximum voltage across the load is 4.6 MV, at 50 ns. The average ion density and temperature during the pinch are shown in Fig. (2). These reach a peak nearly together at about 81 ns, which is also the time of peak compression (stagnation). At this time, the pinch outer radius is 0.28 cm. At stagnation, the local electron density reaches 1.1×10^{21} , the electron temperature at the inner edge is near 10 keV, and the plasma consists mostly of completely stripped aluminum.

The progress of the implosion can be seen graphically in Fig. (3). Here an RGB palette is used, where black is zero, red is the minimum finite value and blue is the maximum value. The plots in this figure are analogous to streak photographs, with the ordinate corresponding to time and the

abscissa to radial position (the center line is at the origin). In all plots, the overall compression of the plasma to a minimum at 80 ns is evident. The temperature plots show the ohmic heating of the plasma initially at the outer edge and later compressional heating at the center. The density plot shows that the pinch initially expands somewhat and cools and then, during run-in, experiences strong compression at the outer edge. The degree of ionization plot shows the extremely rapid propagation of the ionization wave soon after compression begins. The electric and magnetic field plots show the current penetration during run-in and stagnation.

For computational purposes, the load is divided into 30 concentric annular zones, each of which moves with the local fluid velocity, each constrained by the motion of the others. Because of this, the local fluid velocity is always known and can be used as a benchmark. If the ionization wave propagates towards inner zones (as it does), its velocity exceeds the local fluid velocity. The outer radius of the outer zone is taken to be the pinch outer radius, and is close to what a pinhole photograph would measure as the pinch radius, although the luminosity of each zone has not been included. The motion of the zone boundaries during the implosion is shown in Fig. (4). Where the boundaries come closer, the local density is larger.

The color plots in Fig. (5) show the process of ionization in the load. Here again, the ordinate is the time axis, with a full extent of 100 ns lasting until just slightly after stagnation. The abscissa corresponds to the radial zone number, and is divided into 30 strips, one for each zone. The pinch center line is at the origin, and higher zone numbers are closer to the outer edge. Using zone instead of radial position for the abscissa has two advantages. First, it expands the display, making variation clearer, particularly near stagnation when the plasma is compressed. Second, it shows explicitly that the ionization front is moving in excess of the fluid velocity (that is, the cell velocity), and by how much. An RGB palette is used here, and the appearance (and disappearance) of each charge state is marked by the appearance of color against the black background. Colors represent the magnitude of the population fraction of the given charge state, and all population fractions for the different charge states sum to one at any given time and any given radial position. Blue means a low population fraction, and red means the plasma at that position and time is almost entirely composed of the given charge state. Plots are aligned horizontally so that the plasma composition at a given time can be easily identified, at least for ionized states displayed in the same column.

It can be seen in Fig. (5) that the plasma is initially composed of Al V and Al VI. After about 30 ns, the ionization wave commences, so that Al VII appears at 30 ns, Al VII at 35 ns, Al IX at 40 ns, Al X at 41 ns, and Al XI at 42 ns, all initially at the outer edge. Before about 40 ns, there is very little compression, and in fact the plasma slightly expands until this time. After 40 ns, the current ramps, and the implosion begins (this coincides with the peak in the load voltage). The increase in temperature and pressure during run-in rapidly (within 5 ns) lead to the development of the Al XI and Al XII species at the outer edge, and these species dominate until stagnation sets

in, near 60 ns. The Weizmann Institute observations were made during this run-in period in their experiment.

As stagnation occurs, a secondary ionization wave propagates from the outer edge to the center, and Al XII further ionizes to Al XIII; after about one ns, another ionization front forms, moving from the center out to the edge. This last process of ionization occurs during the maximum compression, as the implosion kinetic energy thermalizes, and it produces fully stripped ions. Although there is some cooling on the outside after stagnation, the plasma is mostly fully stripped for the remainder of the run (to 100 ns).

Quantitative details of the ionization dynamics can be seen in the population profiles in Fig. (6). As seen in the figure, population fractions at 21 ns are essentially as in the initial state. At 30 ns, the outer edge has heated sufficiently to produce significant populations of Al VI and Al VII. At 40 ns, outer-edge ionization continues, with charge states to Al X and Al XI forming there. Also evident at this time, however, is interior pre-ionization, so that near 1 cm there is more Al VI than Al V. This is a consequence of nonuniform compression during run-in, which causes a slight pre-heat of the pinch interior and may decrease the efficiency of thermalization at stagnation. The main effect, however, is the outer-edge ionization, which continues to be evident at 62 ns with the formation there of Al XII.

The average radial velocity of the ions in each charge state as a function of time during the run-in is shown in Fig. (7). This is what would be determined by measuring Doppler broadening of ionized-state spectra, as was done in the experiment. As was experimentally found, the higher charge states have a higher velocity. This is not unexpected, since the each successive charge state initially appears near the outer edge, and the outer edge has the highest radial velocity during run-in (this can be inferred from the zone boundary trajectories in Fig. (4)). The difference in velocity between different charge states was proportionately much greater in the experiment than in the model results, however. The absolute run-in velocities in the high-power model implosion are 5 to 10 times greater than the experimental values (up to 60 cm/ μ sec).

The location of the maximum population of each charge state is shown in Fig. (8) as a function of time during run-in. This is where the charge state is most likely to be located in an experimental measurement (As Fig. (5) shows, the charge states are pretty well localized during run-in). The trajectory of the charge state maxima traces out the progression of the ionization front for each stage of ionization. The closer in space and time the maxima for different charge states are, the faster the ionization process. The model results agree with the experimental observations, that the ionization front velocity exceeds the fluid velocity, and that higher ionization stages appear first at the outer edge of the pinch. In the experiment, however, the radial separation between different charge states was much greater; the model shows a much faster ionization, more like a shock. Besides the greater power and faster pinch in the model implosion, a possible explanation for this

is the greater number of ionized states available in aluminum compared to oxygen.

Conclusion

We have here demonstrated the application of several new perspectives for analyzing the results of numerical models of PRS implosions. This analysis was prompted by the recent demonstration at the Weizmann Institute of new diagnostic measurements in z-pinch implosions, and the results we have obtained are in the same pattern as those experimental results.

From the MHD data analysis, we find that, as in the experiment, there is an ionization wave that propagates faster than the fluid velocity, much faster during run-in, but probably not so fast as to be a shock front. We also find that the higher charge state ions have a greater velocity. The difference in velocity between different types of ions, however, is much smaller in the MHD results than in the experiment. In addition, the MHD analysis showed nonuniformities within the pinch that caused some internal preheat and pre-ionization, probably due to compression. These nonuniformities could have been present in the experiment as well, but not observed, because of the small number of data points available experimentally.

If similar radially and axially resolved measurements were obtained from high-power PRS loads such as DECADE and Saturn, the procedures we have followed here would allow a closer examination of the correspondence between the actual observations and the theoretical model of the experiment. This would improve the theoretical models and provide better understanding of the experiment. Even without direct comparison to experiment, however, this analysis is useful.

MHD data analysis such as that demonstrated here provides direct physical insight into the actual working of the model, and shows among other things where and for what parameters internal heating is occurring, what the important heating and conduction processes are, and where the important ionized states first appear. Data from the model also indicate whether conditions are suitable for other processes to be important, such as runaways and turbulence. This process of identifying the important processes and conditions is just as important in a complicated numerical model such as is needed for advanced PRS design as it is in an experimental procedure. The implications of this analysis of MHD data have only been hinted at in this presentation, because the analysis is still in its initial stages, but this process will be further developed in the future.

References

1. M.E. Foord, Y. Maron, G. Davara, L. Gregorian and A. Fisher, "Particle velocity distributions and ionization processes in a gas-puff z-pinch", Weizmann Institute of Science preprint (1993).
2. Radiation Hydrodynamics Branch, "Advanced Concepts Theory Annual Report 1990", NRL Memorandum Report 6870 (1991), p. 86ff.
3. J.W. Thornhill, K.G. Whitney and J. Davis, *J. Quant. Spectrosc. Radiat. Transfer* **44**,251 (1990).

Figure captions

1. Current through the load (solid line) and voltage across the load (dotted line) as a function of time. The time $t = 0$ is defined to be when the voltage is first applied. The current was arbitrarily cut off when the pinch reached maximum compression.
2. Average ion density (solid line) and ion temperature (dotted line) as a function of time. The average is given by summing the quantity for all particles and then dividing by the total number of particles.
3. Color display of various state variables during the implosion, as a function of time (ordinate) and radial position (abscissa). The center line is at the origin, and radial profiles at a given time are along a vertical line intersecting the appropriate time value on the ordinate. Black indicates zero, and a "rainbow" color palette is used, with blue, yellow and red respectively indicating minimum, intermediate and maximum values.
4. Position as a function of time of the outer boundaries of each of the 30 concentric annular zones in the computational grid. The outer and inner zone boundaries are solid lines, and the other boundaries are dotted lines. Greater compression is indicated when the boundaries move closer.
5. Color display of the evolution of the population fraction profiles of each ionized state as a function of time. The ordinate is the time (in ns), and the abscissa is the zone number, corresponding to radial position (see Fig. (4)), with the center line at the origin. Population fractions range from zero to one, and the sum of the fractions of all charge states is one at every position and time where there is plasma. Black indicates the absence of the charge state, and a color if present indicates the relative abundance of the charge state, with abundance increasing from blue to yellow to red. A profile of the plasma composition at any given time can be seen along a vertical line that intersects the ordinate at that time value. Displays are horizontally aligned to permit comparison of simultaneous populations (at least if the charge states are in the same column). Because the abscissa is zone number and not actual radius, these profiles show no compression during the implosion, although from other figures it is clear that the zones do get significantly closer during run-in.
6. Population fractions for important charge states as a function of radius, at times of 21, 30, 41 and 62 ns. Charge state fractions not shown are not significantly present. The population fraction is plotted as a dashed line with the charge state identification printed near its highest point. For example, at 21 ns, the plasma is mostly Al V (peak fraction 0.9 near the edge), with some Al VI and Al IV. Population fractions at each point sum to one.

7. Radial velocities (in cm/ μ sec) of ions in different charge states, as a function of time during run-in. Here, symbols for highest charge states are joined by lines. These are: "+" for Al XIV, "*" for Al XIII, "." for Al XII, diamond for Al XI, triangle for Al X, square for Al IX, "X" for Al VIII, and "-" for Al VII. In addition, the "+" symbol not joined by lines represents Al VI.

8. Radial position (in cm) of the peak population of several charge states as a function of time, during run-in. The solid line represents Al XIV, which is not significantly present during this time. Other charge states are represented by the following symbols: Al XIII ("+"), Al XII ("*"), Al XI ("."), Al X (diamond), Al IX (triangle), Al VIII (square), and Al VII ("X"). Higher charge states appear first on the outer edge of the pinch, and generally remain farther out from the center line during run-in. Some mixing of peak positions, evident at 50 ns and 70 ns, could be the result of nonuniformities in the implosion.

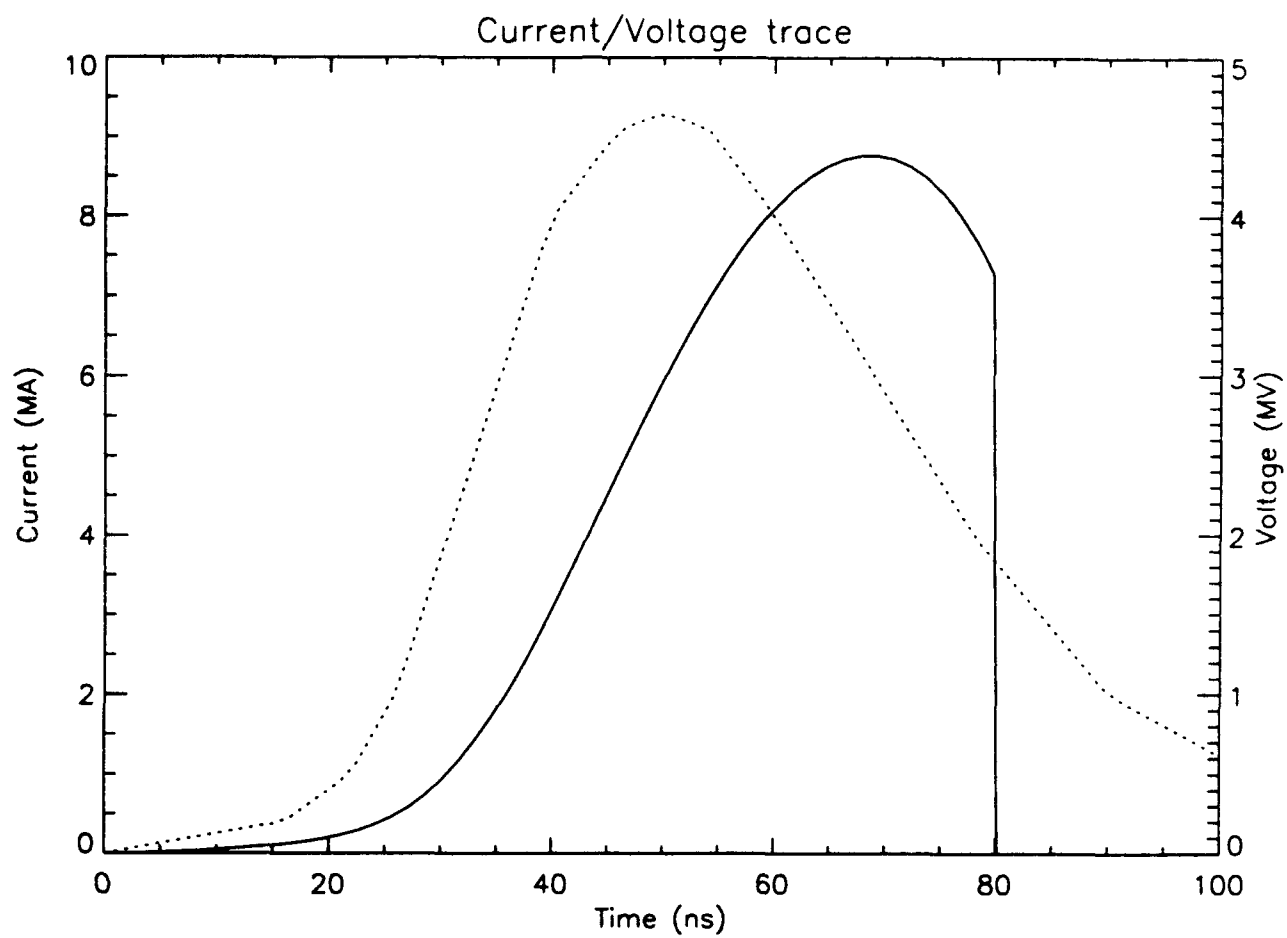


Fig. 1

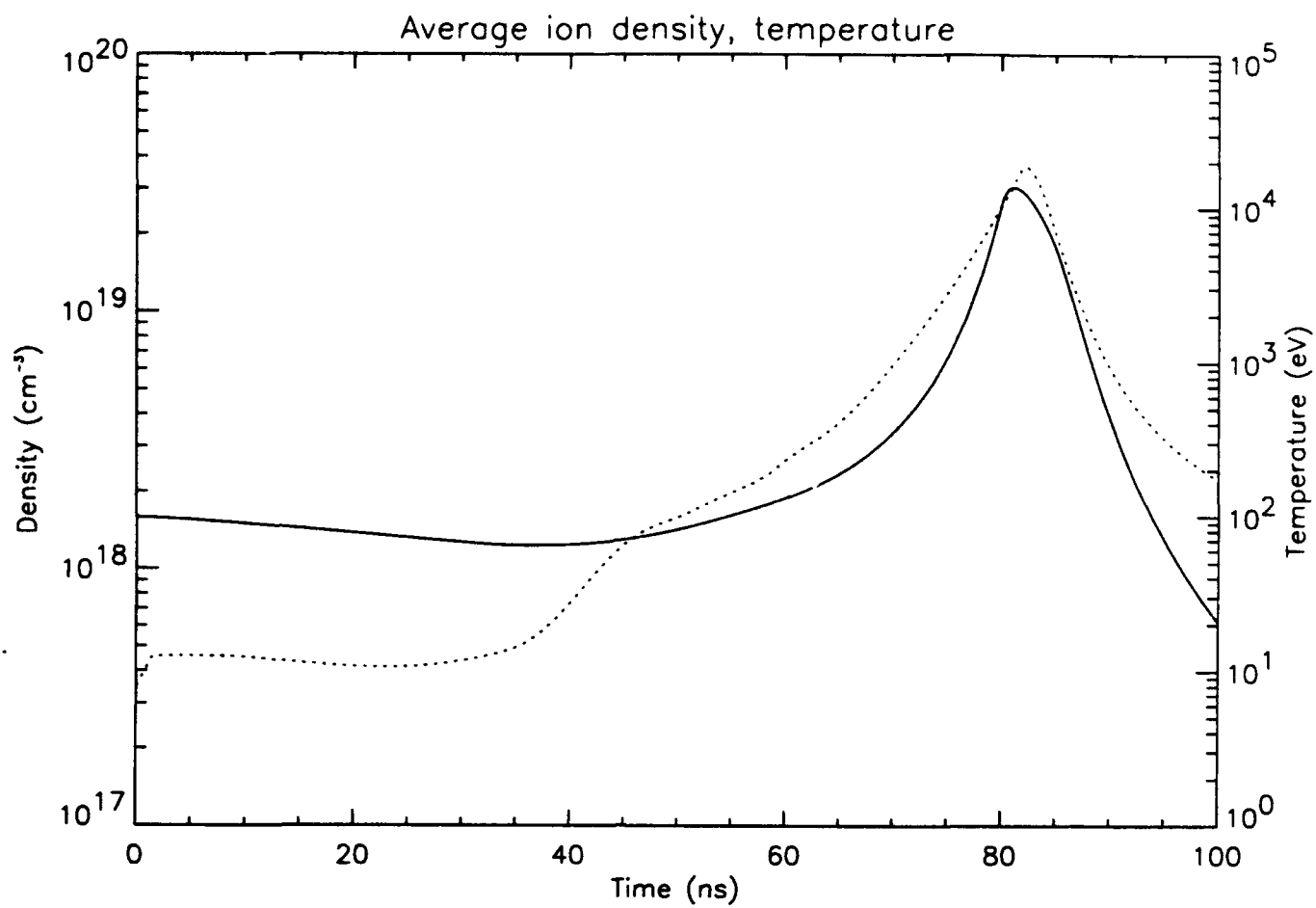


Fig. 2

STATE VARIABLES

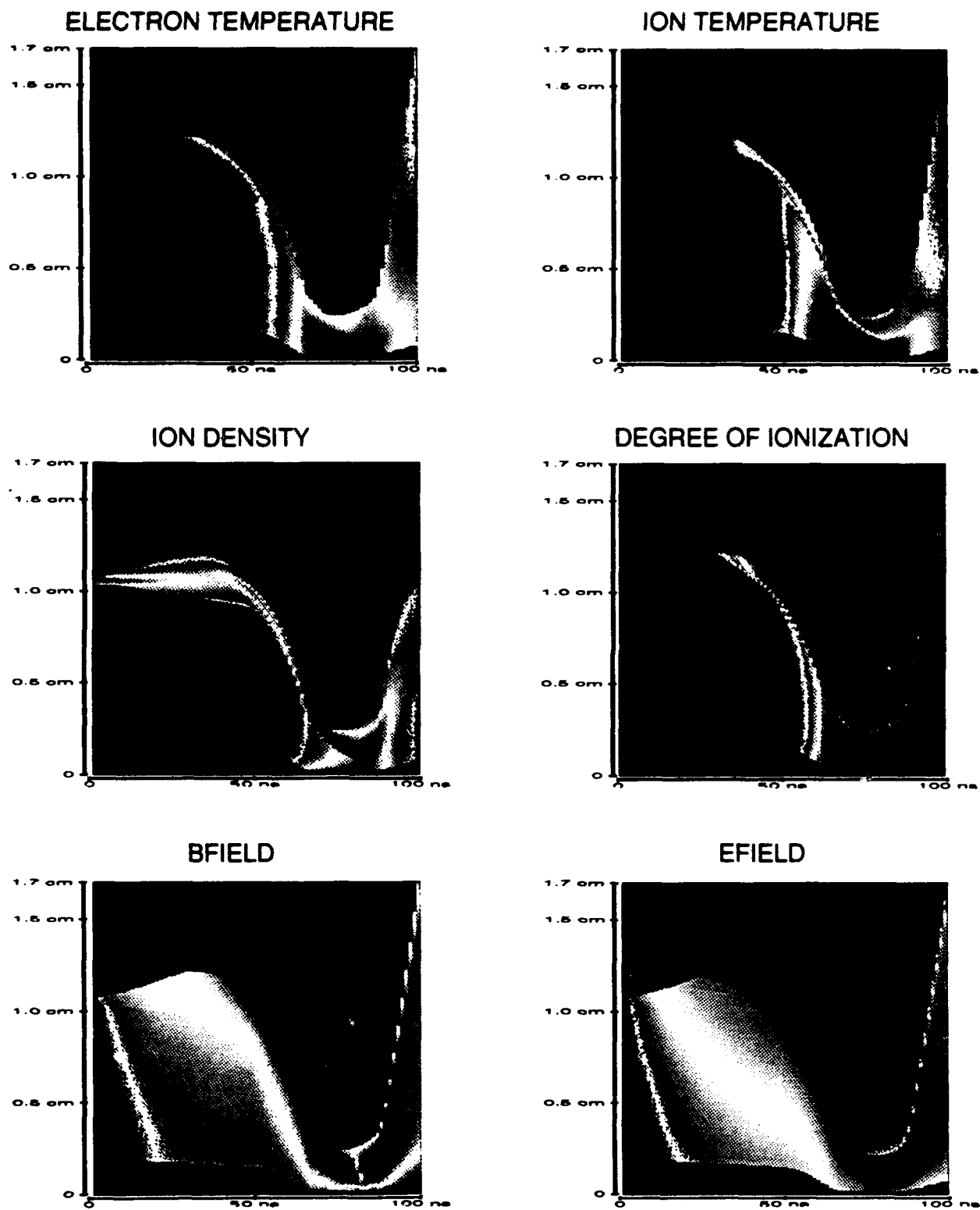


Fig. 3

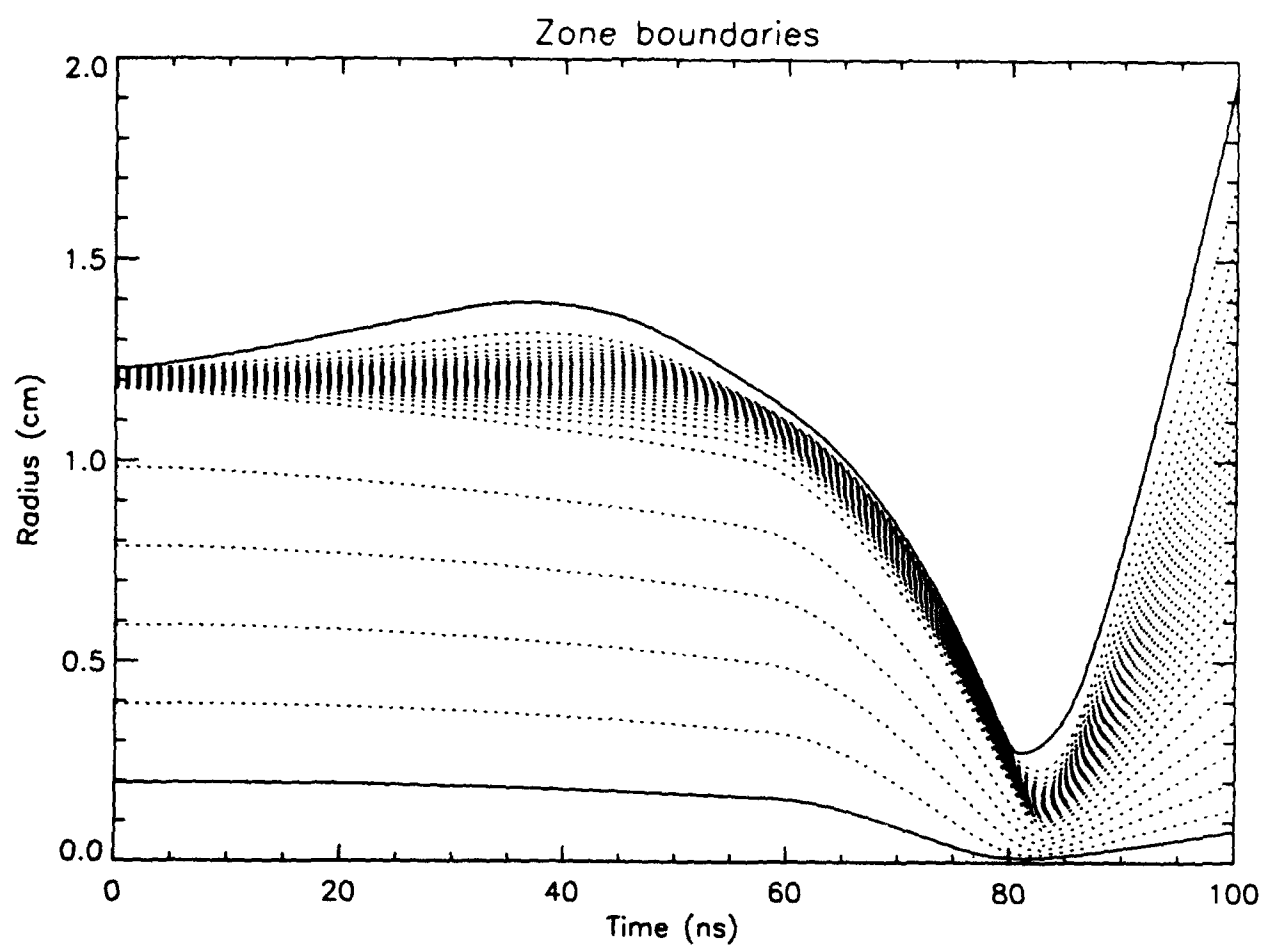


Fig. 4

Ionized-state population profiles vs. time

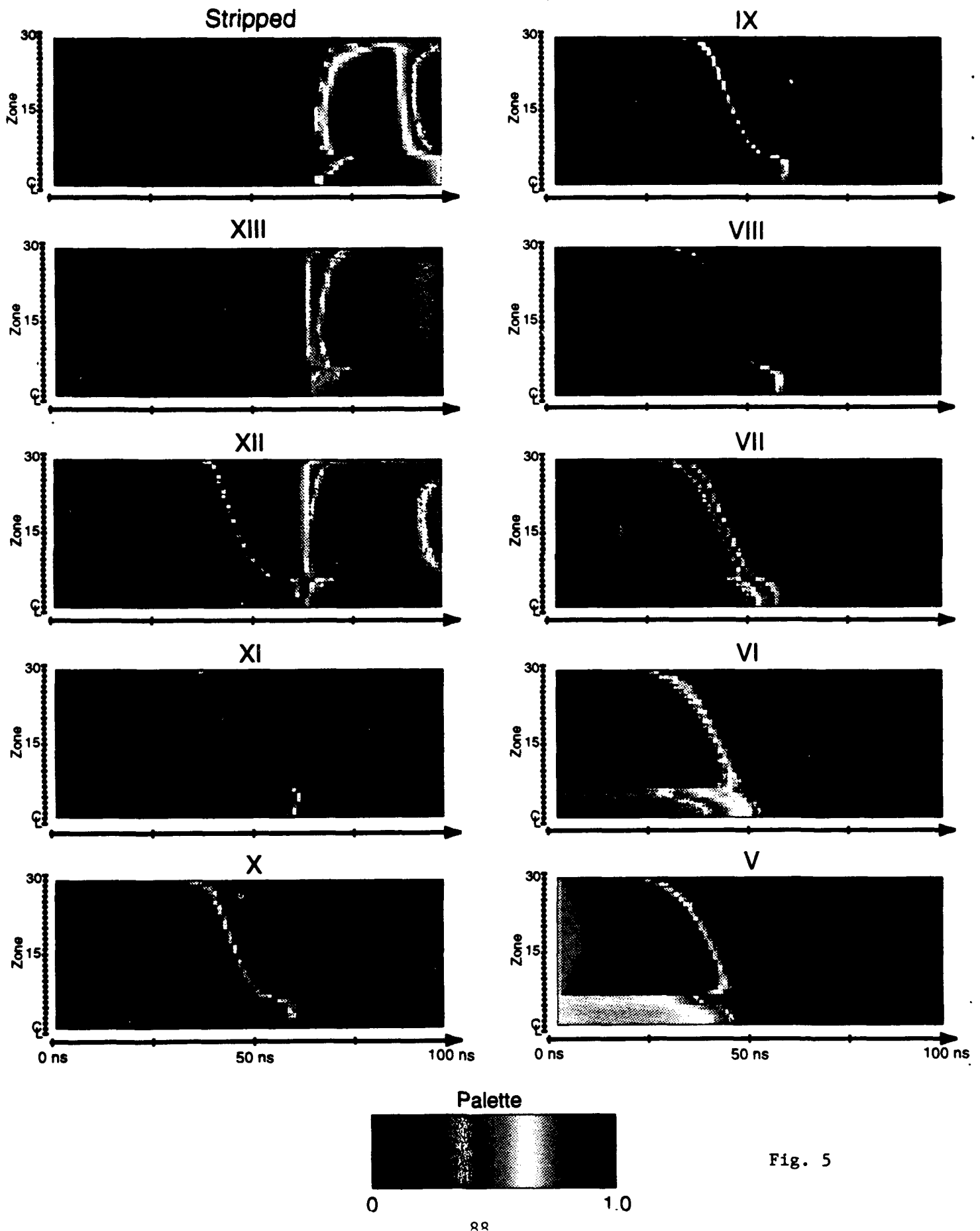


Fig. 5

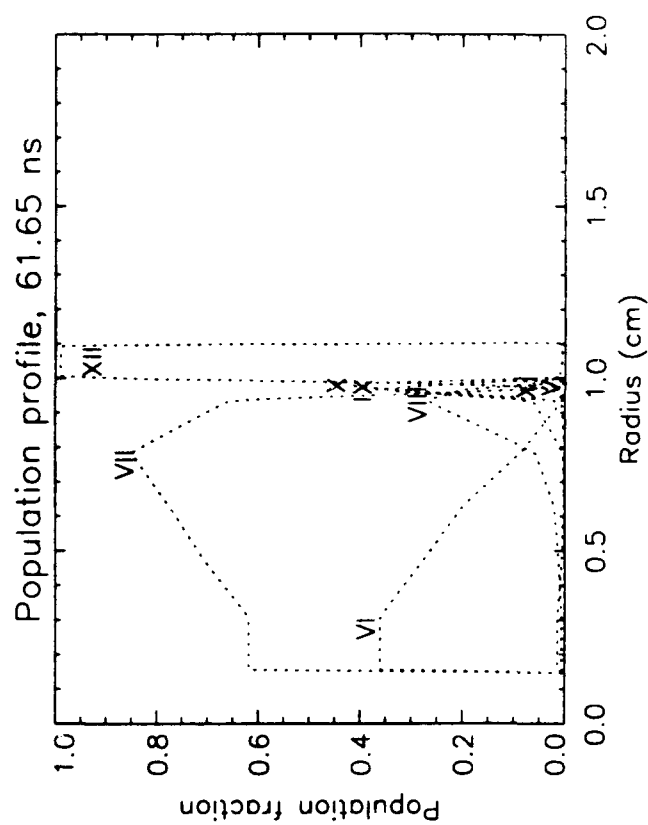
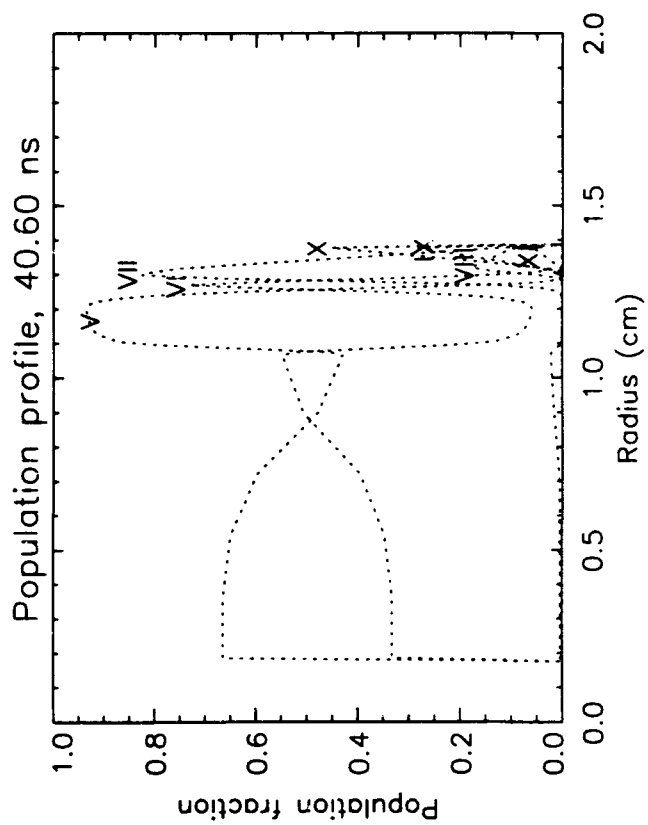
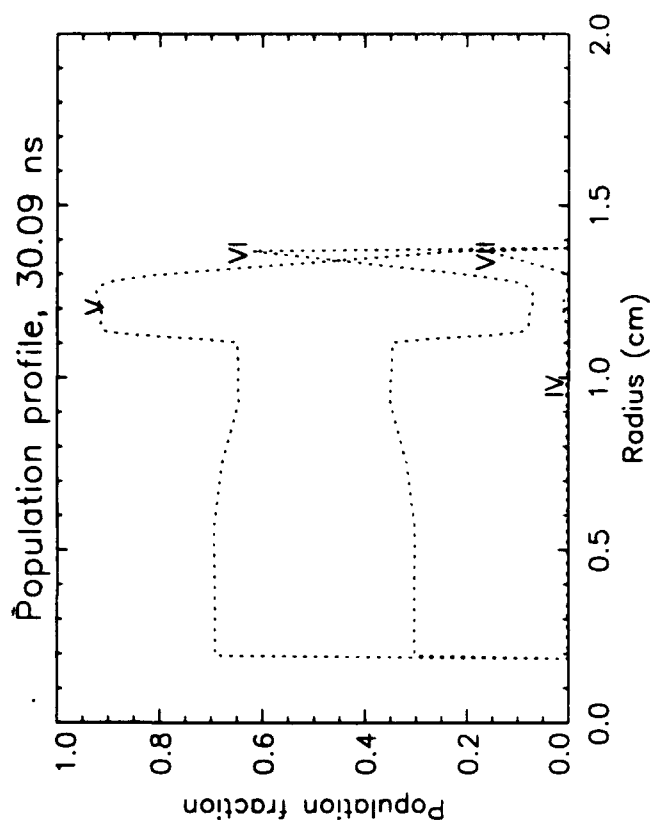
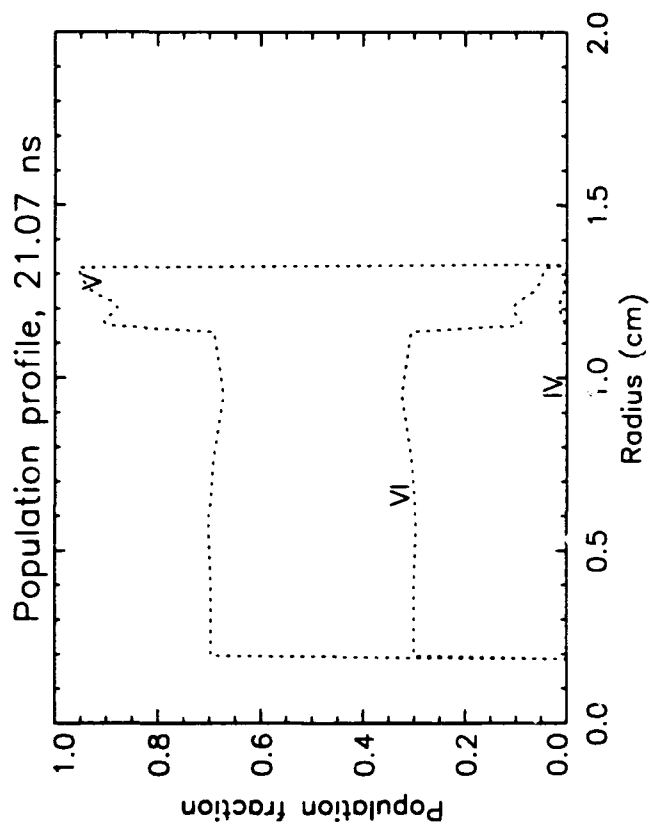


Fig. 6

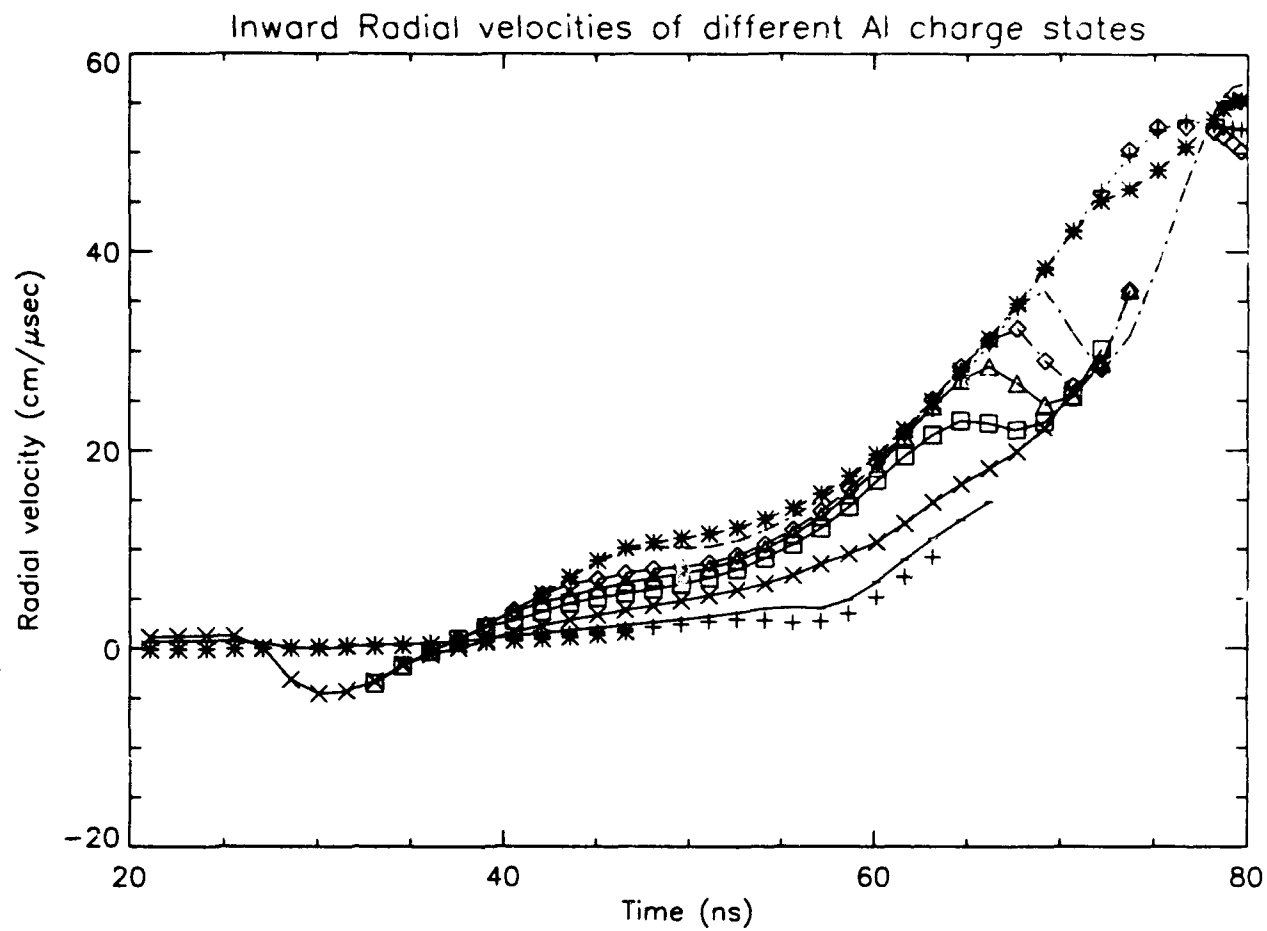


Fig. 7

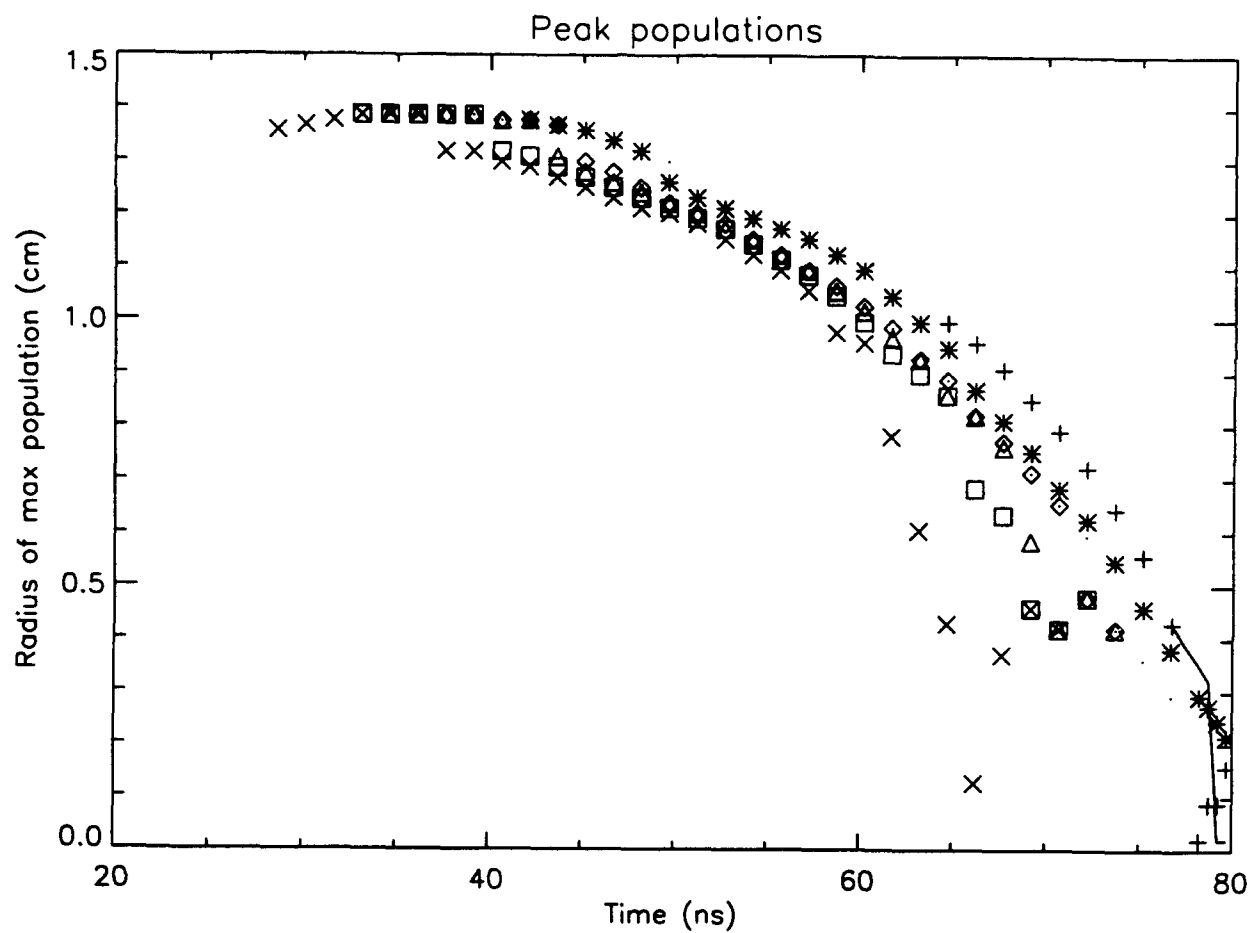


Fig. 8

VI. L-SHELL MODEL DEVELOPMENT

The development of X-ray diagnostics for ions in the L-shell, using line emissions from such ions, is of fundamental importance for the understanding of plasma conditions. Using the line ratio intensities for two emission lines arising from different excited states of a given ion one can determine the temperature in LTE. Temperature diagnostics can also be obtained by comparisons of intensities of lines from neighboring ionization stages of an element. The purpose of this work is to develop a detailed description of the $n=3$ multiplet levels of F-like ionization stage of selenium. We have already developed a very accurate and detailed data base for the $n=3$ multiplet levels of Ne-like selenium. Similar to using the H to He line ratios to obtain the K_{α} diagnostics, the F to Ne line ratios can be used to determine the L-shell X-ray diagnostics. Previous theoretical predictions and experimental observations indicate substantial F-like population for selenium plasma and the experimental observation of strong 3-2 L-shell spectra for this ion provides the motivation for a thorough theoretical investigation of the F-like selenium ionization stage. A detailed description of the multiplet levels for an ion such as F-like selenium requires an enormous amount of atomic data. In order to accurately determine the populations of the atomic states of an ion in the steady state for a given plasma density and temperature, and to make comparisons between observed spectra and theoretical calculations one needs to obtain accurately calculated atomic rates populating and depopulating these states. Theoretical modeling of the extreme UV spectrum for F-like selenium in the experiments at the Lawrence Livermore National Laboratory is at discrepancy with the experimental observations. Also, theoretical calculations using plasma hydrodynamics simulations predict strong 3-3 lines for F-like ions, however, no such lines were observed in the experiments. These facts necessitate further detailed and accurate modeling of the kinetics of F-like ionization stage. The rates of the various atomic processes populating the states depend on the rate coefficients which are obtained by calculating the atomic cross sections and averaging them over the electron distributions for the appropriate plasma temperatures. The cross sections that are needed for the atomic processes include collisional excitation, deexcitation, ionization, photoionization, as well as radiative and dielectronic recombination. Under coronal equilibrium conditions, one needs to

take into account recombination processes as well as radiative cascade from upper levels to obtain various level populations by solving a multitude of different rate equations. The level of the detailed calculations of the cross sections of these processes as well as the determination of the energy levels of the atomic states involved depend on the atomic model required to accurately represent the kinetic properties of the plasma. For example, in the ionization balance calculations it may be sufficient to calculate configuration averaged atomic data whereas detailed calculations at the fine structure levels are required in predicting spectra.

We have developed the $n=3$ multiplet levels of F-like ionization stage of selenium in a similar fashion as was done for Ne-like selenium. Our compact model contains the three $n=2$ low lying states and fifty seven $n=3$ multiplet states including 8 $2p^4 3s$, 21 $2p^4 3p$, 28 $2p^4 3d$, three inner-shell excited configurations of $2p^5 3s$, $2p^5 3p$, $2p^5 3d$ and the two lumped $n=4$ excited state levels. Figure 1 shows this basic model.

The atomic structure and cross sections for this work were calculated using various computer programs such as the computer codes developed at Los Alamos National Laboratory, the atomic code of R. D. Cowan¹ and the relativistic distorted wave codes developed by Sampson and Zhang.² The energy levels, oscillator strengths and plane wave Born (PWB) collision strengths were calculated using CATS,³ a version of the atomic structure code of Cowan, modified by the group at Los Alamos. Even though our basic atomic model contains the inner-shell excited states at the configuration level, the multiconfigurational structure calculation includes the fine structure levels of these states with a total of 113 states for all L- and M-shell ground and excited states of F-like selenium. Our energy levels compare very well with the fully relativistic energies calculated by Hagelstein.⁴ We have neglected any configuration (CI) among higher levels and doubly excited levels. In order to check the effect of CI on the energy levels, Hagelstein included 1622 states which included 3/3' doubly excited levels and found no significant effect. In Table I we show the designations and the energies of the levels that are included in our model.

We have also calculated the wavelengths and absorption oscillator strengths for some of the strong $n=2-3$ transitions. Except for a few transitions our absorption oscillator strengths agree

very well with those of Hagelstein. When compared with the experimental data our oscillator strengths are also in good agreement for many of the transitions. Table II shows a comparison of our oscillator strengths with other data.

From our previous experience, during the development of a detailed atomic data base for Ne-like selenium, we realized that the existing Branch codes for calculating the necessary collision strengths and photoionization cross sections for the model were quite inadequate. This made it absolutely necessary to obtain and use other available computer codes such as the CATS code and the distorted wave collision codes developed by Sampson and Zhang and capable of producing much more accurate and consistent atomic data for collision and photoionization. In order to compare the data obtained using the in-house capabilities with these more sophisticated and detailed codes, we calculated a few collision strengths for F-like ions. Since the branch code was developed for K-shell modeling and the data for the L-shell were obtained inconsistently, there were accidental agreement between our collision strengths and those obtained by the other codes for certain electron energies. We thus could not rely on the existing branch codes and needed to use these more developed and reliable codes for determining an accurate level populations for the $n=3$ levels of F-like selenium. The collision strengths for excitation from the low lying $n=2$ to all the excited $n=3$ fine structure levels were calculated in the PWB method using CATS. The results obtained agreed with other published collision strengths except at very low energies. The PWB cross sections for excitation are not sufficiently accurate for spectroscopic purposes and specifically near threshold. We therefore used the ACE⁵ (Another Collisional Excitation) code (also obtained from Los Alamos) which is a modified version of Mann's⁶ distorted wave (DW) method and gives more accurate collision strengths than the PWB method. However, since the DW calculations are much slower than the PWB calculations and we need to generate a large number of collision strengths, only the very important transitions were calculated using ACE. ACE uses the atomic structure data generated by CATS. We have obtained the collision strengths for excitation from the $n=2$ to $n=3$ states as well as for collisional coupling between the $n=3$ excited states. We have obtained the collision strengths for excitation at the fine structure levels. However, these quantities can be obtained directly from

CATS at the configuration averaged or at the multiplet levels as seem necessary. Table III shows the collision strengths for a few of the strong 2-3 transitions in F-like Se obtained using the ACE code in the DW approximation. We also compare our results with those published data of Sampson and Zhang. Our DW collision strengths for the strong collisional excitations are within 10% of those relativistic DW collision strengths obtained by Sampson and Zhang. The DW collision excitation cross sections $\sigma_{if}(E)$ were obtained from the collision strengths Ω_{if} by using the formula

$$\sigma_{if} = \frac{\pi a_0^2}{2J_i + 1} \frac{1}{p^2} \Omega_{if}(E)$$

where i and f refer to initial and final states, a_0 is the Bohr radius, $2J_i + 1$ is the statistical weight of the initial state, E is the incident electron energy and p is the momentum of the incident electron. Our DW collision excitation cross sections compare quite well with those of Hagelstein in some cases, whereas in some other cases the agreement is quite poor. This is shown in Table IV. It was found that the results obtained by Hagelstein for the transitions (1-31) and (2-38) which were at great discrepancy with our cross sections were erroneous.

As already mentioned, we have also calculated the collisional excitations between the $n=3$ excited levels and found that the $2p^4 3d$ levels are strongly coupled to the $2p^4 3p$ levels. Thus inclusions of these excitation rates will have major influence in the calculations of population of the $n=3$ multiplet levels.

The dielectronic recombination rates from the low-lying O-like ground levels to all the singly excited $n=3$ F-like states were calculated in detail by using the HFR (Hartree-Fock with relativistic corrections) method of Cowan. In order to calculate the rates for dielectronic recombination (DR) process, where a free electron is captured by an ion forming a doubly excited state which stabilizes either by radiative decay to the singly excited state of the next ion or by autoionization, one needs to obtain a huge number of autoionization and radiative data. For each doubly excited F-like levels, we thus calculated atomic data which include rates for all possible autoionization channels including autoionization to excited states of the initial ion and radiative data such as oscillator strengths and radiative decay rates for all possible dipole stabilizing transitions from these doubly

as well as singly excited F-like states. Our DR data also necessarily include the energies for these large number of doubly and singly excited states.

The DR branching ratios from the low lying $n=2$ O-like levels to each specific fine structure levels of the singly excited $n=3$ F-like states were calculated explicitly for low lying doubly excited states. For the high rydberg states with $n>10$, the autoionization rates were approximated by using the $1/n^3$ fall off of these rates while the radiative rates remained constants. Our DR branching ratios were calculated for a large number of intermediate resonance states in the single configuration approximation. Approximate relativistic corrections are made to both the radial wave functions as well as to the singly and doubly excited states energies. Figure 2 shows the DR rate coefficients to some of the $n=3$ levels of F-like Se. We have previously calculated the DR branching ratios for several F-like ions including Ar⁸, Ti¹⁴, Fe¹⁸, Se²⁶ and Mo³⁴ ions and obtained scaling relations using the DR data for recombination from Ar⁸, Ti¹⁴, Fe¹⁸ and Se²⁶ ions using three or four coefficients polynomial fits to our data. These results are already in press and will be published in the 'Atomic Data and Nuclear Data Tables'.⁷ The DR data for recombination from O-like Mo was calculated to investigate the validity of extrapolating the Z-scaling beyond Se. Except for a few data points, the Z-scaled data using the data for Ar⁸, Ti¹⁴, Fe¹⁸, and Se²⁶ ion predict the Mo³⁴ data which are within a few percent of the explicitly calculated data. This and the fact that our DR rate coefficients for O-like and F-like ions agree quite well with other detailed and more complex calculations, give us confidence in our use of Cowan's HFR method of calculations of DR rates.

Presently our L-shell data base for F-like selenium does not include any radiative recombination rates. We will in the near future upgrade our calculations by including such rates. We also intend to upgrade our ionization rates for ionization from Ne-like to F-like selenium very soon. We already have the computer codes (one from Penn state by Sampson and Zhang, and the other from Los Alamos) available to compute improved ionization rates. In the case of Ne-like Se, it was seen that the $n=3$ levels of this ion were substantially populated by indirect or resonance excitation (RX). We therefore plan to compute such RX rates and include them to the direct collisional excitation rates for excitation from ground levels to the $n=3$ levels of F-like selenium.

REFERENCES

1. Atomic structure code of R. D. Cowan following his book *The Theory of Atomic Structure and Spectra* (University of California Press, Berkley, CA, 1981).
2. D. H. Sampson, H. L. Zhang, and C. J. Fontes, *Atomic Data and Nuclear Data Tables*, **48**, 25 (1991).
3. J. Abdallah, Jr., R. E. H. Clark, and R. D. Cowan, **Theoretical Atomic Physics Code Development I. CATS: Cowan Atomic Structure Code**, Los Alamos National Laboratory manual (December 1988).
4. P. L. Hagelstein, *Phys Rev. A* **34**, 934 (1986).
5. R. E. H. Clark, J. Abdallah, Jr., G. Csanak, J. B. Mann, and R. D. Cowan, **Theoretical Atomic Physics Code Development I. ACE: Another Collisional Excitation Code**, Los Alamos National Laboratory manual (December 1988).
6. J. B. Mann, *Atomic Data and Nuclear Data Tables*, **29**, 407 (1983).
7. A. Dasgupta and K. G. Whitney, *Atomic Data and Nuclear Data Tables*, **57** (1994).

Table I. State configurations, total angular momenta J and energies relative to the ground state for the lowest 65 states of F-like selenium. Notation a[b] means $ax10^b$.

level	jj-state	J	Energy (eV)	level	jj-state	J	Energy (eV)
1	$[2s^2 2p_{1/2}^2 2p_{3/2}^3]_{3/2}$	3/2	0	33	$[2s^2 2p_{1/2}^2 2p_{3/2}^3]_{3/2} 3d_{3/2}$	1/2	1.616[3]
2	$[2s^2 2p_{1/2}^2 2p_{3/2}^4]_{1/2}$	1/2	4.328[1]	34	$[2s^2 2p_{1/2}^2 2p_{3/2}^3]_{3/2} 3d_{5/2}$	9/2	1.618[3]
3	$[2s^2 2p_{1/2}^2 2p_{3/2}^4]_{1/2}$	1/2	2.131[2]	35	$[2s^2 2p_{1/2}^2 2p_{3/2}^3]_{3/2} 3d_{3/2}$	7/2	1.619[3]
4	$[2s^2 2p_{1/2}^2 2p_{3/2}^3]_{3/2} 3s$	5/2	1.501[3]	36	$[2s^2 2p_{1/2}^2 2p_{3/2}^3]_{3/2} 3d_{5/2}$	1/2	1.623[3]
5	$[2s^2 2p_{1/2}^2 2p_{3/2}^3]_{3/2} 3s$	3/2	1.506[3]	37	$[2s^2 2p_{1/2}^2 2p_{3/2}^3]_{3/2} 3d_{5/2}$	3/2	1.627[3]
6	$[2s^2 2p_{1/2}^2 2p_{3/2}^3]_{3/2} 3s$	1/2	1.519[3]	38	$[2s^2 2p_{1/2}^2 2p_{3/2}^3]_{3/2} 3p_{3/2}$	1/2	1.628[3]
7	$[2s^2 2p_{1/2}^2 2p_{3/2}^3]_{3/2} 3s$	3/2	1.542[3]	39	$[2s^2 2p_{1/2}^2 2p_{3/2}^3]_{3/2} 3d_{5/2}$	5/2	1.630[3]
8	$[2s^2 2p_{1/2}^2 2p_{3/2}^3]_{3/2} 3s$	1/2	1.546[3]	40	$[2s^2 2p_{1/2}^2 2p_{3/2}^3]_{3/2} 3d_{3/2}$	3/2	1.635[3]
9	$[2s^2 2p_{1/2}^2 2p_{3/2}^3]_{3/2} 3p_{1/2}$	3/2	1.547[3]	41	$[2s^2 2p_{1/2}^2 2p_{3/2}^3]_{3/2} 3d_{5/2}$	5/2	1.638[3]
10	$[2s^2 2p_{1/2}^2 2p_{3/2}^3]_{3/2} 3p_{1/2}$	5/2	1.548[3]	42	$[2s^2 2p_{1/2}^2 2p_{3/2}^3]_{3/2} 3d_{3/2}$	1/2	1.653[3]
11	$[2s^2 2p_{1/2}^2 2p_{3/2}^3]_{3/2} 3s$	5/2	1.555[3]	43	$[2s^2 2p_{3/2}^4]_{3/2} 3p_{1/2}$	1/2	1.656[3]
12	$[2s^2 2p_{1/2}^2 2p_{3/2}^3]_{3/2} 3s$	3/2	1.556[3]	44	$[2s^2 2p_{1/2}^2 2p_{3/2}^3]_{3/2} 3d_{3/2}$	3/2	1.657[3]
13	$[2s^2 2p_{1/2}^2 2p_{3/2}^3]_{3/2} 3p_{3/2}$	1/2	1.557[3]	45	$[2s^2 2p_{1/2}^2 2p_{3/2}^3]_{3/2} 3d_{5/2}$	7/2	1.658[3]
14	$[2s^2 2p_{1/2}^2 2p_{3/2}^3]_{3/2} 3p_{3/2}$	5/2	1.558[3]	46	$[2s^2 2p_{3/2}^4]_{3/2} 3p_{3/2}$	3/2	1.659[3]
15	$[2s^2 2p_{1/2}^2 2p_{3/2}^3]_{3/2} 3p_{3/2}$	7/2	1.559[3]	47	$[2s^2 2p_{1/2}^2 2p_{3/2}^3]_{3/2} 3d_{5/2}$	5/2	1.661[3]
16	$[2s^2 2p_{1/2}^2 2p_{3/2}^3]_{3/2} 3p_{1/2}$	1/2	1.566[3]	48	$[2s^2 2p_{1/2}^2 2p_{3/2}^3]_{3/2} 3d_{3/2}$	5/2	1.662[3]
17	$[2s^2 2p_{1/2}^2 2p_{3/2}^3]_{3/2} 3p_{3/2}$	3/2	1.572[3]	49	$[2s^2 2p_{1/2}^2 2p_{3/2}^3]_{3/2} 3d_{5/2}$	3/2	1.663[3]
18	$[2s^2 2p_{1/2}^2 2p_{3/2}^3]_{3/2} 3p_{3/2}$	3/2	1.577[3]	50	$[2s^2 2p_{1/2}^2 2p_{3/2}^3]_{3/2} 3d_{3/2}$	7/2	1.668[3]
19	$[2s^2 2p_{1/2}^2 2p_{3/2}^3]_{3/2} 3p_{1/2}$	1/2	1.586[3]	51	$[2s^2 2p_{1/2}^2 2p_{3/2}^3]_{3/2} 3d_{5/2}$	9/2	1.670[3]
20	$[2s^2 2p_{1/2}^2 2p_{3/2}^3]_{3/2} 3p_{1/2}$	3/2	1.591[3]	52	$[2s^2 2p_{1/2}^2 2p_{3/2}^3]_{3/2} 3d_{5/2}$	5/2	1.672[3]
21	$[2s^2 2p_{1/2}^2 2p_{3/2}^3]_{3/2} 3p_{3/2}$	5/2	1.598[3]	53	$[2s^2 2p_{1/2}^2 2p_{3/2}^3]_{3/2} 3d_{3/2}$	1/2	1.672[3]
22	$[2s^2 2p_{1/2}^2 2p_{3/2}^3]_{3/2} 3p_{1/2}$	5/2	1.600[3]	54	$[2s^2 2p_{1/2}^2 2p_{3/2}^3]_{3/2} 3d_{5/2}$	7/2	1.675[3]
23	$[2s^2 2p_{1/2}^2 2p_{3/2}^3]_{3/2} 3p_{3/2}$	1/2	1.601[3]	55	$[2s^2 2p_{1/2}^2 2p_{3/2}^3]_{3/2} 3d_{3/2}$	3/2	1.675[3]
24	$[2s^2 2p_{1/2}^2 2p_{3/2}^3]_{3/2} 3p_{3/2}$	3/2	1.602[3]	56	$[2s^2 2p_{1/2}^2 2p_{3/2}^3]_{3/2} 3d_{3/2}$	5/2	1.677[3]
25	$[2s^2 2p_{3/2}^4]_{3/2} 3s$	1/2	1.603[3]	57	$[2s^2 2p_{1/2}^2 2p_{3/2}^3]_{3/2} 3d_{5/2}$	3/2	1.684[3]
26	$[2s^2 2p_{1/2}^2 2p_{3/2}^3]_{3/2} 3p_{3/2}$	7/2	1.611[3]	58	$[2s^2 2p_{1/2}^2 2p_{3/2}^3]_{3/2} 3d_{5/2}$	1/2	1.686[3]
27	$[2s^2 2p_{1/2}^2 2p_{3/2}^3]_{3/2} 3p_{3/2}$	3/2	1.611[3]	59	$[2s^2 2p_{3/2}^4]_{3/2} 3d_{5/2}$	5/2	1.719[3]
28	$[2s^2 2p_{1/2}^2 2p_{3/2}^3]_{3/2} 3d_{3/2}$	5/2	1.614[3]	60	$[2s^2 2p_{3/2}^4]_{3/2} 3d_{3/2}$	3/2	1.723[3]
29	$[2s^2 2p_{1/2}^2 2p_{3/2}^3]_{3/2} 3d_{3/2}$	3/2	1.614[3]	61	$2s^2 p^5 3s$		1.705[3]
30	$[2s^2 2p_{1/2}^2 2p_{3/2}^3]_{3/2} 3p_{3/2}$	5/2	1.615[3]	62	$2s^2 p^5 3p$		1.758[3]
31	$[2s^2 2p_{1/2}^2 2p_{3/2}^3]_{3/2} 3p_{1/2}$	3/2	1.615[3]	63	$2s^2 p^5 3d$		1.820[3]
32	$[2s^2 2p_{1/2}^2 2p_{3/2}^3]_{3/2} 3d_{5/2}$	7/2	1.615[3]	64	$2s^2 p^4 4l$		2.102[3]
				65	$2s^2 p^5 4l$		2.282[3]

Table II. Wavelengths and absorption oscillator strengths for strong 2p-3s and 2p-3d transitions in F-like Se.

Transitions	$J_i - J_f$	λ (Å) (this work)	λ (Å) (Ref. 3)	f (this work)	f (Ref. 3)
2-8	1/2-1/2	8.252	8.253	0.045	0.043
1-5	3/2-3/2	8.234	8.237	0.069	0.067
2-12	1/2-3/2	8.195	8.196	0.094	0.089
1-11	3/2-5/2	7.974	7.978	0.054	0.049
2-25	1/2-1/2	7.950	7.948	0.044	0.089
1-37	3/2-3/2	7.621	7.625	0.181	0.185
1-39	3/2-5/2	7.606	7.610	0.382	0.381
1-41	3/2-5/2	7.569	7.570	0.268	0.243
2-57	1/2-3/2	7.558	7.558	0.977	0.984
2-58	1/2-1/2	7.547	7.546	0.774	0.770
1-48	3/2-5/2	7.458	7.464	0.181	0.205
1-53	3/2-1/2	7.414	7.419	0.227	0.220
1-55	3/2-3/2	7.401	7.405	0.496	0.497
1-56	3/2-5/2	7.395	7.398	0.792	0.773
2-64	1/2-3/2	7.360	7.380	1.019	0.979
1-57	3/2-3/2	7.364	7.366	0.145	0.130

Table III. Collision strengths for excitation from some of the strong 2-3 transitions in F-like selenium. Notation a[b] means $a \times 10^b$.

Transition	Transition Energy(eV)	E/E _{th}	This Work	Ref. 7
1-17	1.572[3]	1.058	1.60[-2]	1.46[-2]
		1.260	1.63[-2]	1.50[-2]
		1.646	1.68[-2]	1.55[-2]
		2.360	1.75[-2]	1.62[-2]
		3.650	1.81[-2]	1.70[-2]
		5.849	1.87[-2]	1.78[-2]
1-31	1.615[3]	1.050	5.47[-2]	5.77[-2]
		1.250	5.62[-2]	5.95[-2]
		1.629	5.84[-2]	6.20[-2]
		2.320	6.06[-2]	6.48[-2]
		3.58	6.25[-2]	6.75[-2]
		5.722	6.37[-2]	6.98[-2]
2-38	1.585[3]	1.051	2.17[-2]	1.92[-2]
		1.260	2.23[-2]	1.97[-2]
		1.640	2.31[-2]	2.05[-2]
		2.350	2.39[-2]	2.14[-2]
		3.630	2.46[-2]	2.23[-2]
		5.802	2.50[-2]	2.30[-2]
2-43	1.613[3]	1.050	2.16[-2]	2.19[-2]
		1.250	2.20[-2]	2.25[-2]
		1.630	2.27[-2]	2.32[-2]
		2.320	2.34[-2]	2.41[-2]
		3.630	2.40[-2]	2.50[-2]
		5.726	2.43[-2]	2.58[-2]
1-56	1.677[3]	1.050	5.99[-2]	6.12[-2]
		1.240	6.81[-2]	6.97[-2]
		1.610	8.27[-2]	8.44[-2]
		2.270	1.05[-1]	1.07[-1]
		3.490	1.37[-1]	1.40[-1]
		5.550	1.74[-1]	1.80[-1]
2-57	1.640[3]	1.050	3.88[-2]	3.97[-2]
		1.250	4.34[-2]	4.54[-2]
		1.620	5.37[-2]	5.49[-2]
		2.300	6.81[-2]	6.98[-2]
		3.540	8.83[-2]	9.10[-2]
		5.650	1.12[-1]	1.17[-1]
2-64	1.680[3]	1.050	3.98[-2]	3.95[-2]
		1.240	4.17[-2]	4.46[-2]
		1.600	5.34[-2]	5.34[-2]
		2.270	6.78[-2]	6.74[-2]
		3.480	8.77[-2]	8.77[-2]
		5.540	1.11[-1]	1.13[-2]

Table IV. Collision excitation cross sections (cm^2) for excitation from some of the strong 2-3 transitions in F-like selenium. Notation a[b] means $a \times 10^b$

Transition	Transition Energy(eV)	E/E _{th}	This Work	Ref. 3
1-17	1.572[3]	1.13	2.711[-21]	1.519[-21]
		1.32	2.365[-21]	1.340[-21]
		1.64	1.950[-21]	1.125[-21]
		2.27	1.460[-21]	8.597[-22]
		3.54	9.730[-22]	5.917[-22]
1-31	1.615[3]	1.13	9.080[-21]	1.731[-20]
		1.31	8.020[-21]	1.523[-20]
		1.63	6.630[-21]	1.267[-20]
		2.32	4.840[-21]	9.480[-21]
		3.48	3.320[-21]	6.273[-21]
2-38	1.585[3]	1.13	7.320[-21]	1.904[-21]
		1.32	6.440[-21]	1.712[-21]
		1.64	5.320[-21]	1.466[-21]
		2.26	3.980[-21]	1.143[-21]
		3.52	2.640[-21]	7.966[-22]
2-43	1.613[3]	1.12	7.190[-21]	4.295[-21]
		1.31	6.290[-21]	3.803[-21]
		1.62	5.200[-21]	3.197[-21]
		2.24	3.860[-21]	2.426[-21]
		3.48	2.550[-21]	1.641[-21]
1-56	1.677[3]	1.12	1.000[-20]	1.040[-20]
		1.30	9.680[-21]	1.011[-20]
		1.61	9.160[-21]	9.628[-20]
		2.19	8.310[-21]	8.782[-21]
		3.38	7.080[-21]	7.538[-21]
2-57	1.640[3]	1.12	1.330[-20]	1.360[-20]
		1.30	1.280[-20]	1.317[-20]
		1.62	1.210[-20]	1.249[-20]
		2.22	1.090[-20]	1.129[-20]
		3.44	9.220[-21]	9.582[-21]
2-64	1.680[3]	1.12	1.330[-20]	1.302[-20]
		1.30	1.270[-20]	1.253[-20]
		1.60	1.190[-20]	1.183[-20]
		2.19	1.080[-20]	1.068[-20]
		3.38	9.108[-21]	9.090[-21]

F-LIKE SELENIUM MODEL

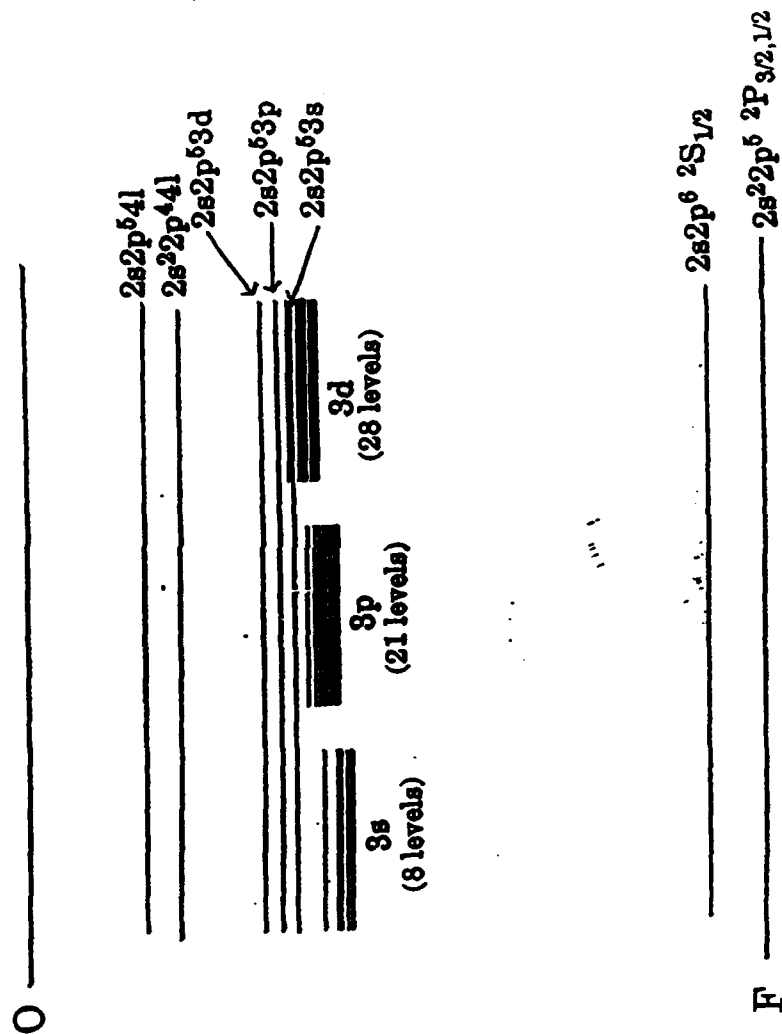


Fig. 1

DR RATE COEFFICIENTS

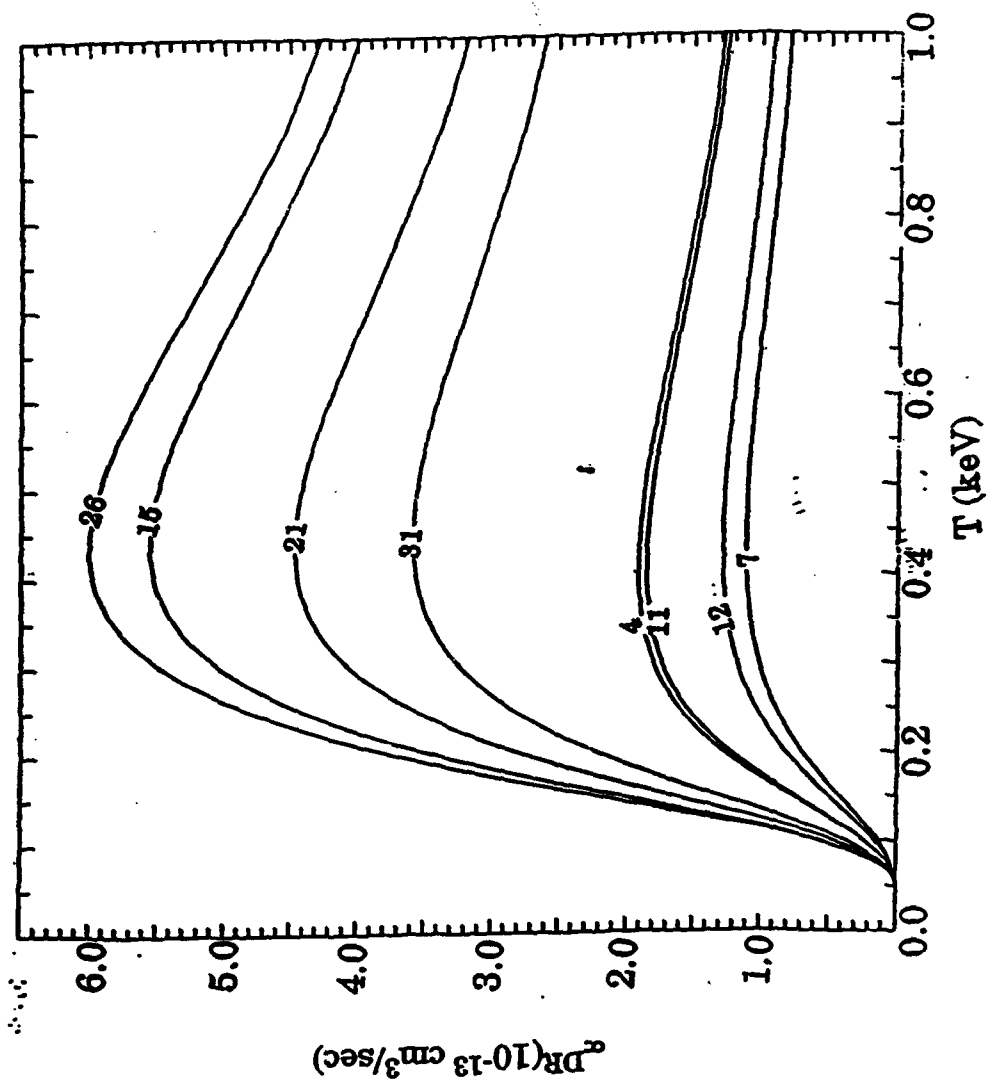


Fig. 2